The Effect Of Curing Types On Compressive Strength Of High Performance Concrete

Assist. Prof. Dr. Eng.
Nada Mahdi Fawzi
Civil Eng.Dept.

Eng (M.Sc.)
Ahmed Saher Tawfeeq Agha
Civil Eng.Dept.

Abstract

The present investigation considers the effect of curing temperatures (30, 40, and 50˚C) and curing compound method on compressive strength development of high performance concrete, and compares the results with concrete cured at standard conditions and curing temperature (21˚C). The experimental results showed that at early ages, the rate of strength development at high curing temperature is greater than at lower curing temperature, the maximum increasing percentage in compressive strength is 10.83% at 50C˚ compared with 21C˚ in 7days curing age. However, at later ages, the strength achieved at higher curing temperature has been less, and the maximum percentage of reduction has been 5.70% at curing temperature 50C˚ compared with 21C˚curing temperature in 91 days curing age. Also, the results showed that the specimens which are cured under field condition (using curing compound) have a various strength development rate, and the results indicate 92.11% as minimum field-standard curing strength ratio.

Key Words: High Performance Concrete, Compressive Strength, Standard Curing, Curing Temperature, Curing Compound, Field Conditions.

تأثير طرق الانضاج على مقاومة الانضغاط للخرسانة العالية الاداء

الاستاذ المساعد الدكتور
ندى مهدي فوزي
قسم الهندسة المدنية

المهندس (ماجستير)
أحمد ساهر توفيق آغا
قسم الهندسة المدنية

الخلاصة

هذا البحث اخذ بنظر الاعتبار تأثير درجات حرارة الانضاج (30، 40، 50 °م) وكذلك طريقة الانضاج الذاتي باستخدام المركبات الكيميائية على تطور مقاومة الانضغاط للخرسانة العالية الاداء، ومقارنة النتائج مع خرسانة منضجة تحت ظروف ودرجة حرارة قياسية (21°م). النتائج المختبرية اظهرت، في الاعمار المبكرة، بان معدل تطور مقاومة الانضغاط في درجات حرارة الانضاج العالية اعلى من درجات الانضاج الواطئة، حيث يصل نسبة الزيادة في مقاومة الانضغاط الى 10,83% عند درجة حرارة انضاج 50°م مقارنة بالدرجة القياسية (21°) بعمر 7 ايام. اما في الاعمار المتأخرة، فان مقاومة الانضغاط في درجات الحرارة العالية تكون اقل، حيث تصل نسبة النقصان الى 5,70% عند درجة حرارة 50°م مقارنة بالدرجة القياسية (21°م) بعمر 91 يوم. وكذلك النتائج اظهرت، بان النماذج المنضجة تحت الظروف الحقلية باستخدام المركبات الكيميائية، تمتلك معدلات متغيرة في تطور مقاومة الانضغاط وان اقل نسبة مقاومة حقلية الى قياسية كانت 92,11%.

Abbreviations

C°: Celsius Degree
C.A.: Coarse Aggregate
F.A.: Fine Aggregate
F: Field Curing
DRUW: Dry Rodded Unit Weight
F_{cu}: Cube Compressive Strength
HPC: High Performance Concrete
HRWRA: High Range Water Reducer Admixture
SF: Silica Fume
W/(C+P): Water to Cementitious Material Ratio

Introduction

Curing is the process of maintaining satisfactory moisture content and temperature in the concrete for a definite period of time. Hydration of cement is a long-term process and requires water and proper temperature. Therefore, curing allows continued hydration and consequently, continued gains in concrete strength (Mamlouk, 1999).

The curing period is defined as the time period beginning at placing, through consolidation and finishing, and extending until the desired concrete properties have developed (ACI308R-01).

Two types of curing are used throughout the experimental works to determine the effect of curing conditions on compressive strength HPC; the first type based on water curing under standard curing temperature 21C° and temperatures above standard (30, 40, and 50 C°) using special curing water tank for this purpose, to study the effect of high temperatures curing on compressive strength developments and comparing these with standard curing temperature. The second type of curing based on self curing, using curing compound materials, to investigate the efficiency of the curing compound type with low water cement ratio (0.28) and also to study the compressive strength development under field conditions in different weathers (cold and hot).

Curing temperature is the major factor that affects strength development rate. In general, increasing curing temperature has adverse effect on the concrete properties, especially on the compressive strength. When concrete cured at high temperature normally develops higher early strength than concrete produced and cured at lower temperature, but strengths are generally lower at 28 days and later ages (ACI305R-99). The explanation is that rapid initial hydration appears to form products of a poorer physical structure, probably more porous, so that a proportion of the pores will always remain unfilled, and on the other hand, rapid initial rate of hydration at higher temperatures retards the subsequent hydration and produces a non-uniform distribution of the products of hydration within the paste. The reason for this is that, at high initial rate of hydration, there is insufficient time available for the diffusion of the products of hydration away from the cement particle and for uniform precipitation in the interstitial space. As a result, a high concentration of the products of hydration is built up in the vicinity of the anhydrate particles, and this retards the subsequent hydration and adversely affects the long-term strength (Neville 1995).

The effect of high curing temperature on hardened concrete can be limited to (ACI305R-99):

a. Increased tendency for drying shrinkage and differential thermal cracking from either cooling of overall structure or from temperature differentials within the cross section of the member;
b. Decreased durability due to cracking.

c. Greater variability of surface appearance, such as cold joints or color differences, due to different rates of hydration.

1. Review Of Literature

1.1 Curing of Concrete

Curing can be defined as a procedure for insuring the hydration of the Portland cement in newly placed concrete. It generally implies control of moisture loss and sometimes of temperature. The hydration of Portland cement is the chemical reaction between grains of Portland cement and water to form the hydration product. Hydration can proceed until all the cement reaches its maximum degree of hydration or until all the space available for the hydrated product is filled by cement gel, whichever limit is reached first.

Concrete derives its strength by the hydration of cement particles. The hydration of cement is not a momentary action but a continuing process for a long time and requires water and proper temperature. The rate of hydration is fast to start with, but continues over a very long time at a decreasing rate. The quantity of the product of hydration and consequently the amount of gel formed depends upon the extent of hydration (Shetty, 1982).

The curing allows the hydration to be continued and consequently, continued gains in concrete strength. In fact once curing stops the concrete dries out and the strength gain stops (Mamlouk, 1999), as indicated in Figure (1).

1.2 Curing Types

Concrete can be kept moist (and in some cases at a favorable temperature) by three curing methods:

a. Methods that maintain the presence of mixing water in the concrete during the early hardening period. These include ponding or immersion, spraying or fogging, and saturated wet coverings. These methods afford some cooling through evaporation, which is beneficial in hot weather.

b. Methods that reduce the loss of mixing water from the surface of the concrete. This can be done by covering the concrete with impervious paper or plastic sheets, or by applying membrane-forming curing compounds.

c. Methods that accelerate strength gain by supplying heat and additional moisture to the concrete. This is usually accomplished with live steam, heating coils, or electrically heated forms or pads (Kosmatka, 2003).

The term "curing" of concrete is always governed by two variables, period and temperature (CIP, 2000):

1.2.1 Period: it should be noted that the time-strength relations in concrete technology generally assume moist-cured conditions and standard temperature. At given water/cement ratio, the longer the moist curing period the higher the strength assuming that the hydration of anhydrous cement particles will go on. In thin concrete elements, if water is lost by evaporation, air-curing conditions prevail, and strength gain will become very low and once the moisture is lost completely then will be stopped.

1.2.2 Temperature: is an important factor in proper curing, since the rate of hydration, and therefore, strength development, is faster at higher temperature. Generally, concrete temperature should be above 10C° for an adequate rate of strength development. Further, a uniform temperature should be maintained through the concrete section while it is gaining strength to avoid thermal cracking.

For moist-cured concrete, the influence of temperature on strength depends on the time-temperature history of

casting and curing. This can be illustrated with the help of three cases:

a) Concrete cast and cured at the same temperature;
b) Concrete cast at different temperature, but cured at standard temperature;
c) Concrete cast at standard temperature, but cured at different temperature.

In this experimental work all cubes prepared for compression test is cured as case three which casted at standard temperature (21±2C˚) and cured at temperatures 21, 30, 40, and 50 C˚.

The curing temperature is an important factor that affects directly the strength gain of concrete since its cement hydration rate.

It is interesting to note that concrete subjected to higher curing temperature at the early period of hydration is found to lose some of the strength gained at a later age. On the contrary, concrete cured at a comparatively lower temperature takes longer time to develop strength, but the strength attained will be higher than standard curing at later ages. The phenomenon of retrogression of strength explains that faster hydration will result in the formation of poor quality gels with porous open structure, whereas gel formed slowly but steadily compact and dense in nature (Shetty, 1982).

The effect of high curing temperature on hardened concrete can be limited to (ACI305R-99):

a. Increased tendency for drying shrinkage and differential thermal cracking from either cooling of overall structure or from temperature differentials within the cross section of the member;
b. Decreased durability due to cracking.
c. Greater variability of surface appearance, such as cold joints or color differences, due to different rates of hydration.

1.3 Curing Effect on Hardened Concrete

1.3.1 Strength Gain: laboratory tests show that concrete in dry environment can lose as much as 50 percent of its potential strength compared to similar concrete that is moist cured. Concrete placed under high temperature conditions will gain early strength quickly but later strength may be reduced. Concrete placed in cold weather will take longer to gain strength, delaying form removal and subsequent construction.

1.3.2 Durability: well-cured concrete has better surface hardness and will better withstand surface wear and abrasion. Curing also make concrete more water tight, which prevents moisture and water borne chemicals from entering into the concrete, thereby increasing durability and surface life.

1.3.3 Serviceability and Appearance: a concrete slab that has been allowed to dry out too early will have a soft surface with poor resistance to wear and abrasion (Shetty, 1982).

1.4 Previous Researches on Concrete Curing

Al-Foadi, has studied the effect of ambient temperature on properties of high performance concrete. Different curing temperatures are used for specimens curing (5, 23, 40, and 57C˚). He has reached the following conclusions:

1. The compressive strength for all mixes at early ages (7 and 28days), increases with the increase of the curing temperatures.

The range of increase at 7days is between 2% to 11.11%.

2. The compressive strength for all mixes at later ages (56 and 90 days) decreases with the increase of curing temperatures. The range of decreases at 90 days is between 3.41% to 13.63%.

Burg, has reported the influence of casting and curing temperature on concrete properties. He has cast concretes at temperatures (10, 23, and 32C˚) and these concretes have been cured at their casting temperature. He had observed that the effect of high temperatures on the early age strength are reversed after seven days when absolute strength of concrete cast and cured at 32C˚ is lower than concrete cast and cured at 23C˚.

Safiuddin, et al, have studied the effect of curing methods on the properties of silica fume concrete. They have used concrete with 10% silica fume cement replacement and three curing methods such as water curing, wrapped curing and dry air curing applied at 20±2C˚. They conclude that water curing is the most effective method; it produces the highest level of compressive strength.

Bushlaibi, has also showed the effect of curing methods on the compressive strength of silica fume high strength concrete. Five curing conditions are used, water curing (for 28 days), no curing, sprinkle curing (sprinkling two times in a day for seven days), plastic curing (sprinkling two times in a day with plastic cover sheet for seven days) and burlap curing (sprinkling two times in a day with burlap cover for seven days), and found that following conclusions:

1. The compressive strength of the silica fume high strength concrete, as is also true with normal strength concrete, is directly related to curing duration.
2. The adverse effect on the development of concrete compressive strength increases with increased temperature and test duration.
3. At curing ages of 28 days and beyond, the strength reduction reaches up to 12% of the control strength in some curing conditions.
4. Silica fume high strength concrete is adversely affected by hot dry environment in a manner similar to the way normal strength concrete is adversely affected by excessive moisture evaporation and badly dispersed hydration products resulting from high curing temperatures.

2. MATERIALS AND EXPERIMENTAL WORKS

2.1 Materials

2.1.1 Cement

Iraqi Ordinary Portland cement supplied from Taslooja Factory is used in casting all specimens throughout the experimental work. The required quantity of cement is delivered as one lot to avoid any difference in physical or chemical properties, and stored in sealed plastic container in the laboratory to prevent humidity effects until casting the specimen. Table (1) and (2) shows the physical properties and chemical analysis respectively, which confirm with the Iraqi Specifications I.Q.S. 5/1984.

2.1.2 Silica Fume

Silica fume of Turkish origin densified type is used throughout this work as a partial replacement of cement, which is supplied from “Dost Kimya Industrial Materials Co. Ltd”. It is stored in airtight plastic containers to avoid exposure to different atmospheric conditions.

Table (3) and (4) show the physical properties and chemical analysis of silica fume used respectively, results of tests show that the properties of silica fume used to comply with ASTM C1240-05 standard specification.

2.1.3 Super-Plasticizer

High-range water reducers admixture (HRWRA), according to ASTM C 494-05 Type G (water reducing and retarding), is used as super-plasticizer in preparing all the specimens in this study. It is commercially known Proplast PC260. Its produced by Ayla Company (from Jordon) and described as a high performance super-plasticizing admixture based on polycarboxylic with long chains specially designed to enable the water content of the concrete to perform more efficiency. Table (5) shows properties of the admixture according to manufacturer information.

2.1.4 Curing Compound

Liquid membrane-forming compounds consisting of waxes, resins, chlorinated rubber, and other materials can be used to retard or reduce evaporation of moisture from concrete. They are the most practical and most widely used method for curing not only freshly placed concrete but also for extending curing of concrete after removal of forms or after initial moist curing.

In this work, the field specimens are cured using curing compound, which is commercially known as Curecoat 220. It's produced by Ayla Company (from Jordon) and it complies with ASTM C309-07. Table (6) shows properties of the curing compound according to manufacturer information.

2.1.5 Coarse Aggregate

Crushed gravel supplied from Drbandikhan region (Sulaimaniah City) is used for preparing mixes with maximum aggregate size of 20mm. The sieve analysis of this aggregate is shown in Table (7). It conforms to the Iraqis specifications No. 45/1984. Table (8) shows the physical properties of the coarse aggregate.

2.1.6 Fine Aggregate

Natural sand supplied from Drbandikhan region (Sulaimaniah City) is used for preparing mixes with maximum aggregate size of 5mm. The sieve analysis of this aggregate is shown in Table (9). It conforms to the Iraqi Specifications No. 45/1984 zone 2. Table (10) shows the physical properties of the fine aggregate.

2.1.7 Mixing Water

Drinking tap water is used for mixing and curing the concrete.

2.2 EXPERIMENTAL PROGRAM

2.2.1 Mixture Proportioning Procedure

HSC (High Strength Concrete) is defined as concrete that has a specified cylinder compressive strength of 41MPa or greater. The ACI method (ACI 211.4) is used for calculation of the proportions of HSC, and silica fume was added to produce HPC. Table (11) shows mix proportions for HPC.

2.2.2 Preparation of Specimens

An electrical rotary mixer is used to batch all specimens with 0.05 m^3 capacities. The required quantities of material have been weighed and stored at the lab temperature for 24 hour before casting to control the moisture content and moisture meter is used before mixing to calculate the mixing water.

The ingredients have been initially mixed in dry condition (without silica fume),

and then water and HRWRA are added. The constituents are mixed for three minutes from the time of water adding. Finally silica fume is added and mixed until reaching a homogenous mix.

The moulds have been compacted, and filled in the required number of layer of approximately equal volume according to ASTM C192-07. After completing consolidation, the surfaces of the specimens have been leveled by hand trawling.

All the moulds are thoroughly cleaned and oiled before casting to obtain affair-face and to prevent specimens adhesive to the mould.

After completing the pouring, the specimens are covered with Nylon sheets to prevent evaporation of mixing water from concrete, and they have been left about 24hours in the laboratory. After that all the specimens have been de-moulded and cured in the desired method and period.

2.2.3 Curing

Drinking tab water was used for curing. Two methods of curing are used to cure the specimens:

2.2.3.1 Water Curing

Special tank has been manufactured and divided into four parts (21, 30, 40, and 50C˚) and used for water curing, the temperature is controlled by using a heater in each part (four heaters), and the curing tank is isolated by covering it with styrapor from each side to minimize temperature lost. Figure (2) shows water curing tank with various temperatures.

2.2.3.2 Self Curing

The field specimens have been coated with curing compound after sprinkled with water and left in site until testing day.

2.3 Compressive Strength Test

The test is conducted according to ASTM C39-05, using a digital compressive strength machine with 3000KN capacity.

This test method consists of applying a compressive axial load at a rate 0.25 ± 0.05MPa/s until failure occurs. The compressive strength of the specimen is calculated by dividing the maximum load attained during the test by cross sectional area of the specimen.

Cube of 150mm specimens are used, and taken out from the curing tank before 24 hours and tested in compressive machine on its perpendicular face to casting face at the age of 7, 28, 56, and 90 days, the average of three cubes has been recorded.

Compressive Strength, MPa, = P/A

Where:
P = axial load at failure, N;
A = cross sectional area, mm^2.

3. Results And Discussions

3.1 Curing Temperature Effect

The results reveal that specimens cured at 21C˚ (standard curing) show higher late age compressive strength compared with the same mix cured at temperature higher than 21C˚. These results are in complying with other researches (CIP, 2000 and Burg, 1996). Table (12) shows Compressive Strength of High performance Concrete.

At early ages, the rate of strength development at high curing temperature is greater than at lower curing temperature, the maximum increasing percentage is 10.83% at 50C˚ compared with 21C˚in 7days curing age. This is attributed to an increase in the hydration reaction rate. However at later ages, the strength achieved at higher curing temperature has been less. Table (13) shows the increasing and decreasing percentage due to curing temperature effect.

The reduction in concrete compressive strength due to high curing temperature at later ages is indicated in the Figure (3), and the maximum percentage of reduction has been 5.70% at curing temperature 50C° compared with 21C°curing temperature in 91 days curing age. This reduction can be explained to be due to the reaction products not having time to become uniformly distributed within the pores of the hardening paste at high temperature. In addition, shells made up of low permeability hydration products build up around the cement gains and these hindering further reactions (Neville, 1995 and Elsageer, 2009)

The non-uniform distribution of hydration products leads to larger pores that reduce compressive strength. This is in line with other research findings, which indicate that adverse effect on the development of compressive strength increases with the increased curing temperature and test duration (Burg, 1996).

3.2 Curing Compound Effect

The specimens are cured under field condition using curing compound they have a various strength development rate with curing age. This variation is attributed to the significant influence of ambient temperature on the specimens. The compressive strength ratio of field curing to standard curing reveals that, there is no ratio fall under 85% and this complies with ACI 318 requirement, the results indicate 92.11% as minimum field-standard curing ratio.

Figure (4) show the strength gain of field curing specimen compared to laboratory standard curing (21C°), and Table (14) shows compressive strength ratios of field curing to standard curing.

4. Conclusions

1. At early ages, the compressive strength increases with the increasing of curing temperatures and reveal an increasing up to 10.83% at 50C° compared to standard curing temperature (21C°).

2. At later ages, the high curing temperatures reveal a reduction in compressive strength up to 5.70% at 50C° compared to standard curing temperature (21C°).

3. The field compressive strength is typically lower than this measured on standard curing specimens prepared with the same mixes. On average, differences of 10% have been observed at 91days. Differences in curing conditions between the standard and field curing can explain these discrepancies.

References

1. ASTM: C 1240-05 "**Silica Fume Used in Cementitious Mixtures**", American Society for Testing and Material International, 2005.
2. ASTM: C 494-05 "**Chemical Admixtures for Concrete**", American Society for Testing and Material International, 2005.
3. ASTM: C309-07 "**Liquid Membrane-Forming Compounds for Curing Concrete**", American Society for Testing and Material International, 2007.
4. ASTM: C192-07 "**Making and Curing Concrete Test Specimens in the Laboratory**", American Society for Testing and Material International, 2007.
5. ASTM: C39-05 "**Compressive Strength of Cylindrical Concrete Specimens**", American Society for

Testing and Material International, 2005.

6. ACI Committee 211.4R-93 "Guide for Selecting Proportions for High-Strength Concrete with Portland Cement and Fly Ash", Reported by ACI Committee 211, Reapproved 1998, ACI Manual of Concrete Practice, 2009, pp2-9.
7. ACI Committee 308R-01 "**Guide to Curing Concrete**", Reported by ACI Committee 308, ACI Manual of Concrete Practice, 2009, pp2.
8. ACI Committee 305R-99 "Hot Weather Concreting", Reported by ACI Committee 305, ACI Manual of Concrete Practice, 2009, pp3.
9. Al-Foadi, W. K., "**Effect of Ambient Temperature During Mixing and Casting on Properties of Re-Tempered High Performance Self Compacting Concrete**", M.Sc. Thesis, College of Engineering, University of Technology, 2007.
10. Burg R. G., "**The Influence of Casting and Curing Temperature on the Properties of Fresh and Hardened Concrete**", Portland Cement Association, Research and Development Bulletin RD113T, 1996, pp1-13.
11. Bushlaibi A. H., "**Effects of Environment and Curing Methods on The Compressive Strength of Silica Fume High Strength Concrete**", United Arab Emirates University, Advances in Cement Research, No. 1, UAE, January 2004, pp17-22.
12. CIP, "**Concrete in Practice**", National Ready Mixed Concrete Association, 2000.
13. Elsageer, M, A., Millard, S. G. and Barnett, S. J., "**Strength Development of Concrete Containing Coal Fly Ash under Different Curing Temperature Conditions**", University of Liverpool, Department of Engineering, Brodie Tower, Brownlow Street, Liverpool, UK, L69 3GQ, 2009, pp1-11.
14. Kosmatka S. H., Kerkhoff B. and Panarese W. C., "**Design and Control of Concrete Mixtures**", Fourteenth Edition, Portland Cement Association, United States of America, 2003.
15. Mamlouk M. S. and Zaniewski J. P., "**Materials For Civil and Construction Engineers**", United States of America, 1999.
16. Neville A. M., "**Properties of Concrete**", Fourth and Final Edition, England, 1995, pp360, 559.

17.Shetty M. S., "**Concrete Technology**", India, 1982, pp277, 285, 526, 527.

18.Safiuddin M., Raman S. N. and Zain M.F., "**Effect of Different Curing Methods on the Properties of Micro Silica Concrete**", Australian Journal of Basic and Science, 2007, pp87-95.

19. 5القياسية رقم 19المواصفات العراقية ، المواصف "**السمنت البورتلاندي**"، الجهاز المركزي للتقييس والسيطرة النوعية، بغداد، 1984

20. **ركام المصادر الطبيعية المستعملة في الخرسانة والبناء**"، الجهاز المركزي للتقييس والسيطرة النوعية، بغداد، رقم 45 لسنة 1984

Table (1): Physical Prosperities of Portland Cement

Properties		Results	Iraqi Specification Limits (I.Q.S. 5/1984)
Fineness(m^2/kg)		300	Min, 230
Setting	**Initial setting**	135min.	Min, 45min.
	Final setting	4hrs.	Max, 10hrs.
Comp. St. (MPa)	**3 days**	25MPa	Not less than 15MPa
	7days	36MPa	Not less than 23MPa

Table (2): Chemical Analysis of Portland Cement

Oxides	Content, %	Iraqi Specification Limits(I.Q.S. 5/1984)
SiO_2	21.60	-
Fe_2O_3	3.28	-
AL_2O_3	4.52	-
CaO	62.07	-
MgO	1.93	Max, 5%
SO_3	2.19	Max, 2.8%
L.O.I	1.78	Max, 4%
L.S.F	0.89	0.66-1.02%
In. Residue	0.5	Max, 1.5%
Compound Composition (Bogues Equation)		
C_3S	47.16	-
C_2S	26.62	-
C_3A	6.43	-
C_4AF	9.97	-

Table (3): Chemical Analysis of Silica Fume

Oxides	Content, %	ASTMC1240 Specifications, %
SiO_2	87.66	Min. 85%
Fe_2O_3	1.75	-
AL_2O_3	1.5	-
CaO	1.55	-
MgO	1.33	-
SO_3	0.73	-
L.O.I	2.60	Max, 6%
Moisture Content	1.16	Max, 3%

Table (4): Physical Prosperities of Silica Fume

Properties	Result	ASTM C1240 Specifications
Specific Surface, m^2/gr.	23.36	Min,15
Retaining on Sieve 45 Micron,%	3.8%	Max,10
Strength Index ,@7day%	111%	Min, 75
Bulk Density, kg/m^3	550	-

Table (5): Properties of Super-Plasticizer (PC260)

Properties	Details
Colour	Light yellow liquid
Freezing Point	-1˚C approximately
Specific Gravity	1.1@25˚C
Air Entrainment	Typically less than 2%
Dosage	0.5-3.0 lit. per 100kg cement
Fire	Non-flammable

Table (6): Properties of Curing Compound (Curecoat 220)

Properties	Details
Colour	white Liquid
Minimum Application Temperature	5C°
Storage	5-35C°
Health and Safety	Not-hazardous
Fire	Non flammable

Table (7): Grading Analysis of Coarse Aggregate

Sieve (mm)	**Remaining** (gr.)	**Acc. Remaining** (gr.)	**Passing** %	**Iraqi Specification Limits (I.Q.S. 45/1984)** %
20	0	0	100	**95-100**
14	1455	1455	70.90	**-**
10	1149	2604	47.92	**30-60**
5	2297	4901	1.98	**0-10**
pan	87	**Dry Sample Weight**=5000gr.		

Table (8): Properties of Coarse Aggregate

Items	**Results**	**Iraqi Specification Limits (I.Q.S. 45/1984) ,%**
SO_3 Content	0.08%	Max, 0.1%
Passing on Sieve 75 micron	1.2%	Max, 3%
DRUW	1500kg/m^3	-
Specific Gravity	2.616	-
Absorption	1.05%	-

Table (9): Grading Analysis of Fine Aggregate

Sieve (mm)	Remaining (gr.)	Acc. remaining (gr.)	passing %	Iraqi Specification Limits (I.Q.S. 45/1984) Zone 2, %
10	0	0	100	**100**
4.75	315	315	91.00	**90-100**
2.36	178	493	85.91	**75-100**
1.18	1012	1505	57.00	**55-90**
0.60	387	1892	45.94	**35-59**
0.30	1191	3083	11.91	**8-30**
0.15	347	3430	2.00	**0-10**
pan	50	**F.M=** 3.06		**Dry Sample Weight**=3500gr.

Table (10): Properties of Fine Aggregate

Items	Results	Iraqi Specification Limits (I.Q.S. 45/1984)
SO_3 Content	0.15%	Max 0.5%
Passing on Sieve 75 micron	4.27%	Max 5%
DRUW	1848kg/m^3	-
Specific Gravity	2.59	-
Absorption	1.77%	-

Table (11): Mix Proportion for HPC

W/(C+P)	Silica Fume kg/m^3	Cement kg/m^3	C.A. kg/m^3	F.A. kg/m^3	Water L/m^3	HRWR L/m^3
0.28	15	478	1074	709.8	138	3

Table (12): Compressive Strength of High performance Concrete

HPC				
Temp.	**7 days**	**28 days**	**56 days**	**91 days**
21C°	55.76	60.98	67.90	68.25
30C°	59.08	61.12	67.23	67.20
40C°	60.22	61.98	65.63	66.31
50C°	61.80	62.33	64.03	65.00
Field (Ambient Temp.)	51.36	61.18	65.93	68.63

Table (13): Percentage of Increasing and Reduction in Compressive Strength due to Curing Temperature Effect

Mixes	**Temp.**	**Compressive Strength Ratio, %**			
		7 days	**28 days**	**56 days**	**91 days**
HPC	**30C°/ 21C°**	+5.95	+0.23	-0.99	-1.54
	40C°/ 21C°	+8.00	+1.64	-3.34	-2.84
	50C°/ 21C°	+10.83	+2.21	-5.70	-4.76

Table (14): Compressive Strength of Field curing Versus Standard Curing Strength

Mixes	**Compressive Strength Ratio, %**			
	7 days	**28 days**	**56 days**	**91 days**
HPC	92.11	100.33	97.10	97.63

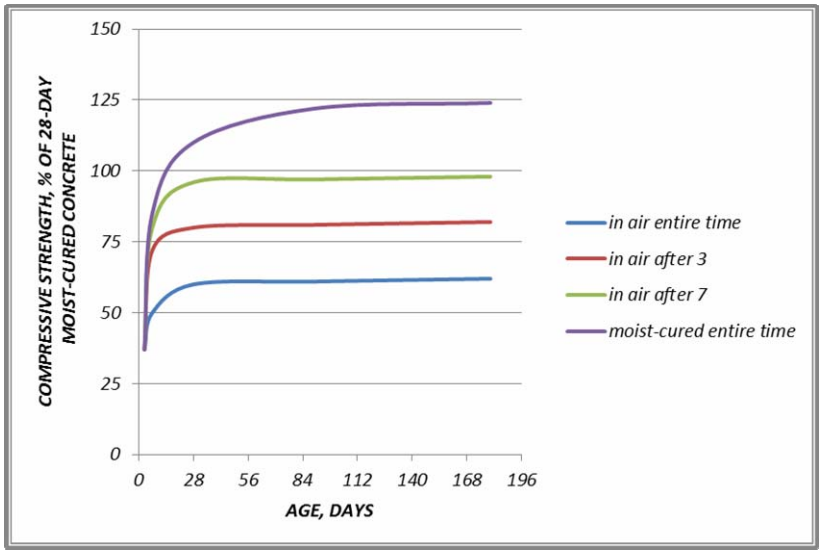

Figure (1): Compressive Strength of Concrete at Different Ages and Curing Levels (Mamlouk, 1999)

Figure (2): Water Curing Tank Divided to Various Temperatures

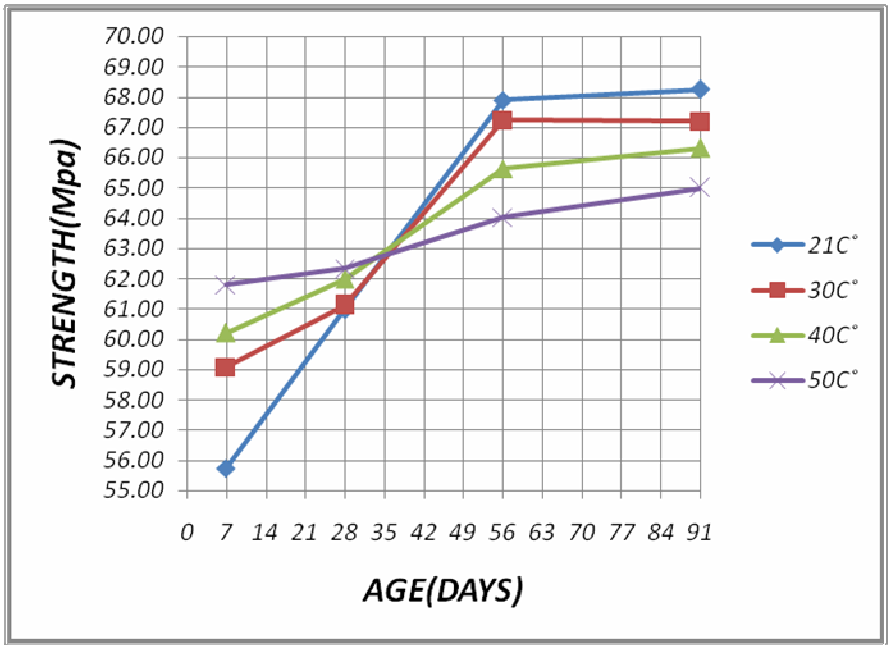

Figure (3): Curing Temperature Effect on Compressive Strength of High Performance Concrete

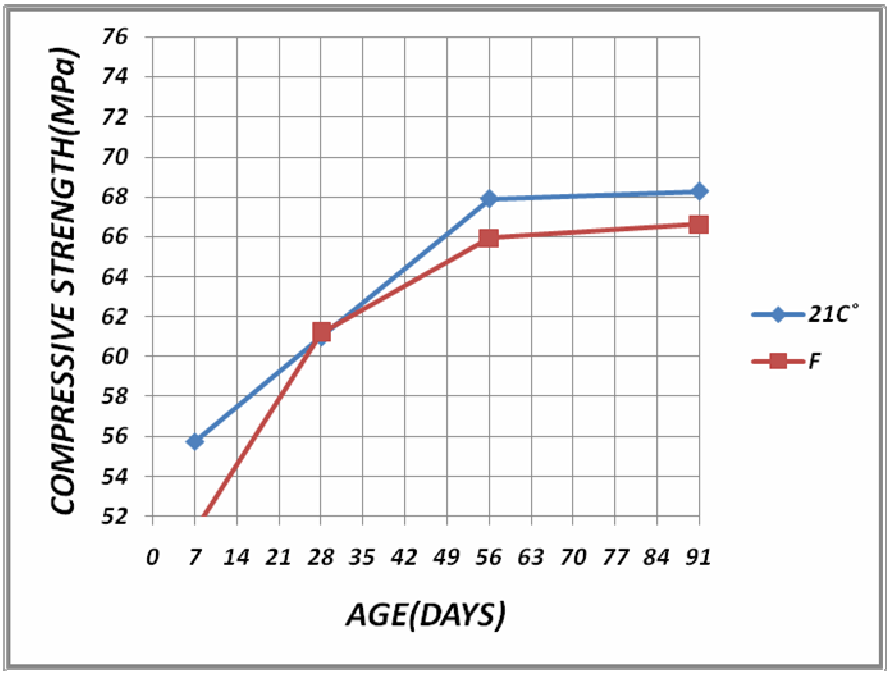

Figure (4): Compressive Strength Development of Standard Curing Compared with Field Curing HPC

Reduction of Concentrating Poisonous Metallic Radicals from Industrial Wastewater by Forward and Reverse Osmosis

Dr. G. A. R. Rassoul, Chemical Engineering Department
Dr. Ahmed Faiq Al – Alawy College of Engineering
Woodyian Nahedth Khudair University of Baghdad – Iraq.

Abstract

The research aims to use a new technology for industrial water concentrating that contains poisonous metals and recovery quantities from pure water. Therefore, the technology investigated is the forward osmosis process (FO). It is a new process that use membranes available commercial and this process distinguishes by its low cost compared to other process.

Sodium chloride (NaCl) was used as draw solution to extract water from poisonous metals solution. The driving force in the FO process is provided by a different in osmotic pressure (concentration) across the membrane between the draw and poisonous metals solution sides.

Experimental work was divided into three parts. The first part includes operating the forward osmosis process using TFC membrane as flat sheet for NaCl. The operating parameters studied were: draw solutions concentration (10 – 95 g/l), draw solution flow rate (12-36 I/h), temperature of draw solution (30 and 40°C), feed solution concentration (10 -210 mg/l), feed solution flow rate (10 -50 l/h), temperature of feed solution (30 and 40°C) and Pressure (0.4 bar).

The second part includes operating the forward osmosis process using CTA membrane as flat sheet for NaCl. The operating parameters studied were: draw solution concentration (15 – 95 g/l), feed solution concentration (10-210 mg/l). Constant temperature was maintained at 30°C.

The last part includes operating the reverse osmosis process using TFC membrane as spiral wound module in order to separate NaCl salt from draw solution and obtain on pure water so as to usefully in different uses and also obtain on solution of NaCl concentrate which was recirculated to forward osmosis process. It is then used as draw solution. The operating parameter studied was: feed solution flow rate (15-55 l/h).

The experimental results show that the water flux increases with increasing draw solution concentration, feed solution flow rate, temperature of draw solution and decreases with increasing feed solution concentration, draw solution flow rate and temperature of feed solution. The experiments also show that CTA membrane gives higher water flux than TFC membrane for forward osmosis operation.

Keyword : Forward osmosis; Reverse osmosis; wastewater; membrane; heavy metals; lead; cadmium; nickel.

اختزال تركيز جذور المعادن السامة من مخلفات المياه الصناعية بواسطة التنافذ الأمامي والتنافذ العكسي

د. غياث عبد الرضا رسول د. احمد فائق وديان ناهض خضير
قسم الهندسة الكيمياوية – كلية الهندسة - جامعة بغداد - العراق

الخلاصة

يهدف البحث لاستخدام تكنولوجيا جديدة لتركيز المياه الصناعية الحاوية على المعادن السامة واسترجاع كميات من المياه النقية . لذلك تمت دراسة عملية التنافذ الأمامي وهي طريقة جديدة تستخدم الأغشية المتوفرة تجارياً وتمتاز هذه العملية بكلفتها القليلة مقارنة بالطرق الأخرى .

تم استخدام كلوريد الصوديوم (NaCl) كمحلول سحب لنزع الماء النقي من محاليل المعادن السامة . القوة الدافعة في عملية التنافذ الأمامي ناتجة من فرق الضغط التنافذي (التركيز) على جانبي الغشاء بين محلول السحب ومحلول المعادن السامة .

تم تقسيم الجزء العملي إلى ثلاث أقسام : يضم القسم الأول تشغيل عملية التنافذ الأمامي باستخدام غشاء TFC على شكل صفيحة مستوية لمحلول سحب كلوريد الصوديوم.

الظروف التشغيلية التي تم دراستها : تركيز محلول السحب (15-95 g/l) ، معدل الجريان لمحلول السحب (12-36 l/h) ، درجـة حرارة محلـول السحب (30 , 40°C) ، تركيز محلول اللقيم (10-210 mg/l) ، معدل الجريان لمحلول اللقيم (10-50 l/h)، ودرجة حرارة محلول اللقيم (30 , 40 °C) . الضغط (0.4 bar).

القسم الثاني يضم تشغيل منظومة التنافذ الأمامي باستخدام غشاء نوع CTA على شكل صفيحة مستوية لمحلول السحب كلوريد الصوديوم . وكان تركيز محلول السحب (15-95 g/l) ، وتركيز محلول اللقيم (10-210 mg/ l) . درجة الحرارة ثابتة عند 30°C .

القسم الثالث تضمن تشغيل منظومة التنافذ العكسي باستخدام غشاء نوع TFC على شكل وحدة حلزونية لفصل ملح الـNaCl من محلول السحب والحصول على مياه نقية يمكن الاستفادة منه في العديد من الاستخدامات وكذلك الحصول على محلول NaCl مركز يتم استرجاعه إلى منظومة التنافذ الأمامي واستخدامه من جديد كمحلول سحب . وكان الظرف التشغيلي الذي تم دراسته : معدل الجريان لمحلول اللقيم (15-55l/h).

أظهرت نتائج البحث ان معدل تدفق الماء يزداد بزيادة تركيز محلول السحب ومعدل الجريان لمحلول اللقيم ودرجة حرارة محلول السحب والقوة الدافعة ويقل بزيادة تركيز محلول اللقيم ومعدل الجريان لمحلول السحب وزيادة درجة حرارة محلول اللقيم . وكذلك أظهرت النتائج ان أغشية CTA تعطي معدل تدفق ماء أعلى من أغشية TFC في عمليات التنافذ الأمامي .

Introduction

Industrial wastewater , which have heavy metals , are an important source of environmental pollution , Pb , Cd , Cu , Hg , Cr , Ni and Zn are the main trace elements that are the most harmful for public health . The optimization of wastewater purification process requires a development of new operation based on low cost raw materials with high pollutant removal efficiency. The complexity of effluents makes the process of heavy metals removal more difficult, as well as strict limitation that have been imposed to wastewater discharge everywhere in aquatic recipients (Achanai et al., 2008).

Several treatment technologies have been adopted to remove heavy metals. The major mode of removing heavy metals from water is by physical – chemical treatment.

Technologies for removing heavy metals include:

- Precipitations, including coagulation/ filtration, direct filtration and other methods.
- Adsorptive processes, including adsorption on to active alumina, activated carbon.
- Ion exchange processes, specifically anion exchange.
- Membrane filtration, including nanofiltration, reverses osmosis and other methods.

Some of these technologies are traditional treatment process (Coagulation / filtration and membrane filtration), which have been tailored to improve removal of heavy metals from water in water treatment plants (Jacks et al., 2001).

Fresh water scarcity is a growing problem in many regions in the world. Unchecked population growth and the impairment of existing freshwater sources cause many countries and communities in dry regions to turn to the ocean as a source of freshwaters (Mesa et al., 1997).

As a result of water scarcity and increasing demands for freshwater, water desalination is becoming an attractive method to produce water for both industrial and domestic usage. Currently, reverse osmosis (RO) is one of the most commonly used technologies due to the availability of stable and good performance membranes, and its relatively lower overall cost compared to thermal processes. Nevertheless, (RO) process generally requires high applied pressure, which leads to high energy requirement and thus, high operational cost. Recently forward osmosis (FO) process, which is a natural process, has been developed as a possible alternative technology for desalination due to its lower energy requirement.

The FO process utilizes an osmosis pressure gradient generated by a highly concentrated solution (known as "draw" solution) to allow water to diffuse through a semi permeable membrane from a saline feed water, which has a relatively lower concentration. Consequently, a less concentrated draw solution is being produced which may be further treated to extract for freshwater. FO bears some analogy to RO for that in both processes, water transports through a semi permeable membrane while salts are withheld by the membrane. However, the driving force in the FO process is created naturally by the concentration differences between the feed and draw solutions across the membrane, which substitutes the high pressure that is required in the (RO) process. Therefore, lesser energy is required for the (FO) process compared to the (RO) process (Howy et al., 2006). The main advantages of using FO are that operates at low or no hydraulic pressures, it has high rejection of a wide range of contaminates, and it may have a lower membrane fouling propensity than pressure-driven membrane process. Because the only pressure involved in the FO process is due to flow resistance in the membrane module (a few bars), the equipment used is very simple and membrane support is less of problem (Tzahi et al.,2006).The concentrated solution on the permeate side of the membrane is the source of the driving force in the FO process. When selecting a draw solution, the main criterion is that it has a higher osmotic pressure than the feed

solution. Also, osmotic agent solution solute must be non toxic and probably the solute is edible in some cases. Ideal draw solution does not interact with the membrane or degrade the membrane. It should be noted, the solute in a draw solution non-edible must be separated easily and economically to be used again (Mustafa, 2009). For these reasons forward osmosis process was used in this search.

The main purpose of this study is use forward osmosis process to reduce heavy metals in wastewater to level acceptable for water reuse or discharge. The first step is to study the effect of various operating condition for Feed (Lead nitrate $Pb(NO_3)_2$, Cadmium nitrate $Cd(NO_3)_2$ and Nickel chloride $NiCl_2$) and draw (NaCl) solution such as concentration, flow rate and temperature for the thin film composite (TFC) membrane which constructed as flat sheet module, and then study the effect of feed and draw solutions concentrations on water flux in the cellulose triacetate (CTA) membrane which is constructed as same module.

The second step is to use reverse osmosis (RO) process in order to separate draw solution (NaCl).

Concentration Polarization

The water flux in osmotic – driven membrane processes is described by equation

$$J_w = A\,(\sigma\,\Delta\pi - \Delta P) \quad (1)$$

Where J_w is the water Flux, A the water permeability constant of the membrane, σ the reflection coefficient, ΔP is the applied pressure, and Δπ represents the osmotic pressure difference across the active layer of the membrane. In such processes, the osmotic pressure difference across the active layer is much lower than the bulk osmotic pressure difference, which results in much lower water flux than expected (Mehta and Loeb, 1978; Lee et al., 1981; Leop et al., 1997.,Seppala and Lampinen, 2004 and Mccutcheon et al., 2006). The lower than expected water flux is often attributed to several membranes associated transport phenomena.

Specifically, two types of concentration polarization (CP) phenomena external CP and internal CP can take place in osmotic driven membrane processes as discussed below:

External Concentration Polarization

Concentration polarization on the feed side of a membrane is a significant problem in pressure driven membrane desalination processes. This phenomenon inhibits permeate flow due to an increased osmotic pressure at the membrane active layer interface on the feed side of the membrane. In an osmotic process, this phenomenon occurs on both sides of the membrane, with the effect being dilutive on the permeate side. These two phenomena collectively are referred as ECP. Specifically, this phenomenon on the feed and permeate side will be referred to as concentrative and dilutive ECP respectively.

To predict flux in the presence of ECP, the effective osmotic driving force at the membrane solution interface on both the feed and permeate sides of the membrane must be determined.

For a pressure driven membrane process, such as RO in the absence of ECP, the generalized flux equation is

$$J_w = A\,(\Delta P - \pi_{F,b}) \quad (2)$$

Where A is the pure water permeability coefficient, ΔP is the transmembrane pressure and $\pi_{F,b}$ is the osmotic pressure of the bulk feed solution. Complete rejection of the feed solute (i.e., the reflection coefficient $\sigma = 1$) is assumed. Equation 2 is valid only when the flux is low or the feed solution is very dilute. If flux becomes higher, the concentration polarization effect becomes significant. The membrane surface concentration on the feed side becomes larger than that of the bulk as solute is rejected, thus concentrating the feed solute. This phenomenon is referred as concentrative ECP. Equation 2 can be modified to account for concentrative ECP:

$$J_w = A\left(\Delta P - \pi_{F,b}\,\exp\left(\frac{J_w}{k_F}\right)\right) \quad (3)$$

Here, the exponential term is the concentrative ECP module (Mccutcneon and Elimelech, 2006) which is a function of water flux and mass transfer coefficient.

For osmotically driven membrane processes with a non dilute feed, a similar concentrative ECP will occur. In an osmotically driven membrane process, however, we must also consider the dilutive effect that occurs on the permeate side of the membrane. Dilutive ECP occurs as permeate water flow displaces draw solute at the membrane - draw solution interface, reducing the effective driving force of the draw solution. These two ECP phenomena are coupled for osmotic flow when solute is present on both sides of the membrane.

The standard flux equation for FO is gives as

$$J_w = A\,(\pi_{D,b} - \pi_{F,b}) \qquad (4)$$

Which predicts flux as a function of the difference in bulk osmotic pressure of the draw ($\pi_{D,b}$) and feed solutions ($\pi_{F,b}$). This equation does not account for ECP, which may be valid only if the permeate flux is very low. When flux rates are higher, though, the equation must be modified to include both concentrative and dilutive ECP moduli:

$$J_w = A\left[\pi_{D,b}\exp\left(-\frac{J_w}{k_D}\right) - \pi_{F,b}\exp\left(\frac{J_w}{k_F}\right)\right] \qquad (5)$$

Note that the dilutive effect is indicated by the negative exponential term modifying the draw solution osmotic pressure. Individual mass transfer coefficients on the feed, k_F, and permeate k_D, sides of the membrane must be considered. Equation 5 represents an implicit model for osmotic flux using a dense symmetric membrane. Therefore consider the case where the membrane is a symmetric, for which ICP effects are most significant (Jeffery et al., 2007).

$$k_F = 1.85\,\frac{D}{d_h^{0.67}L^{0.33}}\,(Re\ Sc)^{0.33} \qquad (6)$$

$$k_D = \frac{D\,\varepsilon}{\tau\, l} \qquad (7)$$

Where D is the diffusion coefficient, d_h is the hydraulic diameter, L is the channel length, Re is the Reynolds number, Sc is the Schmidt number, ε is the porosity of support layer, l is the thickness of support layer, and τ is the tortuosity of support layer (Young et al., 2009).

Finally, the flux of combined system using FO and RO is:

$$J_w = A\left[\Delta P + \pi_{D,b}\exp\left(-\frac{J_w}{k_D}\right) - \pi_{F,b}\exp\left(\frac{J_w}{k_F}\right)\right] \qquad (8)$$

Figure 1 (a) shows this phenomenon with a dense symmetric membrane.

Internal Concentration Polarization

Asymmetric membrane, commonly used in pressure driven membrane processes, use porous layer to mechanically support a thin salt rejecting active layer. In osmotic processes, salt must pervade this porous layer, which do not reject the salt to any appreciable degree, yet still hinder its diffusion, to establish the osmotic driving force across this active layer. When water permeates the membrane, concentration polarization occurs on both sides of this active layer. However, the porous layer provides a protected environment on one side of the active layer where the polarized layer can form without the mitigating effects of cross flow (Mccutcheon and Elimelech, 2006 and Gray et al., 2006). There are two types of ICP depending on the orientation of the membrane. In the PRO mode, the porous layer is against the feed solution and the feed solute will be concentrated within the membrane, Figure (b). In the FO mode, the porous layer is against the permeate side. The draw solute diffuses into this porous layer but becomes diluted as water permeates the membrane, Figure 1(C). These are referred phenomena as concentrative and dilutive ICP, respectively (Gray et al., 2006 and Mccutcheon and Elimelech, 2006).

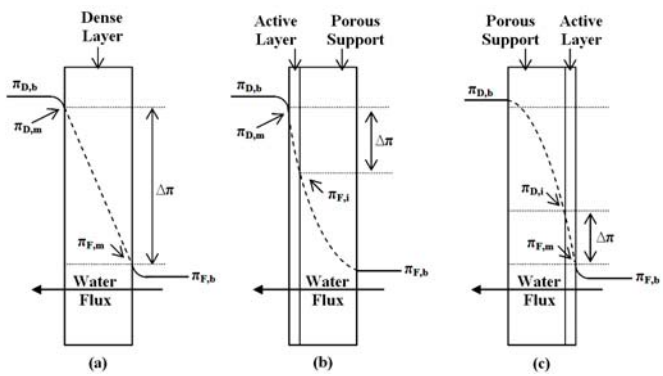

Fig. 1 Illustration of osmotic driving force profiles for osmosis through several membrane types and orientations, incorporating both internal and external concentration polarization. (a) The profile illustrates concentrative and dilutive external CP.

(b) PRO mode; the profile illustrates concentrative internal CP and dilutive external CP.

(c) FO mode; the profile illustrates dilutive internal CP and concentrative external CP.

EXPERIMENTAL

Feed Solution

Three types of feed solution were used for the forward osmosis process. Lead nitrate ($Pb(NO_3)_2$), Cadmium Nitrate ($Cd(NO_3)_2$) and Nickel Chloride ($NiCl_2$). Deionized water, of (3-8) µs/cm conductivity, was used for preparing feed solution with concentration of (10 to 210) mg/l. The chemical analysis of the feeds is given in Table 1.

Table 1 Chemical Specification of Feed Solutions

Lead Nitrate $Pb(NO_3)_2$ = 331.23	Assay > 98.0% Chloride (Cl) < 0.005% Copper(Cu) < 0.005% Iron (Fe) < 0.005% Zinc (Zn) < 0.005% Calcium (Ca) < 0.005%
Cadmium nitrate $Cd(NO_3)_2$ = 236.43	Assay > 98.0% Chloride (Cl) < 0.005% Sulfate (So_4) < 0.005% Copper(Cu) < 0.005% Lead (Pb) < 0.005% Iron (Fe) < 0.005% Zinc (Zn) < 0.005% Calcium (Ca) < 0.005%
Nickel chloride $NiCl_2$ = 129.6	Assay > 98.0% Copper(Cu) < 0.005% Lead (Pb) < 0.005% Iron (Fe) < 0.005% Zinc (Zn) < 0.005% Calcium (Ca) < 0.005%

Draw Solution

Deionized water of (3-8) µs/cm conductivity, was used for preparing sodium chloride with concentration of (15 to 95) g/l. NaCl was selected as osmotic agent because it has high osmotic pressure, high solubility, easily and economically be separated and recycled to high concentration using reverse osmosis process. Table 2 shows (NaCl – H_2O) draw solution concentration and their corresponding conductivities at 30°C temperature. The chemical analysis of the NaCl is given in Table 3.

Table 2 Sodium Chloride Conductivity, at 30 °C

Concentration (g/l)	Conductivity (ms/cm)
5	9.95
15	27.7
25	44.2
35	59.4
45	73.8
55	87.6
65	100.6
75	112.8
85	124.6
95	135.6

Table 3 Chemical Specification of Sodium Chloride Solutions

Sodium chloride (Assay 99.5% min)	
Maximum limits of Impurities	%
Ammonia	0.002
Iron	0.002
Lead	0.0005
Potassium	0.02
Sulphate	0.02
Molecular weight of Nacl	= 58.44

The Forward Osmosis Process

Figure 2 describes the forward osmosis apparatus used in laboratory of chemical engineering department. The feed and draw solutions were pumped by means of a centrifugal pump (11.4 – 54.6 l/min, 3 – 13.7 m. H, 210 Watt, STUART TURNER LTD. HENLEY ON THAMES ENG, England) to

pass through channels of osmosis cell. The flow rate of draw and feed solutions was regulated by means of globe valve connected at the discharge of the pumps, and measure with a calibrated rotameters with range flow (12– 120 l/hr) and (6-60 l/h). Both the draw and feed solutions were held at the same temperature and flow rate during the FO tests. Concentration of heavy metals was measured by digital total dissolved solid (TDS) meter(waterproof TDSTestr High+, range(0-1 * 10^4 mg/l), operating temperature (0-50 °C), accuracy is ±1 % , and Oakton instruments), While, the concentration of draw solution was measured by digital laboratory conductivity meter (inoLab Cond 720, range (0 – 2 * 10^6 µS/cm), operating temperature (0 – 55 ^oC), accuracy is ± 0.5% full scale, the electrode material is graphite, and made in Germany (WTW)) and a digital balance was used to measure the samples weight in experiments(Sartorius BP 3015 max. 303 g, d= 0-1 mg). The flat sheet module was designed to serve forward osmosis operation it has two symmetric flow channels on both side of the applied membrane. The dimensions of the cross section: width W = 6 Cm, length L = 19.7 Cm and hight H = 10 Cm. The feed solution and the draw solution flow on same side of a flat sheet membrane. In this study used two types of (TFC) and (CTA). Thin film composite membrane is an aromatic polyamide consisting of three layers: polyester support web, microporous polysulphone interlayer, and ultra thin polyamide barrier layer on the top surface. The specifications of the module are: membrane active area (197 cm^2), salt rejection (96-99%), maximum operating pressure (6.9 Mpa), and maximum operating temperature (113 F). The CTA was specifically developed for FO applications and was a required from Hydration Technologies In. (Albany , OR).The thickness of the membrane is less than 50 μm and the structure of cellulose triacetate (CTA) forward osmosis membrane is quite different from standard reverse osmosis membranes. Reverse osmosis membrane typically consist of a very thin active layer (less than 1 µm) and a thick porous support layer. The specification of the module is: membrane active area (197 cm^2), salt rejection (greater than 95%).

The Reverse Osmosis (RO) process

The draw solution from the forward osmosis process is fed into the reverse osmosis process and the product of the reverse osmosis is two streams, the one stream contains pure water and the other stream contains solution of NaCl concentrate that recirculated to the forward osmosis. The devices used in forward osmosis unit itself was used in reverse osmosis unit, except the selected membrane used a TFC membrane constructed as spiral – wound module instead of plate and frame module. An experimental rig of reverse osmosis unit was constructed in the laboratory as shown schematically in figure 3. Also, in RO we need to high pressure pump (Santoprene and Polyproplene materials, maximum pressure = 120 psi, power = 220 – 240 V, and Current = 1.2 A). To overcome on osmotic pressure for salt NaCl in water.

Experimental Procedure

Forward Osmosis Process

Two types of solution were prepared to run the experiments in the present work. The first is the draw solution which is the solution containing NaCl which was prepared in the QVF glass vessels by dissolving the NaCl salt in 20 liter of deionized water . The second solution is the feed solution which is prepared in the QVF glass by dissolving different amounts of either Lead nitrate or Cadmium nitrate or Nickel chloride to obtain different concentration of heavy metals in 20liter of deionized water. NaCl solution was pumped to one side of the membrane and heavy metals solution was pumped to the other side of the membrane by different pump. The apparatus was designed so that both the draw solution flow and feed solution flow tangent to the membrane in the same direction (Co-current flow).

The steady – state took between 0.5 to 1 hr. In this time the conductivities and

concentrations of the feed solution, draw solution, feed solution outlet concentration and draw solution outlet concentration were measured by the conductivity and TDS meters, and the water flux through membrane. The water flux was calculated by dividing the permeate volume by the product of effective membrane area and time.

Reverse Osmosis Process

The diluted draw solution (NaCl-H_2O) exterior from forward osmosis process is sent to a reverse osmosis process in order to separate draw solution into two streams; that is one contains pure water and the other contains solution of NaCl concentrate

After recording the conductivity and concentrations, calculations of required mentioned parameters were reported. The solution was drained through a drain valve. The whole system washed by deionized water, so that it can be ready for next run.

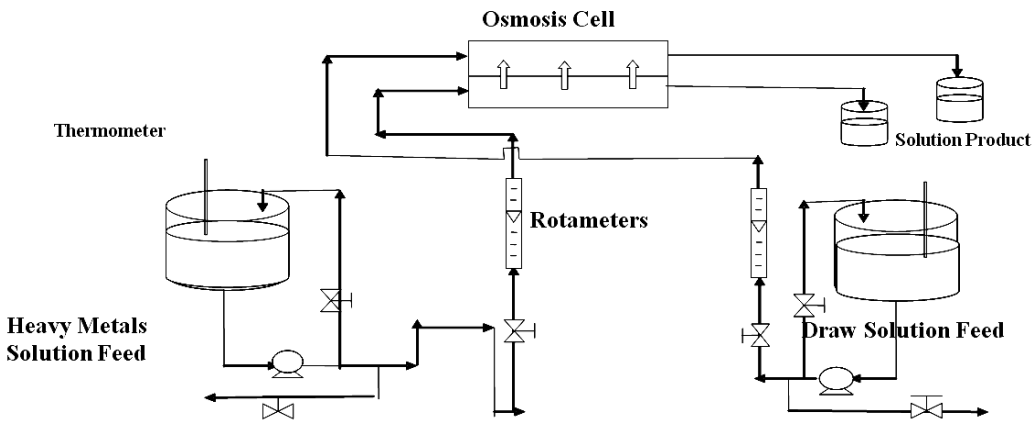

Fig. 2 Schematic Diagram of Forward Osmosis Process

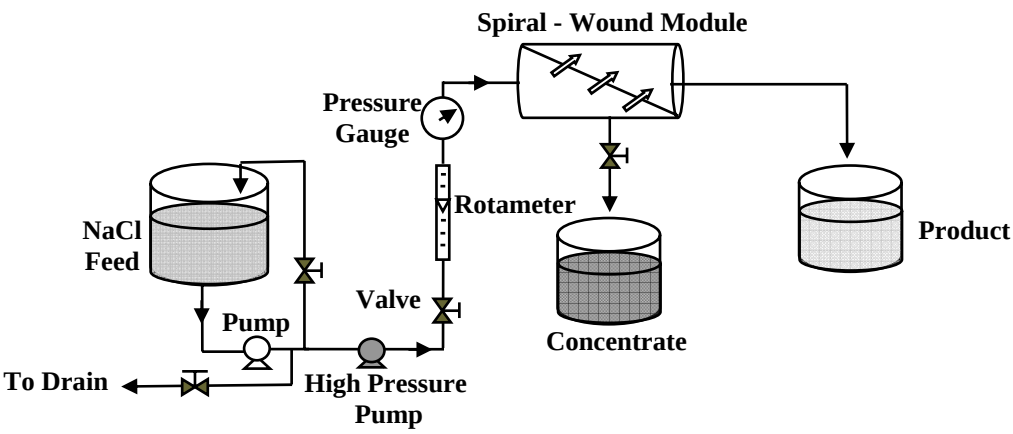

Fig. 3 Schematic Diagram of Reverse Osmosis Process

Results And Discussion

Forward Osmosis Process

Thin Film Composite Membrane

The water flux calculated by dividing the volume of pure water which transfers from feed to draw solution on time and active area of membrane. The water flux increasing with increasing draw solution concentration because the driving force (osmotic pressure of draw solution – osmotic pressure of heavy metals) increased. An increase as demonstrated in Figure 4 for Sodium chloride (NaCl) as draw solution at three types of feed solution. The solution of heavy metals loses quantities of pure water and this leads to increased concentration of heavy metals. The same quantities of pure water transferred across the membrane to the draw solution, as a result, decrease the concentration of draw solution. The effect of draw solution concentration (C_{NaCl} inlet) on draw solution outlet concentration (C_{NaCl} outlet) is shown in Figure 5. Figure 6 show the effect of draw solution concentration (C_{NaCl} inlet) on feed solution outlet concentration (C_{metals} outlet) at three types of feed solution.

By increasing feed solution concentration (C_{metals} inlet), driving force decreases, see figure 7. This appears as a decrease of water flux through the membrane. The water flux decreasing with increasing feed solution concentration because the driving force (osmotic pressure of draw solution – osmotic pressure of heavy metals) decreases for Lead Nitrate ($Pb(NO3)_2$, Cadmium Nitrate ($Cd(NO3)_2$ as feed solution at NaCl draw solution. Osmotic pressure depends on the molecular weight of solute and number of dissociation. The dcrease in water flux resulted from Lead Nitrate ($Pb(NO3)_2$) is larger than Cadmium Nitrate ($Cd(NO3)_2$ and Nickel Chloride ($NiCl_2$) because it has large osmotic pressure (driving force) than (Cd(NO3)2) and ($NiCl_2$). The effect of feed solution concentration on draw solution outlet concentration (C_{NaCl} outlet) is show in figure 8. Figure 9 show the effect of feed solution concentration on feed solution outlet concentration. Increasing the draw solution flow rate (Q_{NaCl}) prevents the concentration buildup in the solution at the vicinity of the membrane surface (support layer), and resulting in decreasing the driving force. Thus, water flux decreased with increasing the flow rate .This is shown in Figures 10.The effect of draw solution flow rate on draw solution outlet concentration (C_{NaCl} outlet) is shown in figure 11. Figure 12 show the effect of draw solution flow rate on feed solution outlet concentration. Increasing the feed solution flow rate prevents the concentration buildup in the solution at the vicinity of the membrane surface (Active layer), leading to increase a driving force($\Delta\pi$).This behavior contradicts the case of increasing the draw solution flow rate. Figures 13 show the effect of feed solution flow rate on water flux for three types of feed solution at NaCl solution. The effect of feed solution flow rate (Qmetals) on draw solution outlet concentration (C_{NaC}l outlet) is shown in figure 14. Figure 15 show the effect of feed solution flow rate on feed solution outlet concentration (C_{metals} outlet).

Cellulose Triacetate Membrane

By increasing the concentration of draw solution, osmotic pressure difference increases and then the driving force increases, this leads to an increase in water flux, inversely when increasing the feed solution concentration osmotic pressure difference ($\Delta\pi$) decreases. This appears as a decreasing in water flow through the membrane. This shown in Figures 16and 17.

The effect of feed and draw solution concentrations on the draw solution outlet concentration and feed solution outlet concentration are shown in Figures 18, 19, 20, and 21. Generally, any membrane consists of two layers: active layer and support layer. In RO which operates at high pressure it needs membrane with very thick support layer to withstand this pressure but FO which operates at low or no hydraulic pressure it needs membrane with very thin support layer. Because CTA membrane has thickness less than that of TFC membrane, it is found that for forward osmosis operation CTA membrane is more suitable than TFC membrane. CTA membrane was designed to operate for forward osmosis operation. This can be shown in Figure 22 where the water flux with CTA without using pressure is higher than TFC with using pressure.

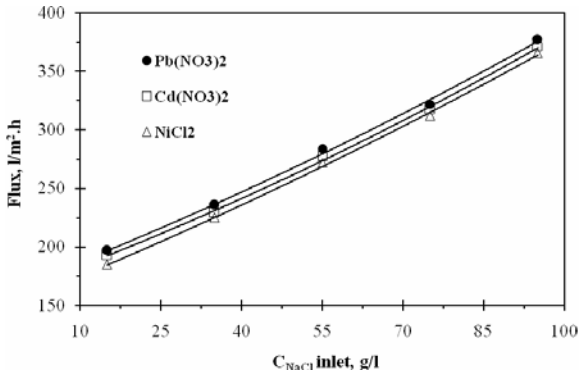

Figure 4 Water flux with draw solution inlet concentration (C_{NaCl} inlet) for different feed solutions (Q_{metals} = 60 l/hr, Q_{NaCl} = 12 l/h, C_{metals} inlet = 150 mg/l, T (feed & draw) = 30 ± 1 °C, P = 0.4 bar).

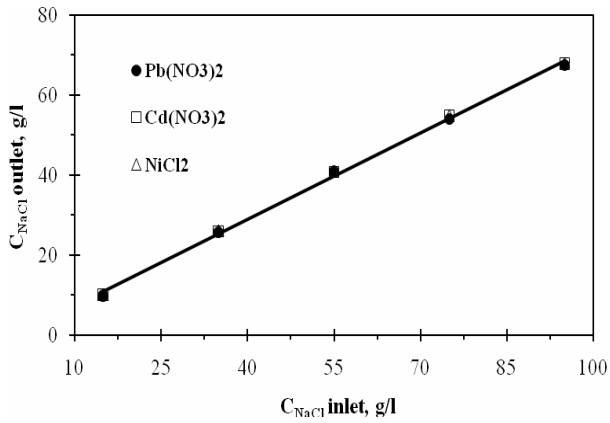

Figure 5 Draw solution outlet concentration (C_{NaCl} outlet) with draw solution inlet concentration (C_{NaCl} inlet) for different feed solutions (Q_{metals} = 60 l/h, Q_{NaCl} = 12 l/h, C_{metals} inlet = 150 mg/l, T (feed & draw) = 30 ± 1 °C, P = 0.4 bar).

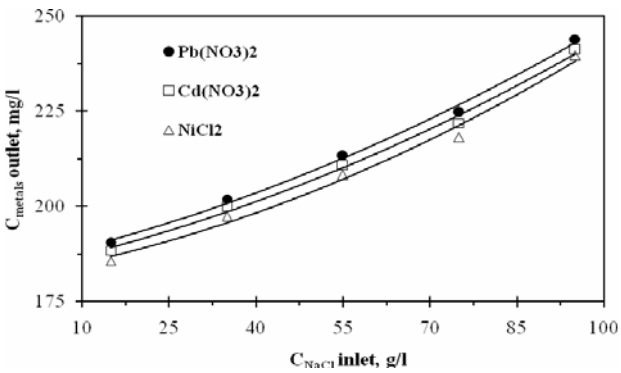

Figure 6 Feed solution outlet concentration (C_{metals} outlet) with draw solution inlet concentration (C_{NaCl} inlet) for different feed solutions (Q_{metals} = 60 l/h, Q_{NaCl} = 12 l/h, C_{metals} inlet = 150 mg/l, T (feed & draw) = 30 ± 1 °C, P = 0.4 bar).

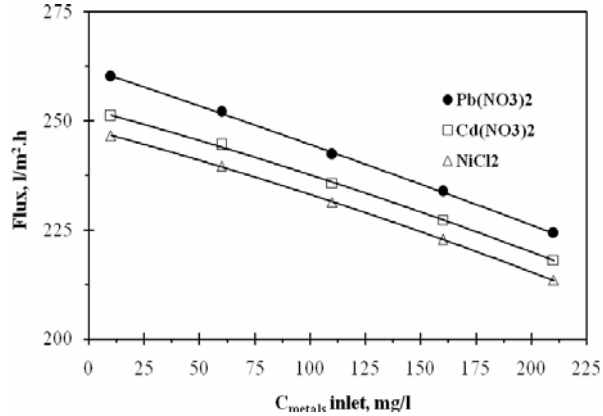

Figure 7 Water flux with feed solution inlet concentration (C_{metals} inlet) for different feed solutions (Q_{metals} = 60 l/h, Q_{NaCl} = 12 l/h, C_{NaCl} inlet = 35 g/l, T (feed & draw) = 30 ± 1 °C, P = 0.4 bar).

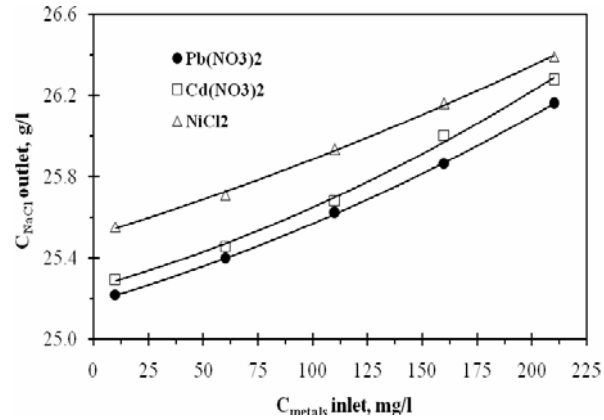

Figure 8 Draw solution outlet concentration (C_{NaCl} outlet) with feed solutions inlet concentration (C_{metals} inlet) for different feed solutions (Q_{metals} = 60 l/h, Q_{NaCl} = 12 l/h, C_{NaCl} inlet = 35 g/l, T (feed & draw) = 30 ± 1 °C, P = 0.4 bar).

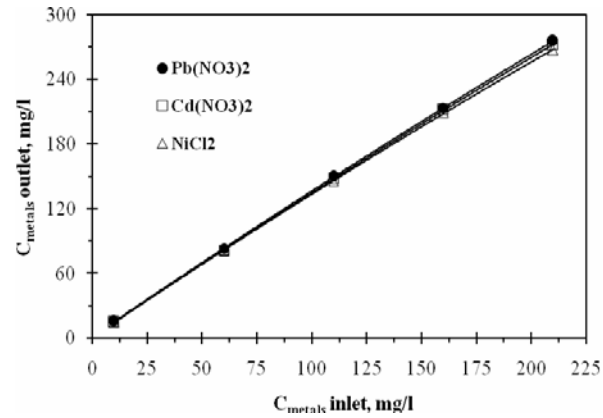

Figure 9 Feed solution outlet concentration (C_{metal} outlet) with feed solution inlet concentration (C_{metals} inlet) for different feed solutions (Q_{metals} = 60 l/h, Q_{NaCl} = 12 l/h, C_{NaCl} inlet = 35 g/l, T (feed & draw) = 30±1 °C, P = 0.4 bar).

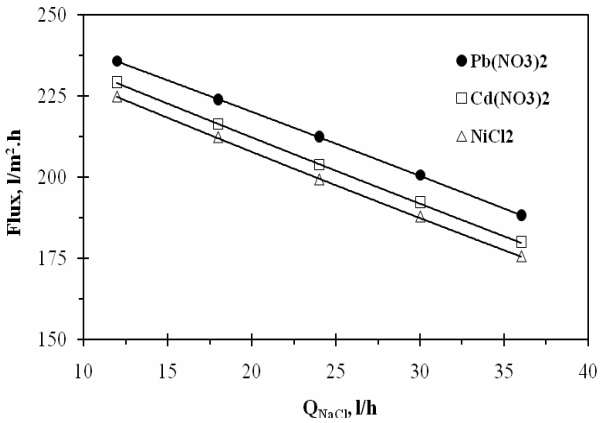

Figure 10 Water flux with draw solution flow rate (Q_{NaCl}) for different feed solution (Q_{metals} = 60 l/hr, C_{metals} inlet = 150 mg/l, C_{NaCl} inlet = 35 g/l, T (feed & draw) = 30 ± 1 °C, P = 0.4 bar).

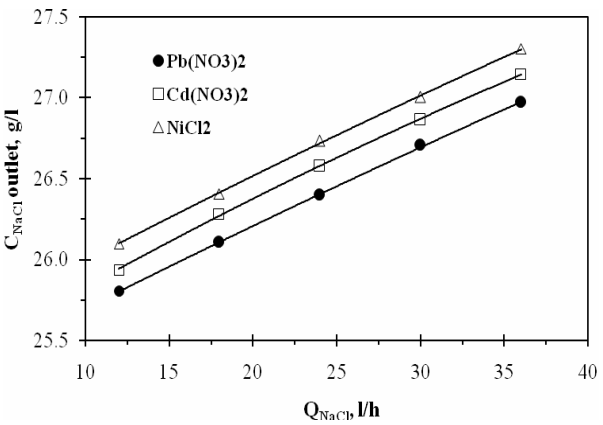

Figure 11 Draw solution outlet concentration (C_{NaCl} outlet) with draw solution flow rate (Q_{NaCl}) for different feed solutions (Q_{metals} = 60 l/h, C_{metals} inlet = 150 mg/l, C_{NaCl} inlet = 35 g/l, T (feed & draw) = 30 ± 1 °C, P = 0.4 bar).

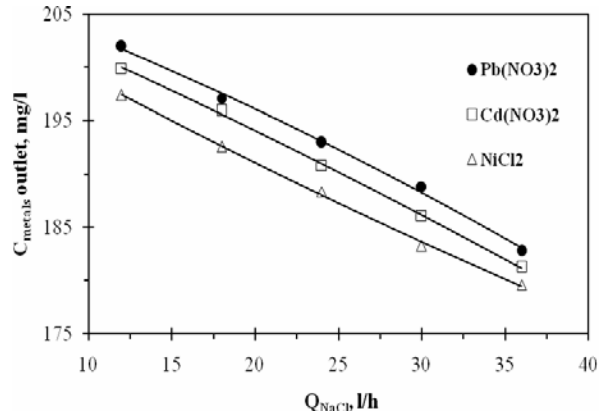

Figure 12 Feed solution outlet concentration (C_{metals} outlet) with draw solution flow rate (Q_{NaCl}) for different feed solutions (Q_{metals} = 60 l/h, C_{metals} inlet = 150 mg/l, C_{NaCl} inlet = 35 g/l, T (feed & draw) = 30 ± 1 °C, P = 0.4 bar).

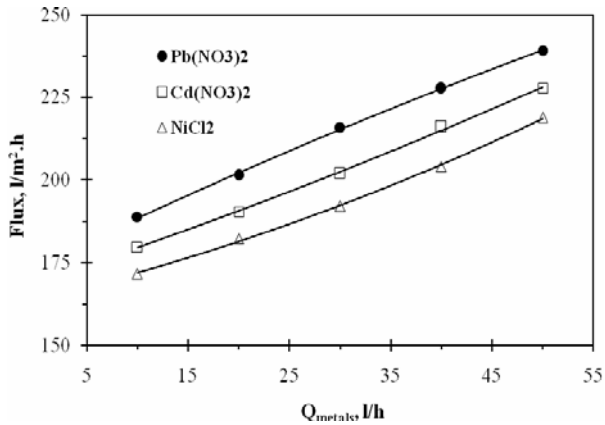

Figure 13 Water flux with feed solution flow rate (Q_{metals}) for different feed solutions (Q_{NaCl} = 12 l/h, C_{metals} inlet = 150 mg/l, C_{NaCl} inlet = 35 g/l, T (feed & draw) = 30 ± 1 °C, P = 0.4 bar)

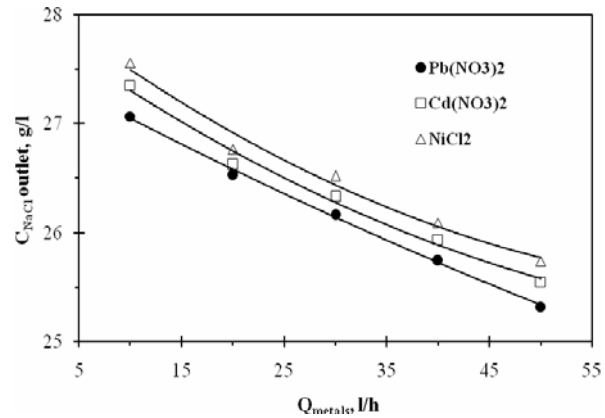

Figure 14 Draw solution outlet concentration (C_{NaCl} outlet) with feed solution flow rate (Q_{metals}) for different feed solutions (Q_{NaCl} = 12 l/h, C_{metals} inlet = 150 mg/l, C_{NaCl} inlet = 35 g/l, T (feed & draw) = 30 ± 1 °C, P = 0.4 bar).

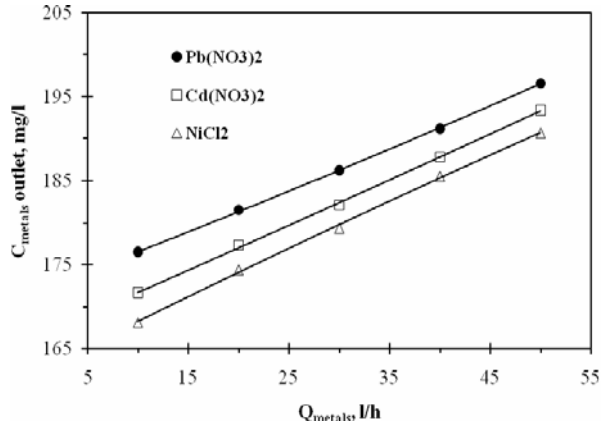

Figure 15 Feed solution outlet concentration (C_{metal} outlet) with feed solution flow rate (Q_{metals}) for different feed solutions (Q_{NaCl} = 12 l/h, C_{metals} inlet = 150 mg/l, C_{NaCl} inlet = 35 g/l, T (feed & draw) = 30 ± 1 °C, P = 0.4 bar).

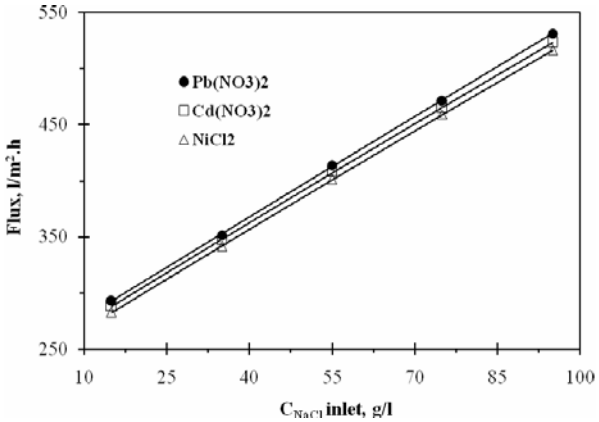

Figure 16 Water flux with draw solution inlet concentration (C_{NaCl} inlet) for different feed solutions (Q_{metals} = 60 l/h, Q_{NaCl} = 12 l/hr, C_{metals} inlet = 150 mg/l, T (feed & draw) = 30 ± 1 °C).

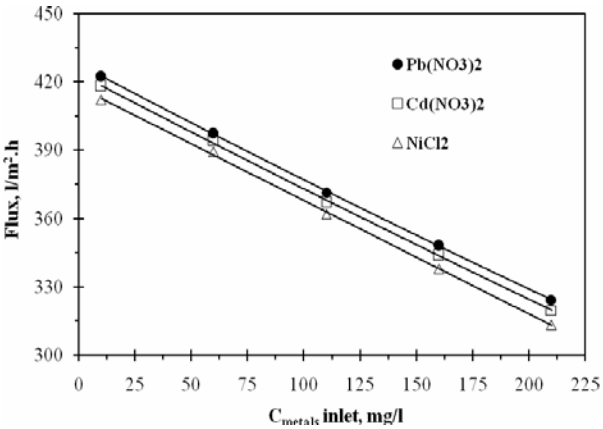

Figure 17 Water flux with feed solution inlet concentration (C_{metals} inlet) for different feed solutions (Q_{metals} = 60 l/h, Q_{NaCl} = 12 l/h, C_{NaCl} inlet = 35 g/l, T (feed and draw) = 30 ± 1 °C).

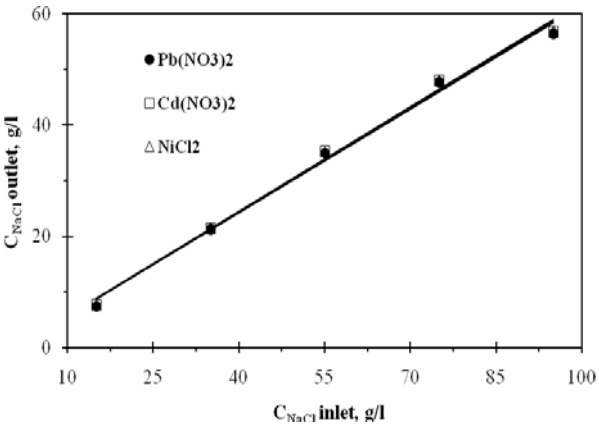

Figure 18 draw solution outlet concentration (C_{NaCl} outlet) with draw solution inlet concentration (C_{NaCl} inlet) for different feed solutions (Q_{metals} = 60 l/h, Q_{NaCl} = 12 l/h, C_{metals} inlet = 150 mg/l, T (feed & draw) = 30°C ± 1).

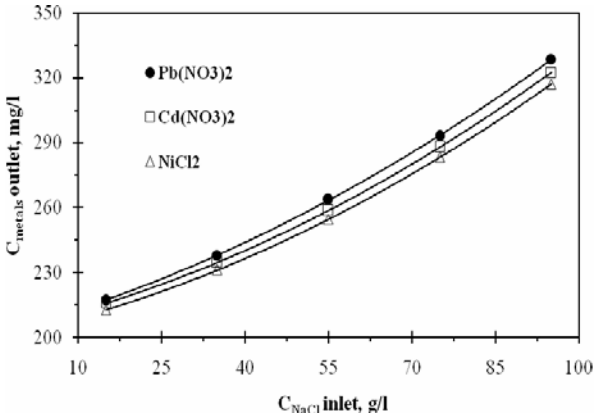

Figure 19 Feed solution outlet concentration (C_{metal} outlet) with draw solution inlet concentration (C_{NaCl} inlet) for different feed solutions (Q_{metals} = 60 l/h, Q_{NaCl} = 12 l/h, C_{metals} inlet = 150 mg/l, T (feed & draw) = 30 ± 1 C).

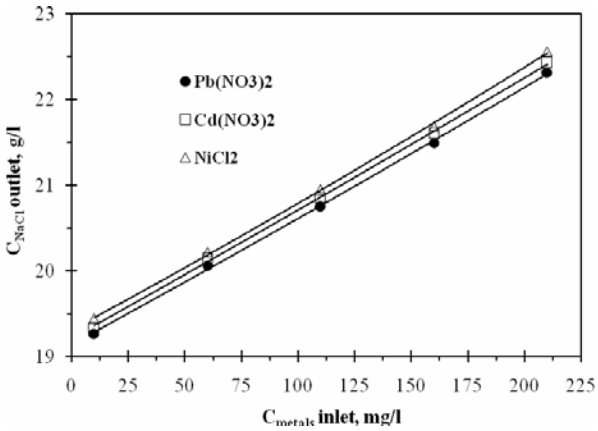

Figure 20 Draw solution outlet concentration (C_{NaCl} outlet) with feed solution inlet concentration (C_{metals} inlet) for different feed solutions (Q_{metals} = 60 l/h, Q_{NaCl} = 12 l/h, C_{NaCl} inlet = 35 g/l, T (feed & draw) = 30 ± 1 °C).

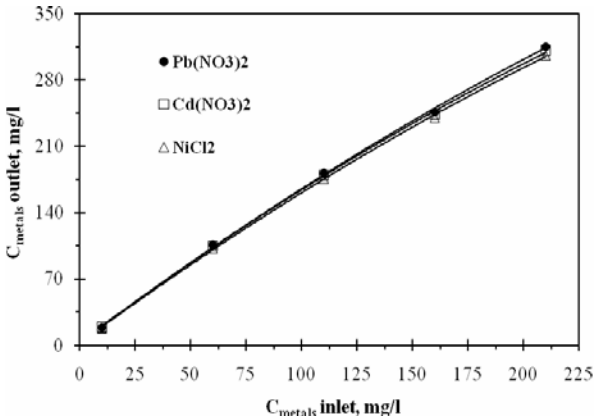

Figure 21 Feed solution outlet concentration (C_{metals} outlet) with feed solution inlet concentration (C_{metals} inlet) for different feed solutions (Q_{metals} = 60 l/h, Q_{NaCl} = 12 l/h, C_{NaCl} inlet = 35 g/l, T (feed & draw) = 30 ± 1 °C).

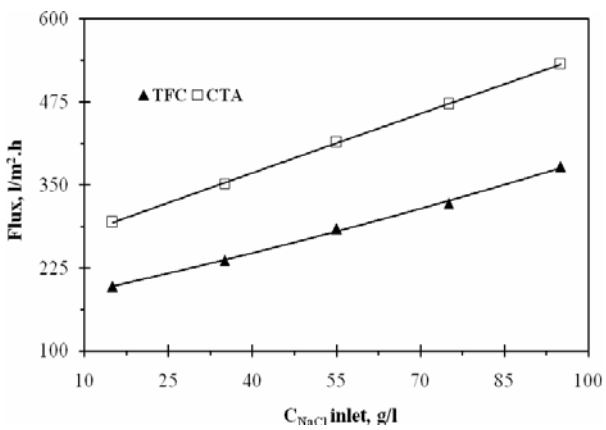

Figure 22 Water flux with draw solution inlet concentration (C_{NaCl} inlet) for $Pb(NO_3)_2$ feed solution and different types of membrane (Q_{metals} = 60 l/h , Q_{NaCl} = 12 l/h , C_{metals} inlet = 150 mg/l, T (feed & draw) = 30 ± 1°C) .

Reverse Osmosis process

Figure 23 illustrates the effect of sodium chloride feed flow rate on water flux. Increasing the brine feed flow rate prevents the concentration build up in the solution at the vicinity of the membrane surface, and result in increasing of driving force ($\Delta P - \Delta\pi$). Thus water flux increased with the increase in feed flow rate.

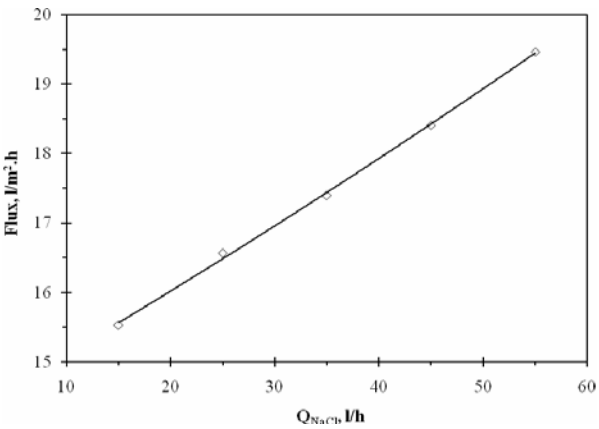

Figure 23 water flux with feed solution flow rate (Q_{NaCl}) (C_{NaCl} inlet = 9000 mg/l, T = 30 ± 1 °C, P = 9.5 bar, pH = 6.5)

Conclusions

The following conclusions could be drawn from the present study:

1- Forward osmosis process is a convenient method and economic for recovery of water from waste water with heavy metals.

2- Different types of heavy metals ($Pb(NO_3)_2$, $Cd(NO_3)_2$ and $NiCl_2$) used as a feed solution and it was found that the order of water flux for this heavy metals was :

$$Pb(NO_3)_2 > Cd(NO_3)_2 > NiCl_2$$

3- The water flux production from the osmosis cell for TFC and CTA is mainly affected by the increase of concentration of draw solution. The water flux decreases with the increase in flow rate of draw solution and increase when increase in temperature of draw solution.

4- The water flux production from the osmosis cell for TFC and CTA decrease with the increase in concentration of feed solution and increase with the increase in flow rate of feed solution and decrease with increase in temperature of feed solution.

5- Cellulose triacetate (CTA) membrane gave better results than the thin film composite (TFC) membrane. Therefore, CTA membrane prefers more in the forward osmosis process.

6- Reverse osmosis process is a good method to treatment of draw solution to be used again.

References

- Achanai , B., Nattawut , C., Kittiya, P., and Lalita., N., 2008. "Use of Natural Clinoptilolite for the Removal of Lead from Waste Water". Chiang Mai J. SCi. 35(3). P. 447-456.
- Gordon, T.G., Jeffrey, R., and Menachem, E., 2006. "Internal Concentration Polarization in Forward Osmosis: Role of Membrane Orientation". Desalination. 197, P. 1-8.
- Gray, G.T., Mccutcheon, J.R., Elimelech, M., 2006. "Internal Concentration Polarization in Forward Osmosis: Role of Membrane Orientation". Desalination. 197, P. 1-8.
- Howy, N.G., Wanling, T., and Weis. W., 2006. "Performance of Forward Osmosis

Process". Environ. Sci. Technol. 40, P. 2408 – 2413 .

- Jacks, G., Bhatta Charya , P., and Chatterjee , D., 2001. "Artificial Recharge as a Remedial Measure for in Situ Removal of Arsenic from the Groundwater". P. 71-75.
- Jeffery, R., and Menachem, E., 2007. "Modeling water Flux in Forward Osmosis". Alche. j. 53, P. 1736.
- Lee, K.L., Waker, R.W., and Lonsdale, H.K., 1981. "Membranes for Power Generation by Pressure – Retarded Osmosis". J. Membr. Sci. 8 , P. 141 -171.
- Loeb, S., Titelman, L., Korngold, E., and Freiman, J., 1997. "Effect of Porous Support Fabric on Osmosis through a Loeb – Sourirajan Type Asymmetric Membrane". J. Membr. Sci. 129, P. 243 – 249.
- Mccutcheon , J. R., and McGinnis , R. L., 2006." Desalination by A novel Ammonia – Carbon Dioxide Forward Osmosis Process: Influence of Draw and Feed Solution Concentration on Process Performance". J. Membr. Sc. 278, P. 114-123.
- Mccutcheon , J.R., Elimelech, M., 2006." Influence of Concentrative and Dilutive Internal Concentration Polarization on Flux Behavior in Forward Osmosis". J. Membr. Sci. 284, P. 237-247.
- Mccutcheon, J.R., McGinnis, R.L., and Elimelech, M., 2006. "Desalination by Anovel Ammonia – Carbon Dioxide Forward Osmosis Process: Influence of Draw and Feed Solution Concentration on Process Performance". J. Membr. Sci. 278, P. 114 – 123.
- Mehta, G.D., and Loeb, S., 1978. "Internal Polarization in the Porous Substructure of a Semi – Permeable Membrane under Pressure – Retarded Osmosis". J. Membr. Sci. 4, P. 261.
- Mesa, A.A., Gomezand, G.M., and Azpitaite R.U., 1997. "Energy Saving and Desalination of Water". Desalination. 108, P. 43-50.
- Mustafa, H., 2009. "A study of Forward Osmosis Using Various Drawing Agents". M.SC. Thesis, Baghdad University.
- Seppala , A., Lampinen, M.J., 2004. "On the Non- Linearity of Osmotic Flow", Exp. Therm. Fluid Sci. 28, P. 283 – 296.
- Tzahi, Y.C., Amy, E.C., and Menachem, E., 2006. "Forward Osmosis: Principles, Applications, and Recent Developments". Journal of Membrane Science. 281, P.70-87.
- Young, J. C., June, S. C., and Joon, H.K., 2009."Toward a Combined System of Forward Osmosis and Reverse Osmosis for Sea water". Desalination. 249, P. 239-246.

Nomenclature

Symbol	Definition	Units
A	Water Permeability Coefficient	$l/bar.m^2.h$
B	Solute Permeability Coefficient	m /s
C	Concentration of Solute	g mole/l
C_{Metals}	Feed Solution Concentration	mg /l
C_{NaCl}	Draw Solution Concentration	g /l
D	Diffusivity	m^2/s
d_h	Hydraulic Diameter	m
ECP	External Concentration Polarization	
ICP	Internal Concentration Polarization	
J_W	Water Flux	$l/h.m^2$
K	Resistance to salt transport in the Porous Support	m/h
k	Mass Transfer Coefficient	m/s
L	Length of the Membrane Channel	m
l	Membrane Thickness	m
P	Pressure	bar
pH	Hydrogen Ion Concentration	
PRO	Pressure – Retarded Osmosis	
Q_{Metals}	Feed Solution Flow rate	l /h
Q_{NaCl}	Draw Solution Flow rate	l/h
Re	Reynolds number	
R_g	Universal Gas Constant	$bar.m^3/mol.\ k$
Sc	Schmidt number	
T	Temperature	^oC

Greek symbols

Symbol	Definition	Units
Δ	Difference Operator	
ε	Membrane Porosity	
π	Osmotic Pressure	bar
σ	Reflection Coefficient	
τ	Pore Tortuosity	
Φ	Osmotic Coefficient	

Subscript

Symbol	Definition
b	bulk
D	Draw Solution
F	Feed Solution
R	Reject
S	Solute
W	Water

Bubble Size Distribution In Gas-Liquid Dispersion Column

Thamer J. Mohammed
University of Technology
Department of Chem. Eng.
Thamer_jasim@yahoo.com

Fadi Z. Hanna
University of Technology
Department of Chem. Eng.
Baghdad/ Iraq/ P.O.Box 35010

Ihsan B. Hamawand*
University of Koya
Department of Chem. Eng.
Iraq, ihsanbaker@yahoo.com

Abstract

The present work investigates the effect of; superficial air velocities of: 1, 3, and 6 cm/s for two types of perforated distributor on hydrodynamic characteristic in a gas-liquid dispersion column of; air-water, and air-aqueous-n-propanol solution. Bubble distribution, gas holdup, and power consumption are parameters take in consideration. Experimental work was carried out in perspex column of 8.5 cm inside diameter and 1.5 m height. Two types of bubble generator (perforated plate) were fixed at the bottom of the column; plate A (99 holes of 0.5 mm diameter and free area of 0.34%), plate B (20 holes of 1.5 mm diameter and free area of 0.62%). Photographic technique was used to measure the bubble parameters.

The experimental results were represented by two empirical correlations. The gas holdup and the Sauter mean diameter of bubbles were correlated with both the power consumption and the hole diameter of the perforate plate.

Keywords:

Gas-liquid dispersion column, bubble size distribution, gas holdup, and power consumption.

الخلاصة

العمل الحالي دراسة تأثير ، سرعة الهواء الظاهريه (1، 3، و 6 سم / ثا) ونوعين من الموزع الهواء على الخصائص الهيدروديناميكية في عمود تشتت الغاز السائل من نظامين؛ الهواء والماء، والهواء ومحلول بروبانول اعتيادي. معدل توزيع الفقاعات، وكميه الغاز المحتجز، واستهلاك الطاقة اخذت بنظر الاعتبار في هذه الدراسه. وقد أجريت تجارب العمل في العمود بقطر داخلي 8،5 سم وارتفاع 1،5 متر. وقد تم تثبيت نوعين من موزعات الهواء (لوحة مثقبة) في الجزء السفلي من العمود؛ لوحه (ا) (99 ثقب بقطر0،5 مم وكانت مساحه التثقيب تساوي 0،34 ٪)، لوحه (ب) (20 ثقب بقطر 1،5 مم وكانت مساحه التثقيب تساوي 0،62٪). تم استخدام تقنية التصوير الفوتوغرافي لقياس القيم المحدده للفقاعة. كما تم ربط النتائج العملية بمعادلات تحليلية حيث تم ربط كمية الهواء المحتجز ومعدل قطر الفقاعات بالطاقة المستهلكة وقطر موزع الهواء.

Introduction

Bhavaraju et al. (1978) and Heijnen & Riet (1984) are the only researcher's works that take the role of sparger in the evolution of bubble characteristics. Their approach is based on the existence of two zones in the column and three bubble regimes. This study distinguishes the region near the sparger where bubble properties are determined by the bubble formation process and the region in the bulk where they are governed by bulk liquid flow. Krishna and Ellenberger (1996) illustrated that the bubble bed behavior is particularly influenced by the nature of the dispersion. Also admitted that three regimes can be distinguished depending on the gas flow rate; homogeneous, heterogeneous and slug flow regimes. The last one is only observed in small-scale columns. Bouaifi et al. (2001) studied the gas holdup, bubble size, mass transfer coefficient, axial liquid dispersion coefficient, and power consumption in stirred gas-liquid reactors and bubble columns. The liquid was tap water and the gas used for all the experiments was air. Different spargers were used such as; perforated plate, sintered glass porous plate, and perforated flexible membrane. The bubble size was measured using a photographic technique with a CCD high definition camera. It was found that the power consumption has a negative impact on the bubble size in contrarily to its impact on gas holdup, interfacial area, volumetric mass transfer coefficient, and bubble size distribution.

Gas-liquid dispersion column has been extensively used in a wide variety of chemical and biochemical processes. It is particularly used in hydrogenation, oxidation, fermentation, petroleum refining, coal liquefaction, etc., where the overall production rate is often controlled by the gas liquid interfacial mass transfer. An example of a dispersion column is the Gas-liquid dispersion column reactor. It is the type of reactor that do not only provide a significant interfacial mass transfer area but also very simple in design and no mechanical agitator is required, (Mandal et al., 2003). Breakup and coalescence of bubbles play a crucial role in a broad spectrum of multiphase flow processes, such as the evaluation of the bubble size distribution in stirred tanks and bubble columns (Delhaye and Mc Laughlim (2003)).

Mouza et al. (2005) studied the effect of the liquid properties on bubble size distribution in a bubble column equipped with two different fine porous spargers (20, 40 μm). Various liquids were used such as; water, n-butanol 0.6 wt%, n-butanol 1.5 wt%, glycerin 33.3 wt%, glycerin 50 wt%, and glycerin 66.7 wt% and atmospheric air is used as the gas phase for all experiments. Gas holdup, bubble size distribution, and mean Sauter diameter were obtained using high speed video camera.

In bubble columns two main regimes can be distinguished. The homogeneous bubbly flow regime, encountered at low gas velocities with small holes sparger, it is characterized by narrow bubble size distributions and a uniform spatial dispersion of gas hold-up. In this regime, there is no interaction between the bubbles, their motion is mostly vertical. The second regime is the heterogeneous (churn turbulent flow) regime which is observed at higher gas velocities. It is defined by a large bubble size distribution and a high concentration of large bubbles. In this regime the bubble size is governed by the coalescence–break-up equilibrium (Malysa et al., 2005, Mouza et al., 2005, Kantarci et al., 2005, and Dargar and Macchi, 2006).

The aim of the present work is to study the effect of different hydrodynamic parameters in to two systems of gas-liquid dispersion column; air-water and air-aqueous-n-propanol solution. This study mainly focused on the bubble size distribution at variety of conditions.

Experimental Work

The experiments are conducted in a cylindrical semi batch bubble column. The column is made of perspex with an inside diameter of 0.085 m and a height of 1.5 m as shown in **Fig.1**. Two types of perforated plates are used as a multiple-orifice nozzle; plate (A) with 99 holes of 0.5mm diameter and free area of 0.34% and plate (B) with 20 holes of 1.5 mm diameter and free area of 0.62%.

Water and aqueous n-propanol solution of 0.6 wt% were presented as the liquid phase and air as the gas phase. All the experiments were conducted at ambient temperature of 25°C and atmospheric pressure. Each experiment started by filling the column with an appropriate liquid phase up to 130 cm above the perforated plate. The gas phase was injected and distributed into the liquid phase by passing it through the perforated plate.

A high speed digital video camera is used for direct flow visualization, bubble size and gas holdup measurements. The air was passed in to the column at a superficial velocity of 1, 3, and 6 cm/s. Three pictures were taken from different angles of the column, the part above the distributor, at a recording speed of 30 pictures per second. The images were analyzed thoroughly to

predict quantitative information about the bubble size distribution and the average gas holdup.

An ellipse shape was approximated for the bubbles where the major and the minor axes were computed by software. The equivalent diameter of a spherical bubble with the same volume of an ellipsoidal bubble shape was computed by Eq. (1), (Colella et al. (1999), Polli et al. (2002), and Bouaifi et al. (2001)).

$$d_{Bi} = \sqrt[3]{a^2 b} \qquad (1)$$

An average number of bubbles were calculated for the three pictures in each experiment, using statistical calculations (Tse et al. (2003), and Hebrard et al. (1996)).

The most important parameter characterizing hydrodynamics behavior of a gas-liquid dispersion is the average gas holdup volume; this was calculated by Eq. (2) which it is essential for the design and the scale-up purposes (Mouza et al. 2005).

$$\varepsilon_g = \frac{H_F - H_L}{H_F} \qquad (2)$$

The mean Sauter diameter, defined by Eq. (3), (Bouaifi et al. 2001):

$$d_{vs} = \frac{\sum n_i d_{Bi}^3}{\sum n_i d_{Bi}^2} \qquad (3)$$

The total power consumption is related to the total gas pressure drop according to the equation (4) (Bouaifi et al. 2001):

(4)

$$\left(\frac{P_g}{V}\right)_{tot} = \frac{Q\Delta P_s}{V} = \frac{Q(\rho_l gH + \Delta P_s)}{V} = \frac{(\rho_l gH + \Delta P_s)U_g}{H}$$

In a perforated plate, the specific sparger

$$\left(\frac{P_g}{V}\right)_{tot.} = \rho_l g U_g \qquad (5)$$

pressure drop can be neglected. The specific power consumption is determined equation (5):

Results And Discussion

Air-Water System

The bubble size distributions (BSD) are presented in **Fig. 2** for air-water system and for both perforated plates A and B. At superficial gas velocity of 1 cm/s, the photographic film was analyzed, the bubble diameter varied between 1.2 to 10.1 mm for perforated plate (A), with mean diameter of 7.037 mm and standard deviation of 2.588 mm, and 1.8 to 11.2 mm for the perforated plate (B), with mean diameter 8.522 mm and standard deviation of 2.473 mm. There is an increase in the bubble mean diameter from 7.037 to 8.522 mm with the increase in the perforated plate diameter, this because the bubble is born at larger size at the outlet of the sparger which lead to produce less number of bubbles.

Similar analysis done for the both superficial gas velocities of 3 and 6 cm/s. As presented in the **Figs. 3 and 4** the mean diameters for both perforated plates (A) and (B) for the velocity of 3 cm/s are 8.527 and 8.913 mm and the corresponding standard deviations are 2.525 and 2.453 mm as respectively. Also, the mean diameters for both perforated plates for the velocity of 6 cm/s are 9.241 and 9.9806 mm and the corresponding standard deviations are 2.383 and 2.476 mm. The comparison between the bubble mean diameter for the three superficial gas velocities; 1, 3, and 6 cm/s show an increase in the bubble mean diameter from 7.037 to 9.241 mm as shown in **Fig. 5**. This lead to a conclusion that there is coalescence happening as the superficial gas velocity increases. Also, not only the holes diameter controls the size of the bubbles at the outlet of the sparger but also the gas velocity. The coalescence phenomena cause a decrease in the bubble rise velocity and decrease in the number of bubbles as shown in **Figs. 6 and 7**. As reported by Colella et al., 1999 the increase in the superficial gas velocity may lead to produce larger bubbles with lower rising velocity.

In the present work, bubbly flow regimes occur when the air velocity was between 1 to 3 cm/s and the transition regime occur when air velocity was at 6 cm/s (Barnea et al. 1980).

Air-Water-N-Propanol Solution System

Figure 8 shows the bubble size frequency distribution for the air-aqueous n-propanol system at 1cm/s superficial gas velocities. The bubbles diameter varied between 2.1 to 9.8 mm and 2.5 to 10.2 mm with mean diameters of 6.859 and 6.998 mm and standard deviations of 2.216 and 2.087

mm, for both perforated plates (A) and (B) respectively. It is clear from these results that the bubbles mean diameter has changed very little from 6.859 to 6.998 mm with the increase in the holes diameter in the perforated plates; this is because the addition of n-propanol to water led to inhibit the effect of the perforated holes diameter on the bubbles diameter at the outlet of the sparger. The comparison between the mean diameter resulted from water alone (7.037 mm) and from n-propanol-water system (6.859 mm), it show little change. In addition, the number of bubbles were increased with the addition of n-propanol because the addition of n-propanol to water led to increase in the breakage rate of the bubbles for a fixed velocity. This also led to increase in gas holdup as shown in **Fig. 14**. For the two higher superficial gas velocities (3, and 6 cm/s) as reported in **Figs. 9 and 10**, the mean diameters at superficial gas velocity of 3 cm/s are 6.4608 and 6.4804 mm, and the corresponding standard deviations are 2.127 and 2.508 mm for both perforated plates (A) and (B) respectively.

The mean diameters at superficial gas velocity of 6 cm/s are 4.6646 and 5.2604 mm, and the corresponding standard deviations are 1.657 and 1.846 mm for both perforated plate (A) and (B) respectively. These results show that the increasing in gas velocity led to decrease in the bubbles mean diameter from 6.859 to 4.664 mm. This also resulted in a significant increase in the number of bubbles with the increase in gas velocity as the holes diameter in the perforated plate get smaller. This is because of faster breakage rate with the increase in gas velocity due to enhancement of bubble-bubble interactions as shown in **Figs.11 and 12**. In fact, increasing the superficial gas velocity leads to smaller bubbles with lower rising velocity (Colella et al., 1999), and the coalescence occurs onto the sparger surface and continue during the movement of the bubbles through the bulk of the liquid (Mouza et al., 2005).

It is well known that the addition of few amounts of long aliphatic alcohol molecules (e.g. n-propanol) to water leads to inhibition of coalescence phenomena. This is because these molecules are composed of a hydrophobic part (carbon chain) and a hydrophilic part (polar group). Thus surface tension gradient forces are created and immobilize the gas-liquid interface so that coalescence is hindered. Aqueous alcohol solutions produce the same effect as industrial organic mixtures on the bubble coalescence and can serve as a model fluid.

The mean bubble size, Sauter mean diameter, depends on the liquid properties which may either promote (e.g. water) or inhibit (e.g. water-n-propanol mixture) coalescence of the primary bubbles formed on the sparger surface as shown in **Figs. 5 and 13**. It is generally admitted that coalescence occurs in three steps, i.e., collision, liquid film drainage and rupture. When two bubbles collide, a liquid film formed due to the small amount of liquid trapped between them. This begins to drain until it is become sufficiently thin to be ruptured due to an instability mechanism. Also bubbles coalescence is a function of the contact time between two bubbles which depends on the bubble rising velocity, bubble size and the turbulence intensity (Chaudhari and Hofmann, 1994).

Gas holdup versus superficial gas velocity is shown in **Fig. 14**, both perforated plates (A) and (B) exhibit quite similar behaviors in aqueous n-propanol solution and air/water system. The perforated plate (A) forms smaller bubbles than the perforated plate (B), as coalescence is suppressed this may preserve these small bubbles within the column leading to increase in the holdup. This may also be due to the decrease in the bubble rise velocity due to the reduction in the drag coefficient caused by the accumulation of solute molecules at the interface (Levan and Newman (1976)).

The variation of gas holdup versus the power consumption are shown in the **Figs. 15 and 16**, for air-water and air-aqueous n-propanol solution systems for the two perforated plates A and B. The increase in the gas holdup led to increase in the power consumption for both systems and for the both perforated plates A and B. This is due to increase in the gas velocity, however it can be clearly seen that the same gas hold up can be achieved with less power consumption by adding of surfactant to the water.

The variation of the bubble Sauter diameter with the total specific power consumption is shown in **Figs. 17 and 18** for both air-water and air-aqueous n-propanol solution systems for the two perforated plates A and B. The variation of Sauter mean diameter depends on the system and the kind of gas spargers used. For air-water system, the Sauter means diameter was increased with the increasing in the power consumption for both perforated plates A and B, in contrary for the air-aqueous n-propanol solution system, the Sauter mean diameter decreased with increasing power consumption for the two perforated plates

A and B. These figures show that the mean Sauter diameter decreased at less power consumption by the addition of surfactant such as n-propanol. As a conclusion, better performance of a dispersion column with less power consumption can be achieved by the addition of n-propanol to the water.

Empirical Correlations

The experimental results are represented by empirical correlations using a computer program named Statistical. The experimental correlations relating the gas holdup and Sauter mean diameter to the specific power consumption and Perforated plate hole diameters for the both systems. These are:

- **For Air-Water System**

The correlation for Gas holdup;

$$\varepsilon_g = -0.011012 + 0.00101\left(\frac{\rho_g}{V}\right) - 15.349\, d_H - 1*10^{-6}\left(\frac{\rho_g}{V}\right)^2 + 0.0655653\, d_H^2 - 0.036932\left(\frac{\rho_g}{V}\right) d_H \quad (6)$$

Correlation coefficient = 0.917
Average error = 10.6%
Standard deviation = 0.0139

The correlation for Sauter mean diameter of bubbles;

$$d_{vs} = 6.2526 + 0.006361\left(\frac{\rho_g}{V}\right) + 1108.939 d_H - 1*10^{-6}\left(\frac{\rho_g}{V}\right)^2 + 2.3182 d_H^2 - 1.1529\left(\frac{\rho_g}{V}\right) d_H \quad (7)$$

Correlation coefficient = 0.962
Average error = 2.13%
Standard deviation = 0.202

- **For Air-Aqueous N-propanol Solution System**

The correlation for Gas holdup;

$$\varepsilon_g = 0.00103 + 0.001164\left(\frac{\rho_g}{V}\right) - 4.6511 d_H - 1*10^{-6}\left(\frac{\rho_g}{V}\right)^2 + 0.075572 d_H^2 - 0.064265\left(\frac{\rho_g}{V}\right) d_H \quad (8)$$

Correlation coefficient = 0.97
Average error = 8.15%
Standard deviation = 0.0153

The correlation for Sauter mean diameter of bubbles;

$$d_{vs} 7.08193 + 0.001019\left(\frac{\rho_g}{V}\right) - 104.189 d_H - 1*10^{-6}\left(\frac{\rho_g}{V}\right)^2 - 0.12599 d_H^2 + 0.97587\left(\frac{\rho_g}{V}\right) d_H \quad (9)$$

Correlation coefficient = 0.996
Average error = 0.93%
Standard deviation = 0.0621

The term $(P_g/V)^2$ in Eqns. (6,7,8 and 9) can be neglected because the effect of this term is very small.

Figure 19 and **Fig. 20** show the relation between the experimental and the predicted gas holdup and Sauter mean diameter respectively. The results good agreements with a maximum error around 10%.

The present experimental data is compared with the correlations predicted by Bach & Pilhofer 1978 and Hikita et al. 1980. In general, the experimental data were found to deviate considerably from proposed empirical models as shown in **Figs. 21 and 22**. The predicted values of gas holdup for the air-water system showed a deviation from our experimental data of 23% and 38% for the two plates respectively. Similar results have been predicted for the air-aqueous n-propanol sol. (0.6 wt %), the deviation were 26% and 54% for both plates respectively. The deviation in the correlations that estimate the gas holdup as published by Bach and Pilhofer (1978) was may be due to the difference in conditions; where D_c>0.1 m and H_L>1.2m, same reason for the data predicted by the correlations by Hikita el a. (1980), where U_g=0.042-0.38 m/s, D_c=0.1m and H_L=0.65m.

Figures 23 and 24 show the comparison between the correlations prediction by Akita & Yoshida (1974) and Bouaifi el a. (2001) and the experimental data from this research regards the Sauter mean diameter values. For air-water system the deviation were around 22% and 51% for both plated respectively. For air-aqueous n-propanol solution (0.6 wt%), the deviation were little smaller around 13% and 29% for both plated respectively, as shown in figures (23 and 24). This deviation in Sauter mean diameter estimated by the correlations of Akita and Yoshida (1974)

may be due to the condition used of D_c up to 0.3 m, U_g up to 0.07 m/s and single-orifice sparger. The correlations conditions for the study published by Bouaifi et al. (2001) were U_g=0.0025-0.04 m/s, D_c=0.15-0.2m and H_L=2m.

Conclusions

It was found that the type of the liquid phase is the main factor that affects the bubble size distribution and the gas holdup. Power consumption is decreased with the addition of surfactant (n-propanol) compared to water alone at the same output. The values of Sauter mean diameter increased due to increase in the superficial air velocity for air-water system, in contrary to air-aqueous n-propanol solution. Perforated plate A gave a lower bubble diameter and a higher gas holdup compare to perforated plate B.

References

Akita, K., and Yoshida, F., (1974) ”Bubble Size. Interfacial Area, and Liquid Phase Mass Transfer Coefficients in Bubble Columns”,Ind. Eng. Chem. Proc. Des. Dev., 13, 84.

Bach, H.F., and Pilhofer, T., (1978) ”Variation of Gas Holdup in Bubble Columns with Physical properties of Liquids and Operating Parameters of Columns”, Germ. Chem. Eng., 1, 270. (Citied in Reference Shah et al. 1982).

Barnea, D., Shoham, O., Taitel, Y., (1980) ”Flow Pattern Characterization in Two Phase Flow by Electrical Conductance Probe”, Int. J. Multiphase Flow, 6, 387.

Bhavaraju, S.M., Russel, T.W.F., and Blanch, H.W., (1978), ”The Design of Gas Sparged Devices for Viscous Liquid System”, AIChE J., 24, 454-466.

Bouaifi, M., Hebrard, G., Bastoul, D., and Roustan, M., (2001), ”A comparative Study of Gas Holdup, Bubble Size, Interfacial Area and Mass Transfer Coefficients in Stirred Gas-Liquid Reactors and Bubble Columns”, Chem. Eng. and Proc., 40, 97-111.

Chaudhari, R.V., and Hofmann, H., (1994), ”Coalescence of Gas bubbles in Liquids”, Reviews in Chem. Eng., 10(2).

Colella, D., Vinci, D., Bagatin, R., Masi, M., and Baker, E.A., (1999),”A Study on Coalescence and Breakage Mechanisms in Three Different Bubble Columns”, Chem. Eng. Sci., 54, 4767-4777.

Dargar, P.,and Macchi, A., (2006), ”Effect of Surface-Active Agents on The Phase Holdups of Three-Phase Fluidized Beds”, Chemical Engineering and Processing, 45, 764-772.

Delhage, J.-M., and Melaughlin, J.B., (2003), Appendix 4: report of study group on microphysics, Inter. J. of Multiphase Flow 29, 1101-1116.

Hebrard, G., Bastoul, D., and Roustan, M., (1996), ”Influence of Gas Sparger on The Hydrodynamic Behaviour of bubble Columns”, Trans I Chem E., 74(A), 406-414.

Heijnen, J.J., and Riet, K.V., (1984), ”Mass Transfer, Mixing and Heat Transfer Phenomena in Low Viscosity Bubble Column Reactors”, Chem. Eng. J., 28, B21-B42.

Hikita, H., Asai, S., Tanigawa, K., Segawa, K., and Kitao, M., (1980) ”Gas Holdup in Bubble Column”, Chem. Eng. J., 20, 59.

Kantarci, N., Borak, F., and Ulgen, K.O., (2005), ”Bubble column reactors”, Process Biochemistry,40, 2263-2283.

Krishna, R., and Ellenberger, J., (1996), ” Gas Holdup in Bubble Column Reactors Operating in The Churn-Turbulent Flow Regime”, AIChE J., 42, 2627-2634.

Levan, M.D., and Newman, J., (1976), ”The Effect of Surfactant on The Terminal and Interfacial Velocities of a Bubble or Drop” , AIChE J., 22, 695-700.

Malysa, K., Krasowska, M., and Krzan, M., (2005), ” Influence of Surface Substances on Bubble Motion and Collision with Various Interfaces”, Advance in Colloids Interface Science 114-115, 205-225.

Mandal, A., Kundu, G., and Mukerjee, D., (2003), ”Gas Holdup and Entrainment Characteristics in a Modified Dawn Flow Bubble Column with Newtonian and Non-Newtonian Liquid”, Chem. Eng. and Processing, 42,777-787.

Mouza, A.A., Dalakoglou, G.K., and Paras, S.V., (2005),"Effect of Liquid Properties on The Performance of Bubble Column Reactors with Fine Pore Spargers", Chem. Eng. Sci., 60, 1465-1475.

Polli, M., Di Stanislao, M., Bagatin, R., AbuBakr, E., and Masi, M., (2002), "Bubble Size Distribution in The Sparger Region of Bubble Columns", Chem. Eng. Sci., 57,197-205.

Rodionow, A.I., and Patzelt, H., (1969),Wiss. Z. Tech. Hochsch. Lewna-Merseburz, 11, 435.

Tse, K.L., Martin, T., McFarlane, C.M., and Nienow, A.W., (2003),"Small Bubble Formation Via a Coalescence Dependent Break-up Mechanism", Chem. Eng. Sci., 58, 275-286.

Notation

a= major axis of ellipsoidal bubble, mm
b= minor axis of ellipsoidal bubble, mm
d_{Bi} = diameter of bubble of size i, mm
d_H= hole diameter of perforate plate, mm
d_{vs} = sauter mean diameter of bubbles, mm
D_c=diameter of column, m
g = acceleration of gravity, m/s^2
H_L = clear liquid height, mm
H_F = aerated liquid height, mm
n_i = number of bubbles of size i
ΔP = gas pressure drop, N/m^2
ΔP_s = sparger pressure drop, N/m^2
P_g = power consumption in aerated liquid, W
Q = gas flow rate, cm^3/s
U_g = superficial gas velocity, cm/s
V = column liquid volume, mm^3
Wt = weight percent of n-propanol in water, %

Greek Symbols

ε_g = gas holdup
ρ = liquid density, kg/m^3

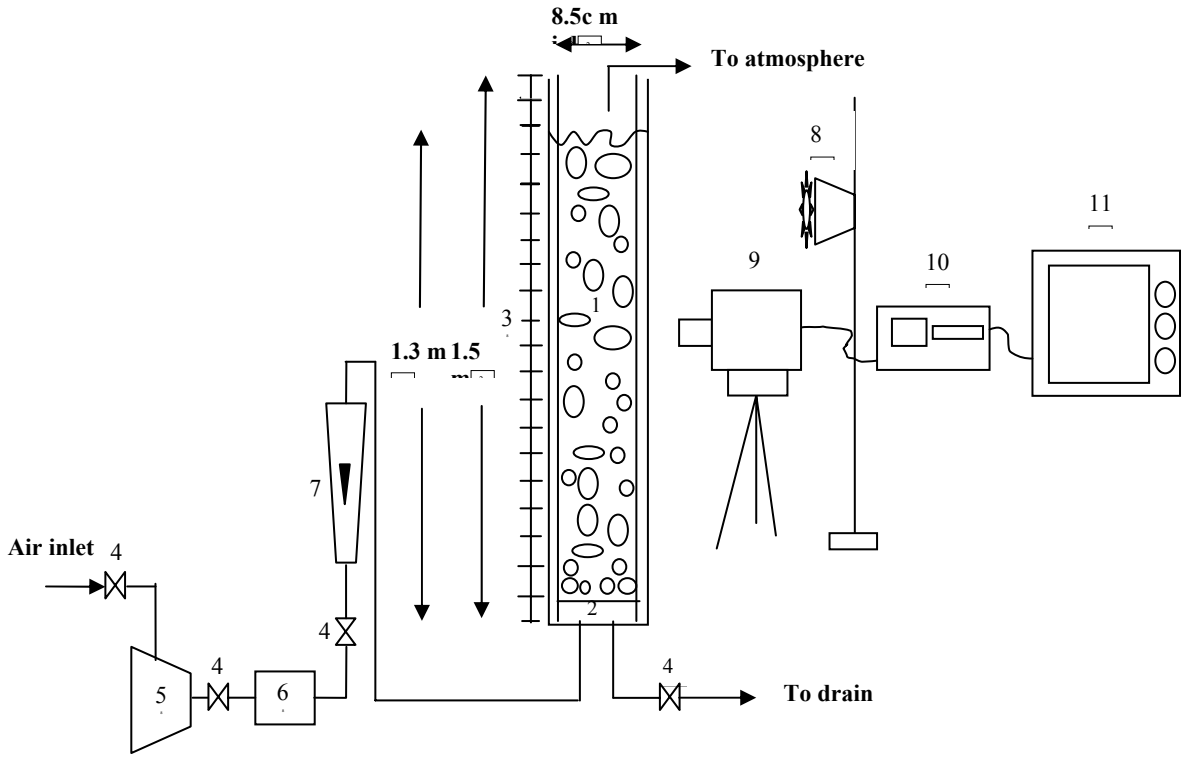

Fig.(1): Experimental set-up: (1) test column: (2) perforate plate: (3) Scale: (4) regulating valves: (5)compressor: (6) air filter:(7) rotameter: (8) electric flash: (9) digital camera: (10) video tape recorder: (11)screen.

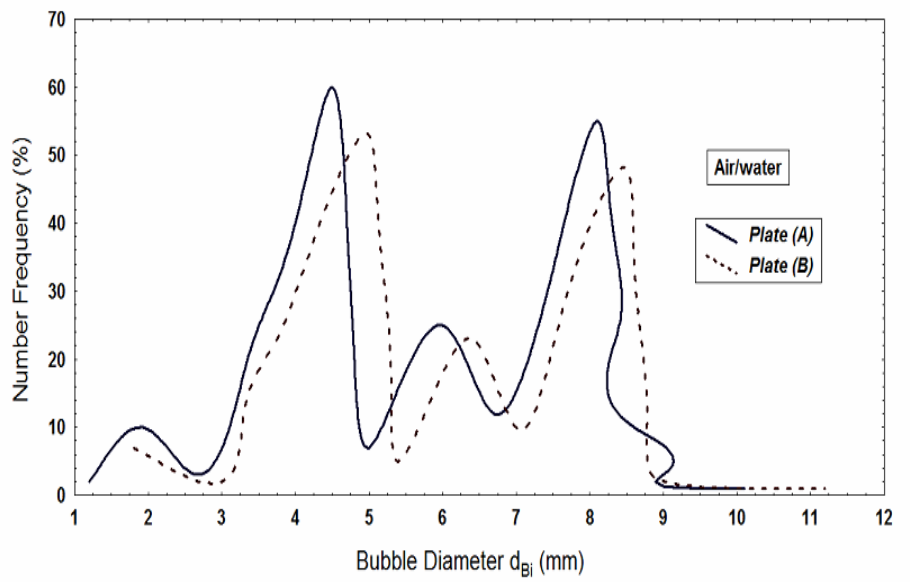

Fig.2: Effect of hole diameter on BSD at (U_g= 1 cm/s) .

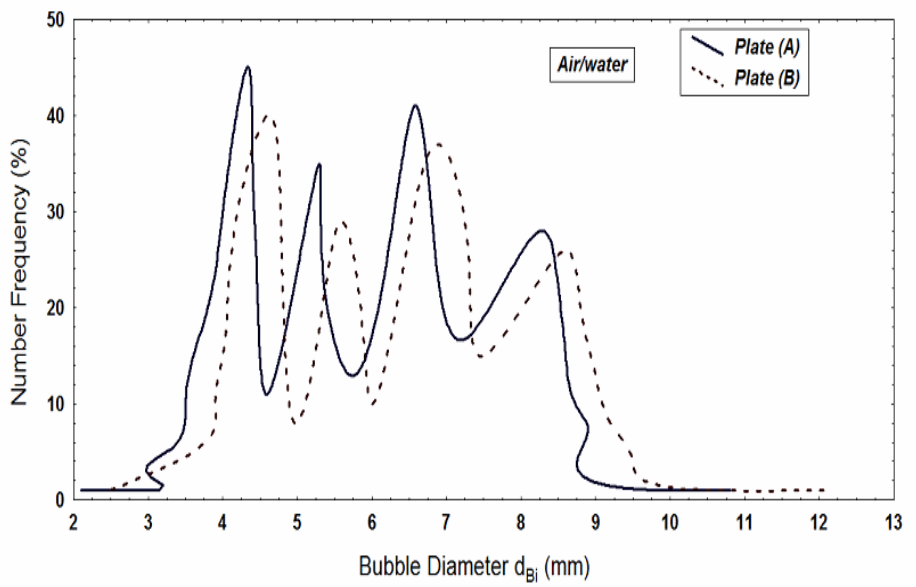

Fig.3: Effect of hole diameter on BSD at (U_g= 3cm/s) .

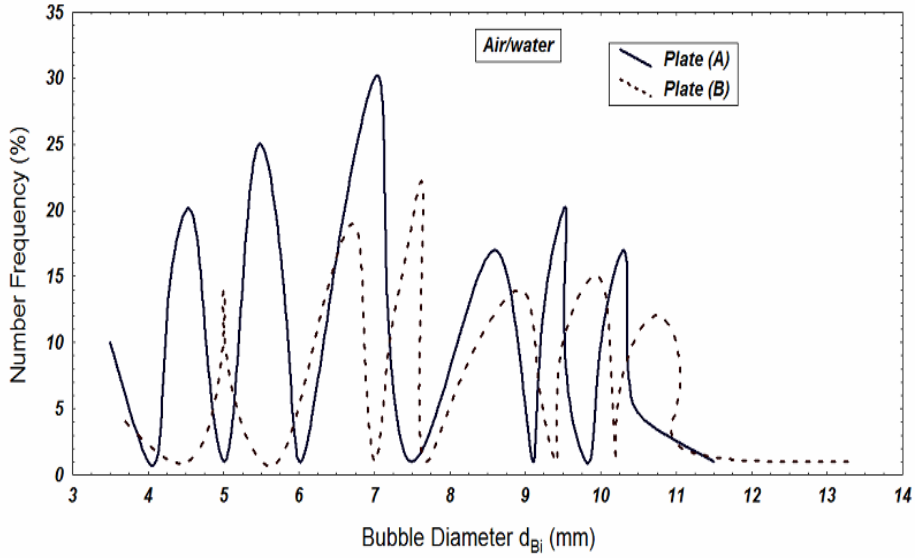

Fig.4: Effect of hole diameter on BSD at (U_g= 6 cm/s) .

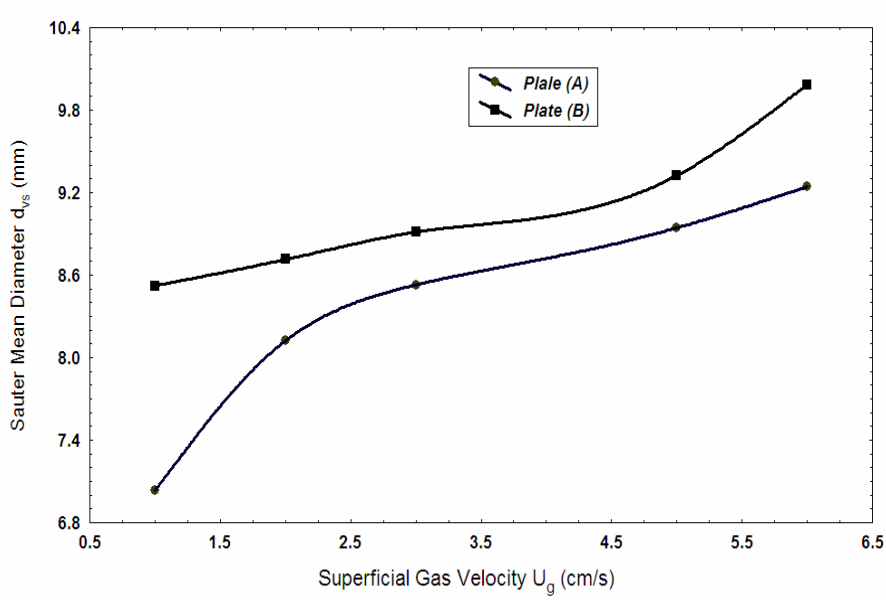

Fig.5: Evolution of d_{vs} with U_g for air-water system.

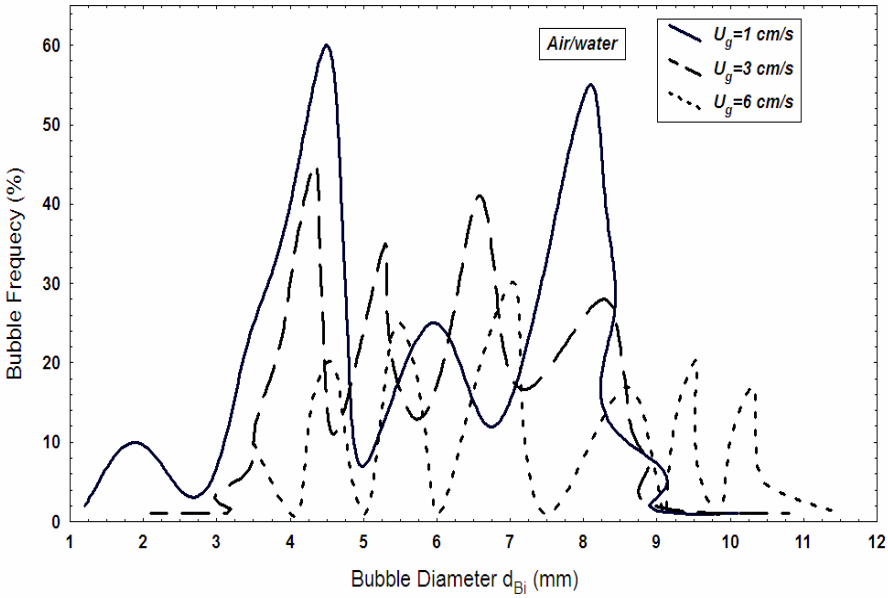

Fig.6: Effect of superficial gas velocity on BSD for (plate A).

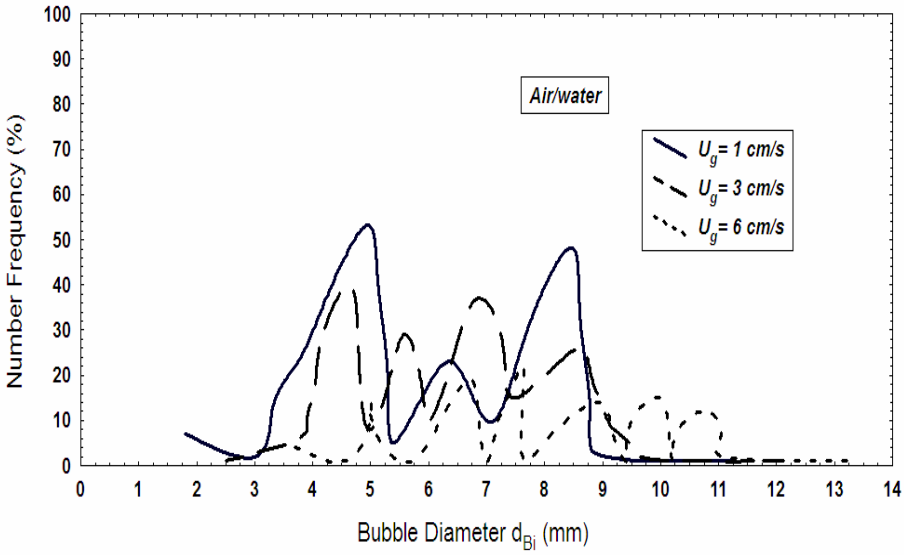

Fig.7: Effect of superficial gas velocity on BSD for (plate B).

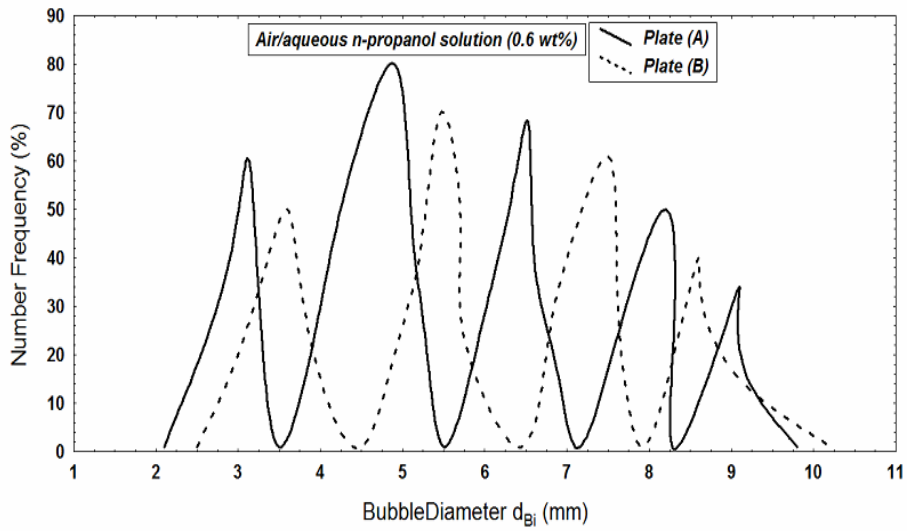

Fig.8: Effect of hole diameter on BSD at (U_g= 1cm/s) .

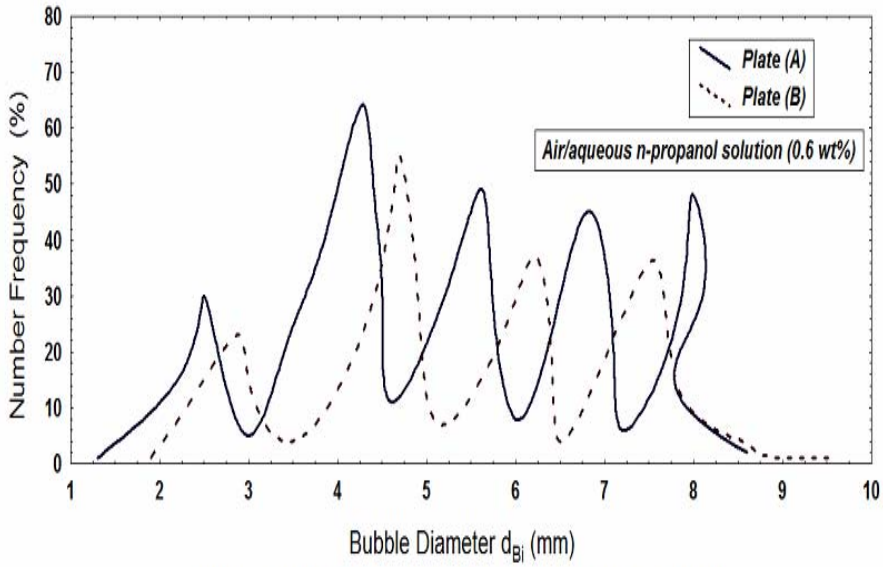

Fig.9: Effect of hole diameter on BSD at (U_g= 3 cm/s) .

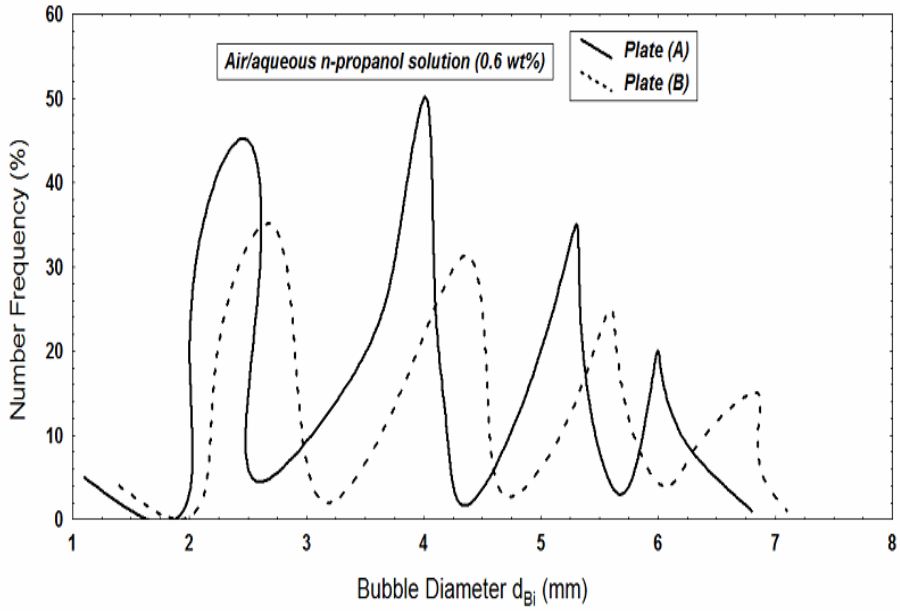

Fig.10: Effect of hole diameter on BSD at (U_g=6 cm/s) .

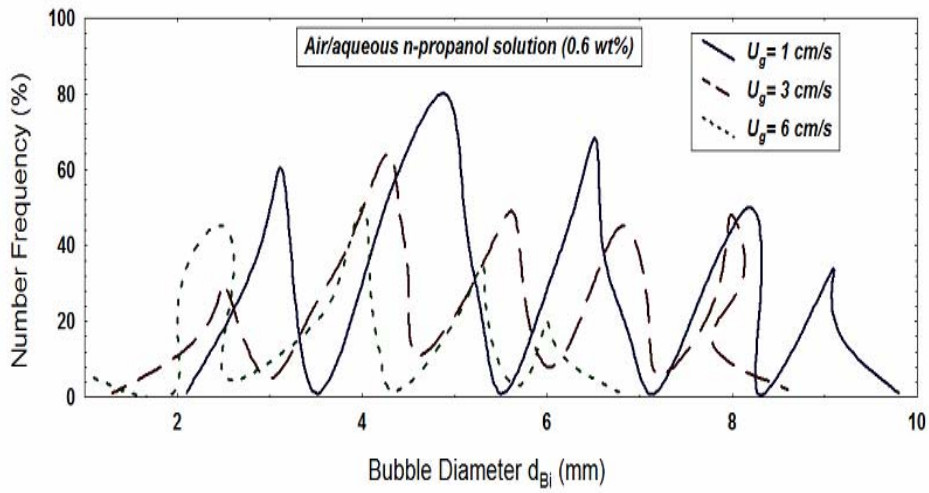

Fig.11: Effect of superficial gas velocity on BSD for (plate A) .

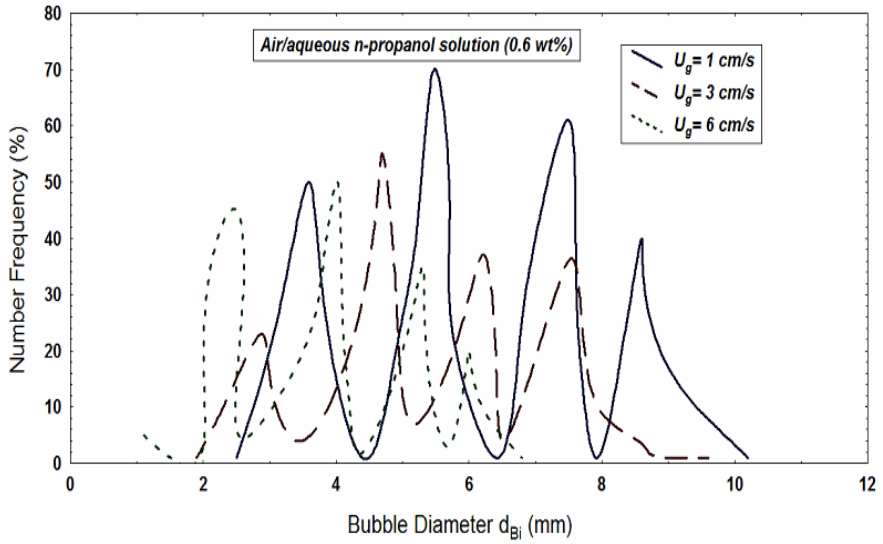

Fig.12: Effect of superficial gas velocity on BSD for (plate B) .

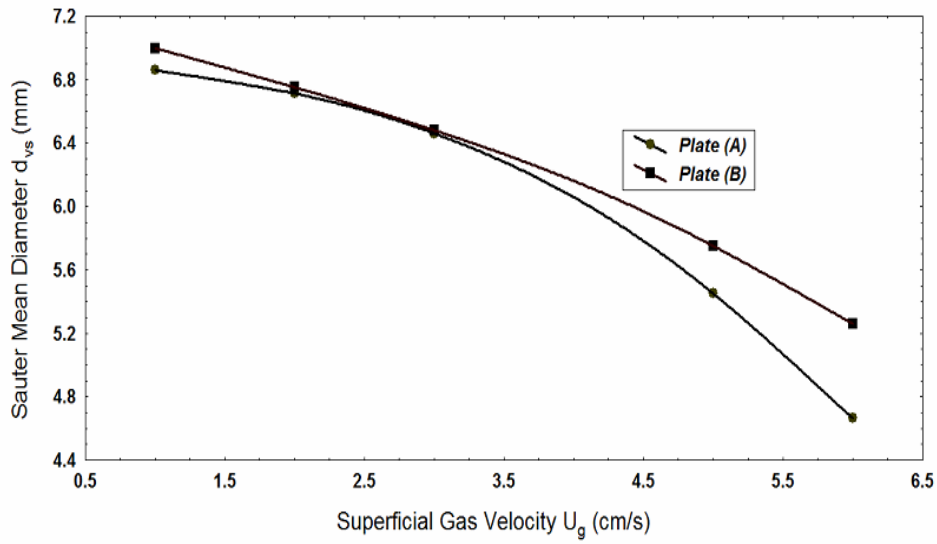

Fig.13: Evolution of d_{vs} with U_g for air/aqueous n-propanol sol. system.

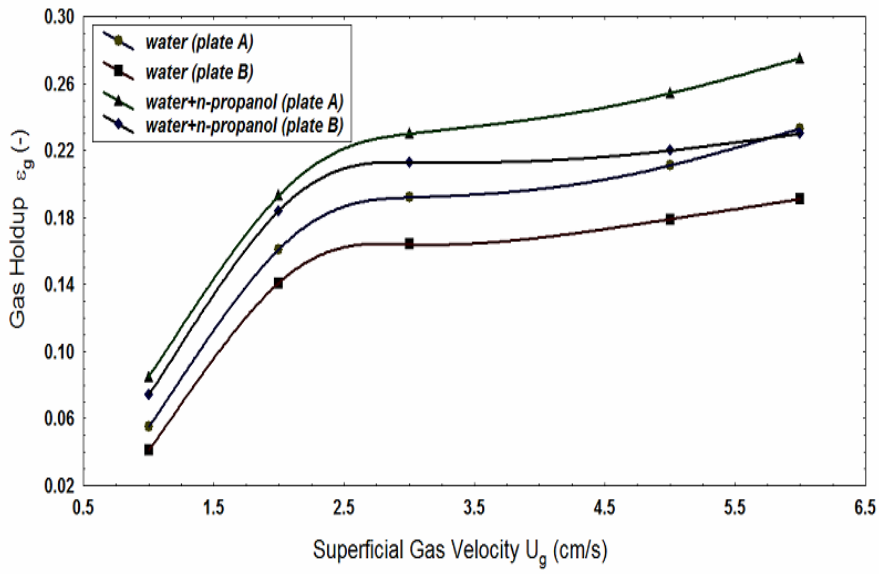

Fig.14: Gas holdup as a function of superficial gas velocity.

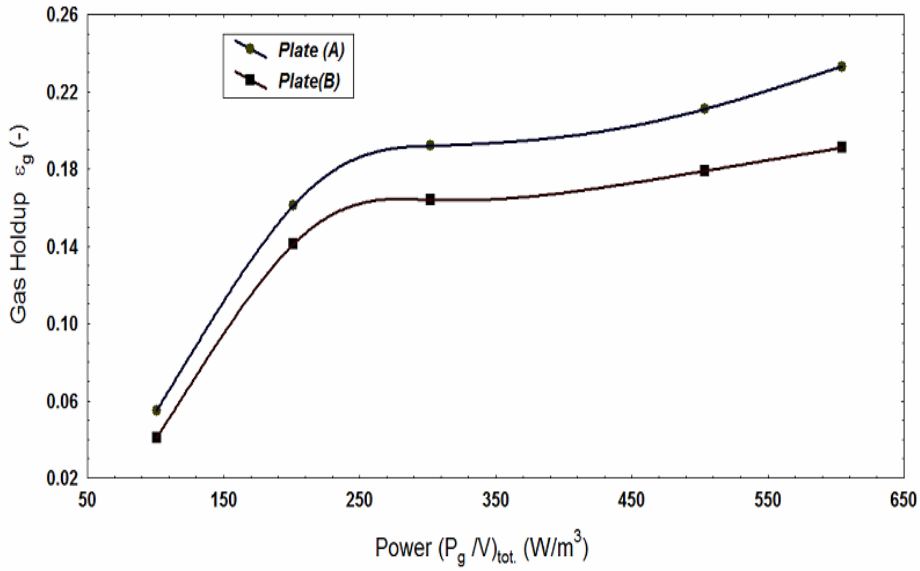

Fig.15: Gas holdup vs. power consum. for air-water system.

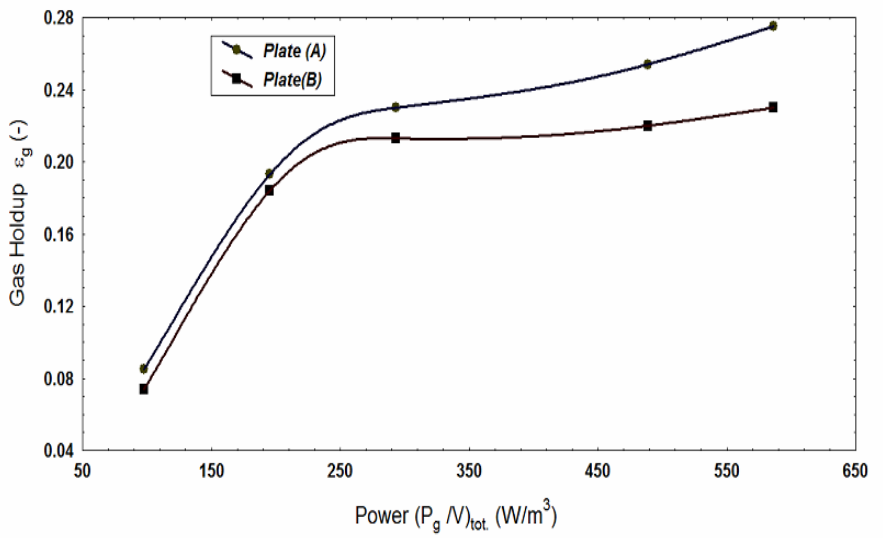

Fig.16: Gas holdup vs. power consum. for air-aqu. n-propanol sol. system.

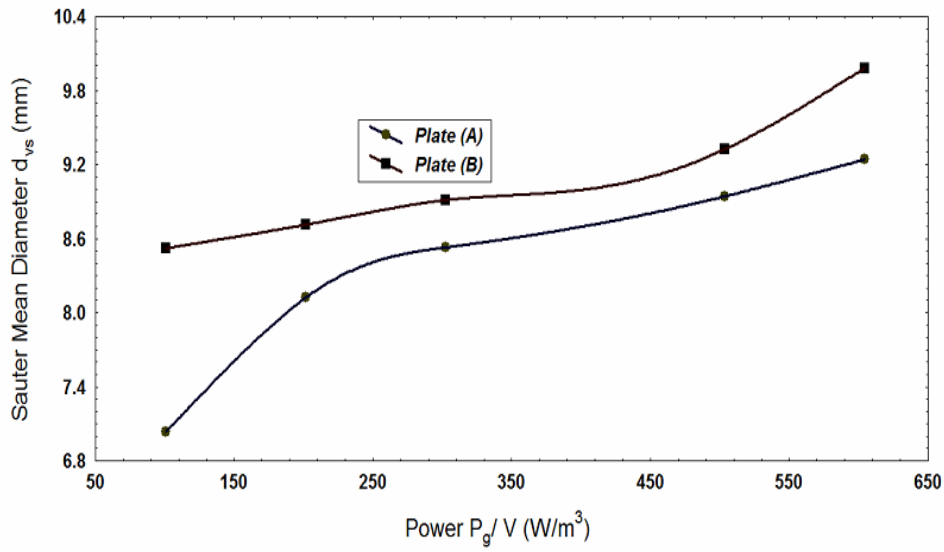

Fig.17: d_{vs} vs. power consum. for air-water system.

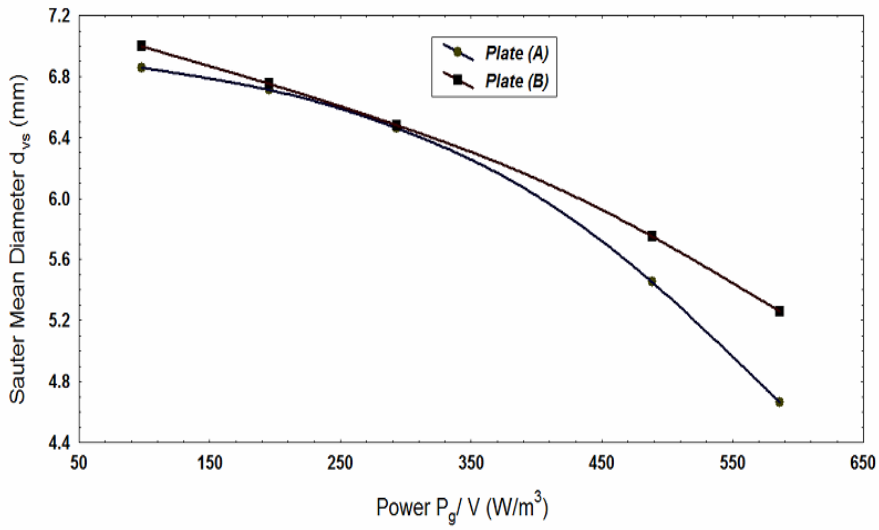

Fig.18: d_{vs} vs. power consum. for air-aqu.n-propanol sol. system.

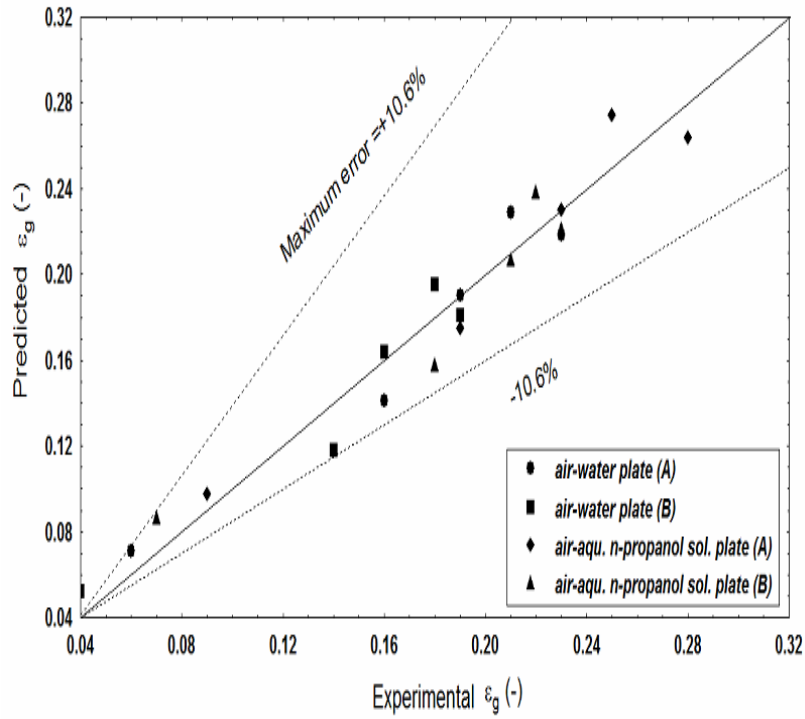

Fig.19: Comparsion between exp. and pred. gas holdup values Eqn.(6&8).

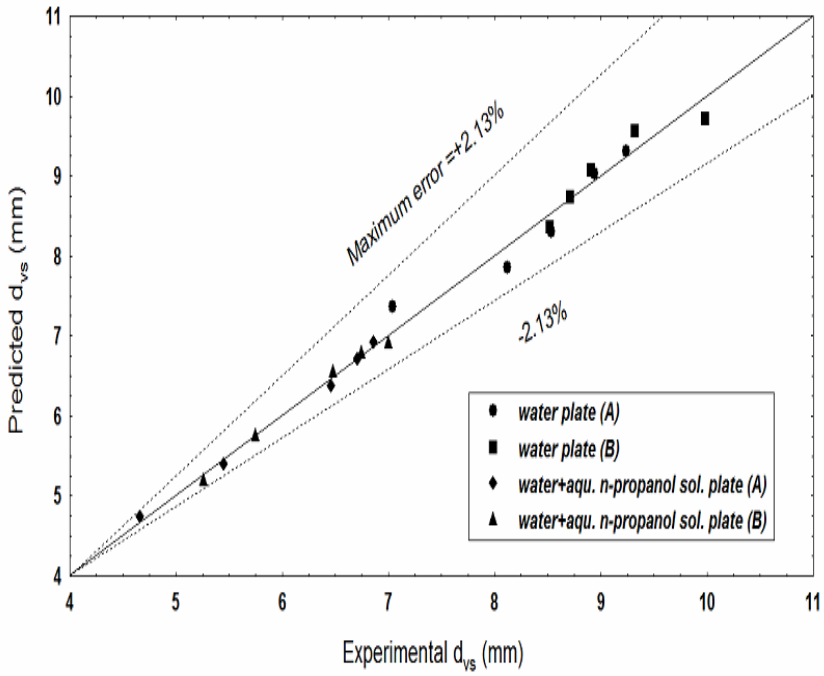

Fig.20: comparsion between exp. and pred. sauter mean dia. values Eqn.(7&9).

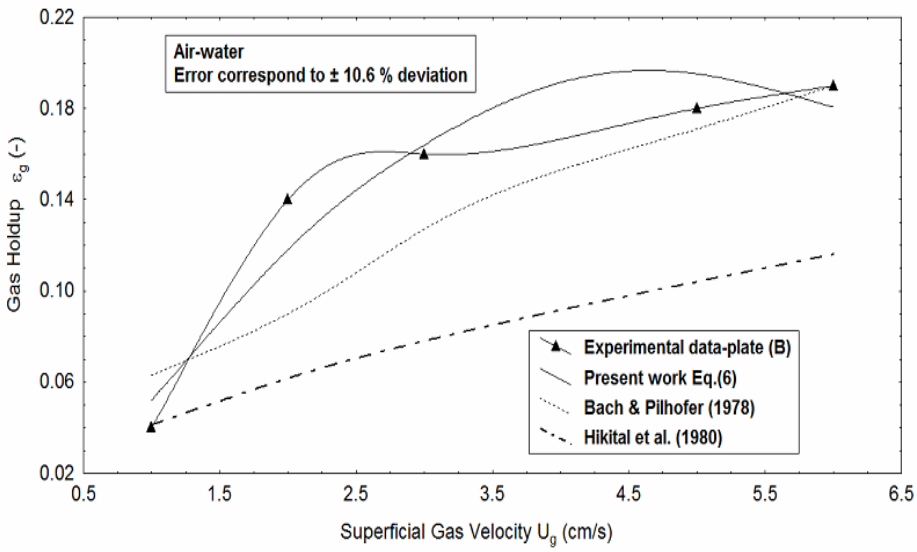

Fig.21: Comparison of the exp.data with others authors work.

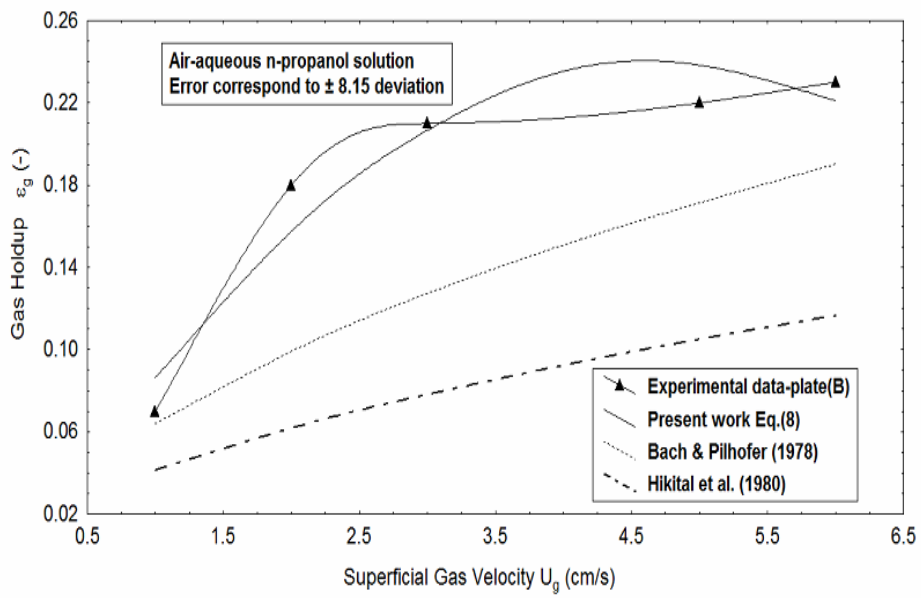

Fig.22: Comparison of the exp.data with others authors work.

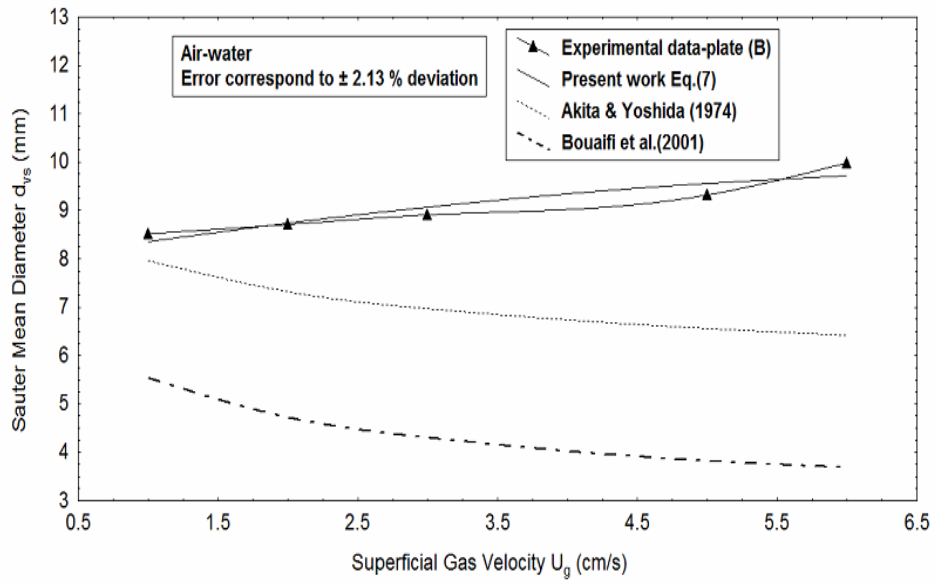

Fig.23: Comparison of the exp.data with others authors work.

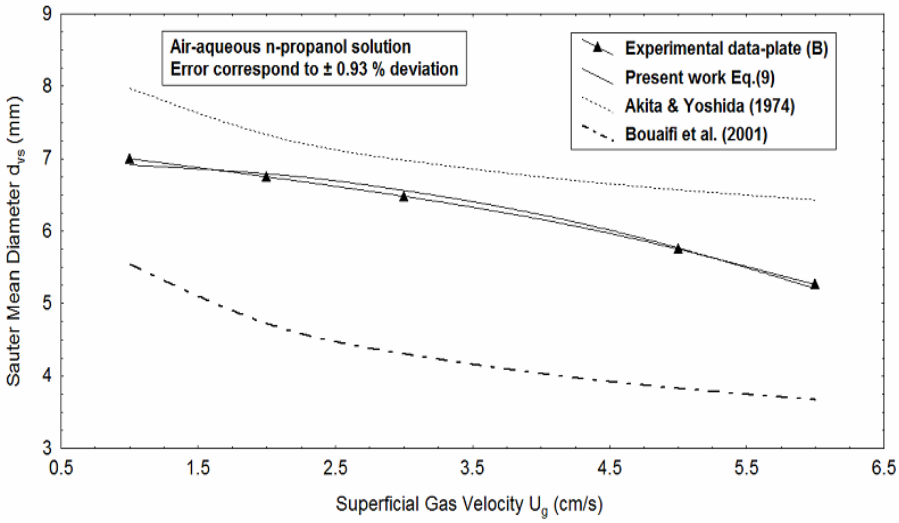

Fig.24: Comparison of the exp.data with others authors work.

Face Identification Using Back-Propagation Adaptive Multiwavenet

Prof. Dr. Waleed Ameen Mahmoud
University of Baghdad/ College of Engineering
Electrical Engineering Department

Ali Ibrahim Abbas
University of Baghdad/ College of Engineering
Electrical Engineering Department

Asst. Prof. Nuha Abdul Sahib Alwan
University of Baghdad/ College of Engineering
Computer Engineering Department

Abstract

Face Identification is an important research topic in the field of computer vision and pattern recognition and has become a very active research area in recent decades. Recently multiwavelet-based neural networks (multiwavenets) have been used for function approximation and recognition, but to our best knowledge it has not been used for face Identification. This paper presents a novel approach for the Identification of human faces using Back-Propagation Adaptive Multiwavenet. The proposed multiwavenet has a structure similar to a multi-layer perceptron (MLP) neural network with three layers, but the activation function of hidden layer is replaced with multiscaling functions. In experiments performed on the ORL face database it achieved a recognition rate of 97.75% in the presence of facial expression, lighting and pose variations. Results are compared with its wavelet-based counterpart where it obtained a recognition rate of 10.4%. The proposed multiwavenet demonstrated very good recognition rate in the presence of variations in facial expression, lighting and pose and outperformed its wavelet-based counterpart.

Keywords: Face Identification, multiwavelet neural network, Back-Propagation Adaptive Multiwavenet

الخلاصة

تمييز الوجوه من المواضيع المهمة في مجال الرؤية الحاسوبية والتعرف على الأنماط وأصبحت مجالا بحثيا نشطا للغاية في العقود الأخيرة. في الآونة الأخيرة استخدمت الشبكة العصبية المتعددة المويجات لتقريب الدالة و التمييز، لكن بحسب علمنا لم تستخدم للتعرف على الوجوه. يقدم هذا البحث نهجا جديدا لتحديد الهوية من خلال الوجه باستخدام (Back-Propagation Adaptive Multiwavenet) الشبكة العصبية المتعددة المويجات التكيفية ذات انتشار تراجعي. تمتلك الشبكة المتعددة المويجات المقترحة بنية مماثلة ل(MLP) مع ثلاث طبقات، غير ان دالة التفعيل تم استبدالها بدالة متعددة المقادير. حققت هذه الشبكة نسبة التمييز 97.75% في تجارب تمت على قاعدة البيانات ORL مع اختلاف في تعابير الوجه، الاضاءة وتدوير الوجه. تمت مقارنة النتائج مع نظيرتها الاحادية المويجة حيث حصلت على نسبة تمييز 10.4%. اظهرت الشبكة المقترحة نسبة جيدة جدا مع وجود اختلاف في الاضاءة، تعابير الوجه وتدوير الوجه وتفوقت على نظيرتها الاحادية المويجة.

1. Introduction

Over the last decade, face recognition has become a popular area of research in computer vision. A general statement of the face recognition problem can be formulated as follows: Given still or video images of a scene, identify or verify one or more persons in the scene using a stored database of faces. A survey of face recognition techniques has been given by (Zhao W., et al., 2003).

In general, face recognition techniques can be divided into two groups based on the face representation they use:

- Appearance-based, which uses holistic texture features and is applied to either whole-face or specific regions in a face image;
- Feature-based, which uses geometric facial features (mouth, eyes, brows, cheeks etc.) and geometric relationships between them.

Among various solutions to the problem (Turk M., et al., 1991) the most successful seems to be appearance-based approaches, which generally operate directly on images or appearances of face objects and process the image as two-dimensional patterns. Most effort in the literature have focused mainly on developing feature extraction methods (Zhao W., et al., 2003), (Zhao W., et al., 1997), (Deniz O., et al., 2003) and employing powerful classifiers such as probabilistic (Moghaddam B., 2002), Hidden Markov models (HMMs) (Othman H., et al., 2003) neural networks (NNs) (Er M.J., et al., 2003), (Er M.J., et al., 2005) and support vector machine (SVM) (Lee K., et al., 2002).

The use of neural networks for face recognition has been addressed in (Pang S., et al., 2005), (Zhang B., et al., 2004), (Fan X., et al., 2005), (Lu X., et al., 2003). Recently, (Li G., et al., 2006) suggested the use of a non-convergent chaotic neural network to recognize human faces. (Lu K., et al., 2006) suggested a semi-supervised learning method that uses support vector machines for face recognition. (Zhou W., et al., 2006) suggested using a radial basis function neural network that is integrated with a non-negative matrix factorization to recognize faces. (Huang L.L., et al., 2006) proposed using two neural networks whose outputs are combined to make a final decision on classifying a face. (Park C., et al., 2006) used a momentum back propagation neural network for face and speech verification.

Back Propagation Wavenet (BPW) is an artificial neural network (ANN) that is integrated with wavelet techniques and has been used successfully in many fields. Instead of conventional nonlinear sigmoid transfer functions, the transfer function of the nodes in a wavelet neural network is wavelet bases. Because wavelet bases are localized in time and frequency, the ability of a BPW in mapping complicated nonlinear functions is enhanced considerably (Yang X., et al., 2009).

(Shen Y., et al., 2004) used BPW for object recognition. (Ensafi A.A., et al., 2007) applied BPW for the determination of sulfide and thiocyanate in real samples such as tap, waste and river waters with satisfactory results. to improve the detection rate for anomaly state and reduce the false positive rate for normal state in the network anomaly detection. (Liu L., et al., 2009) proposed a novel method based on BPW trained by Modified Quantum-behaved Particle Swarm Optimization (MQPSO) algorithm. (Long-yun X., et al., 2008) used BPW for gear faults diagnosis. (Zhao Y.Z., et al., 2009) used BPW for learning the wear out pattern of the milling machine cutters to predict their remaining useful life. (Bin Z., et al., 2010) applied BPW to solve the problem of tunnel surrounding rock deformation prediction.

As an extension of wavelets, a multiwavelet can preserve all the advantages the wavelet has. Furthermore, it can simultaneously have several properties very useful in practical applications such as orthogonality, regularity, symmetry, and compact support, which is impossible for a scalar wavelet. Therefore, the networks using the dilations and translations of a multiscaling function as node functions have better performances which are worth investigating (Jiao L.C., et al. 2001). Based on the considerations above, a model of multiwavelet-based neural network for face identification is used in this paper.

Section 2 provides an introduction of the Multiwavenet. Section 3 presents a face identification system based on a back-propagation multiwavenet classifier. Section 4 presents experimental results. Conclusions are presented in Section 5.

2. Multiwavenet

Suppose a multiplicity-r multiscaling function $\phi(t) = \left[\phi^1(t), \phi^2(t), \ldots, \phi^r(t)\right]^T$ satisfies a dilation equation

$$\phi(t) = \sum_{k \in Z} p_k \phi(2t - k) \tag{1}$$

and the dilations and translations of $\phi^l(t)$s, denoted by $\phi^l_{j,k}(t) = 2^{j/2}\phi^l_{j,k}(2^j t - k)$, l = 1, …, r $k \in Z$, span the scale space V_j $j \in Z$.

We are interested in the case of orthogonal multiscaling functions. In that case, $\{\phi^l_{j,k}(t) \mid l = 1, \cdots, r, \quad k \in Z\}$ form an orthonormal basis of V_j, and the associated multiwavelet $\psi(t) = [\psi^1(t), \psi^2(t), \ldots, \psi^r(t)]^T$ make $\psi^l_{j,k}(t) = 2^{j/2}\psi^l_{j,k}(2^j t - k)$, l = 1,…,r , $k \in Z$, form an orthonormal basis of the orthogonal complementary subspace W_j of V_j in V_{j+1}. From the theory of multiresolution analysis, we know that $\bigcup_{j \in z} V_j = L^2(R)$ and hence, for any $f \in L^2(R)$, there exists a natural number J_0, such that $\|f - f_J\|_2 < \varepsilon, \quad J > J_0$ where $\| \bullet \|_2$ is L^2 norm, ε is an arbitrary positive number, and $f_J \in V_J$

$$f_J = \sum_{l=1}^{r} \sum_{k \in z} \langle f, \phi^l_{J,k} \rangle \phi^l_{J,k}(t) . \tag{2}$$

From the viewpoint of neural networks, f_J can be learned by a neural network, which is called multiwavelet neural network (multiwavenet) because of its connection with the multiwavelet theory though the node functions used are the associated multiscaling functions (Jiao L.C., et al. 2001).

3. The Proposed Face Identification System

The general structure of the proposed face identification system is shown in **Fig. 1**.

Function of each block is clarified below:

- **Preprocessing:** Locating faces in image and extracting the face part only. This is done manually.
- **Normalization:** Histogram equalization of images to reduce the effect of lightning source amplitude's variations.
- **Feature Extraction:** Down sample the image to a low resolution using a bicubic interpolation method and put the result in a one-dimensional feature vector.
- **Classifier:** Multiwavenet classifier is used. After the training is done, the parameters of the multiwavenet classifier, namely weights, translations and dilations are stored and are used in the identification stage when the classifier works in simulation mode.

The processing in both training and identification stages is similar except for the classifier, which works in training mode in the training stage and in simulation mode in the identification stage.

In this section, a classifier for the face identification system is proposed. Each output of the multiwavenet classifier corresponds to a class. The position of the output with the highest value determines the class to which the input belongs. For example if there are five classes, five outputs are needed. During the training phase, each data in the training set is presented to the classifier to the classifier along with its desired output, where desired output for an input belonging to class *c* is an all zero vector with a one in the *c*th position. When a new input is presented to the classifier, the position of the highest value output determines the class.

The architecture of the proposed Back Propagation Adaptive Multiwavenet (BPAMW) is basically the same as the back propagation neural network, except that the sigmoid function of hidden layer node of the back propagation neural network is replaced with two or more scaling functions of a multiwavelet system. For each distinct individual in the training set, an output is needed and for each output a set of weights is required. A competitive layer is added after the output layer. Function of this layer is to produce the final classification result by choosing the output with the highest value among all outputs as the winner and returning its position as the final classification. The architecture of the BPAMW classifier is shown in **Fig. 2**.

The *k*th output of the BPAMW classifier before the competitive layer is

$$y_k(U_s) = \sum_{i=1}^{M} \sum_{L=1}^{r} w_{iLk} \varphi_L \left(\frac{z_{is} - t_i}{\lambda_i}\right) \tag{3}$$
$$k = 1 \cdots K, \quad s = 1 \cdots P$$

$$z_{is} = \sum_{j=1}^{N} v_{ji} u_{js} , \tag{4}$$

where M is the number of multiwavelons, r is the multiplicity of the multiscaling function and each multiwavelon has r wavelons, t_i and λ_i are the translation and dilation of ith multiwavelon's scaling functions respectively, φ_L is the L'th scaling function. $U_s = \{u_{1s}, u_{2s}, \ldots, u_{Ns}\}$ is the sth input vector of the total P input vectors in the training set, N is the number of elements of each input vector (input dimension), z_{is} is the inner product between the input vector U_s and the ith input weight vector $V_i = \{ v_{1i}, v_{2i}, \ldots, v_{Ni} \}$ (weights between input nodes and ith multiwavelon), w_{iLk} is the weight between Lth wavelon of ith multiwavelon and the kth output, $y_k(U_s)$ is the kth output of the network and there are K nodes in the output layer, K should be equal to the number of individuals in the training database.

(Plonka G., et al. 1998) presented an efficient method for creating multi-scaling functions with given approximation order, regularity, symmetry and short support. In second example of their paper, multi-scaling functions with approximation order 4, compact support (0,2), and symmetry was constructed which will be used in this work. Unlike GHM (Geronimo-Hardin-Massopust) multi-scaling functions, these functions have a closed form expression:

$$\phi_1(u) = \begin{cases} \left(-2u^3 + 3u^2\right) & u \in [0,1) \\ (2-u)^2(2u-1) & u \in [1,2] \\ 0 & \text{otherwise} \end{cases} \tag{5}$$

$$\phi_2(u) = \begin{cases} -u^2(3u-3) & u \in [0,1) \\ -(2-u)^2(3u-3) & u \in [1,2] \\ 0 & \text{otherwise} \end{cases} \tag{6}$$

To calculate partial derivatives, the derivative of ϕ_L is also required. Each ϕ_L is composed of two polynomial functions, to obtain the derivative of ϕ_L each polynomial is differentiated as an independent function and results are combined.

$$\frac{d\phi_1(u)}{du} = \begin{cases} -6u(u-1) & u \in [0,1) \\ 6(u-1)(-2+u) & u \in [1,2] \\ 0 & \text{otherwise} \end{cases} \tag{7}$$

$$\frac{d\phi_2(u)}{du} = \begin{cases} -3u(3u-2) & u \in [0,1) \\ -3(3u-4)(-2+u) & u \in [1,2] \\ 0 & \text{otherwise} \end{cases} \tag{8}$$

The output of the competitive layer is

$$c = \underset{k \in \{1 \cdots K\}}{\arg\max}\left(y_k\right) \tag{9}$$

where y_k is the kth output and K is the total number of outputs.

Gradient descent method is used for training of the network parameters. The objective function to be minimized is

$$C_k = \frac{1}{2P}\sum_{s=1}^{P}\left(y_k(U_s) - f_k(U_s)\right)^2, \quad k = 1 \ldots K \tag{10}$$

where P is the number of training pairs, $y_k(U_s)$ is the kth output of the BPAMW classifier before the competitive layer and $f_k(U_s)$ is the kth desired output. The competitive layer is not included in the training, because it has a fixed function that does not need training and only operates when the classifier is in identification stage where it determines the final classification result.

Batch training mode is used where all training pairs $\{U_s, f_k(U_s)\}$, $s = 1, \ldots, P$ should be processed before parameters could be updated. Parameters are modified in the opposite direction of the gradient of C_k. To speed up the convergence rate, momentum term is included in parameter's update.

Let

$$\tau_{is} = \frac{z_{is} - t_i}{\lambda_i}, \tag{11}$$

$$\phi_L(\tau_{is}) = \phi_L\left(\frac{z_{is} - t_i}{\lambda_i}\right), \text{ and} \tag{12}$$

$$e_{sk} = y_k(U_s) - f_k(U_s). \tag{13}$$

Partial derivatives are expressed as follows:

$$\frac{\partial C}{\partial w_{iLk}} = \sum_{s=1}^{P} e_{sk} \phi_L(\tau_{is}) \quad (14)$$

$$\frac{\partial C}{\partial v_{ji}} = \sum_{s=1}^{P}\sum_{k=1}^{K}\sum_{L=1}^{r} e_{sk}\, w_{iLk} \frac{\partial \phi_L(\tau_{is})}{\partial \tau_{is}} u_{js} \lambda_i^{-1} \quad (15)$$

$$\frac{\partial C}{\partial t_i} = -\sum_{s=1}^{P}\sum_{k=1}^{K}\sum_{L=1}^{r} e_{sk}\, w_{iLk} \frac{\partial \phi_L(\tau_{is})}{\partial \tau_{is}} \lambda_i^{-1} \quad (16)$$

$$\frac{\partial C}{\partial \lambda_i} = \sum_{s=1}^{P}\sum_{k=1}^{K}\sum_{L=1}^{r} e_{sk}\, w_{iLk} \frac{\partial \phi_L(\tau_{is})}{\partial \tau_{is}} \tau_{is} \lambda_i^{-1} . \quad (17)$$

Parameters can be updated as follows:
h = iteration number

$$w_{iLk}^{h+1} = w_{iLk}^{h} - \eta \frac{\partial C}{\partial w_{iLk}} + \alpha \Delta w_{iLk}^{h} \quad (18)$$

$$v_{ji}^{h+1} = v_{ji}^{h} - \eta \frac{\partial C}{\partial v_{ji}} + \alpha \Delta v_{ji}^{h} \quad (19)$$

$$t_i^{h+1} = t_i^{h} - \eta \frac{\partial C}{\partial t_i} + \alpha \Delta t_i^{h} \quad (20)$$

$$\lambda_i^{h+1} = \lambda_i^{h} - \eta \frac{\partial C}{\partial \lambda_i} + \alpha \Delta \lambda_i^{h} . \quad (21)$$

where $\Delta x^h = x^h - x^{h-1}$.

Parameter initialization has a significant impact on the convergence rate of the BPAMW. A heuristic method for parameter initialization is proposed here. The following equations express the parameter initialization.

$$v_{ji} = rand() * 4 - 2 \quad (22)$$
for $j = \{1,\ldots, N\}$, $i = \{1,\ldots, M\}$

$$w_{iL} = 0 \quad (23)$$
for $i = \{1,\ldots,M\}$, $L = \{1,\ldots,r\}$

$$U_{\max} = \max_{s\in\{1,\cdots,P\}} (U_s) \quad (24)$$

$$U_{\min} = \min_{s\in\{1,\cdots,P\}} (U_s) \quad (25)$$

$$z_{i\max} = V_i^T \cdot U_{\max} \quad \text{(inner product)} \quad (26)$$

$$z_{i\min} = V_i^T \cdot U_{\min} \quad \text{(inner product)} \quad (27)$$

$$\lambda_i = \frac{z_{i\max} - z_{i\min}}{2} \quad (28)$$

$$t_i = \frac{z_{i\max} + z_{i\min}}{2} \quad (29)$$

where *rand*() is a function that generates random number in the range (0, 1).

The BPAMW classifier's training is needed to be done only once and after that, it can recognize new and unseen images of the persons in the training set. When operating in the identification mode, the classifier uses the stored parameters from training stage to calculate the outputs. The index of the output with the highest value is the class number of the input that is calculated by the competitive layer.

4. Experimental Results

AT&T "The Database of Faces" (formerly "The ORL Database of Faces") database contains 400 grayscale images of 40 persons. Each person has 10 images, each having a resolution of 92 x 112 and 256 gray levels. For some subjects, the images were taken at different times, varying the lighting, facial expressions (open / closed eyes, smiling / not smiling) and facial details (glasses / no glasses). All the images were taken against a dark homogeneous background with the subjects in an upright, frontal position (with tolerance for some side movement). The first three images from each individual of the database are selected for the test set and the rest of the face images are included in the training set. Therefore, a total of 280 face images are used for training and another 120 face images are used for testing. A sample of the face images are shown in **Fig. 3**.

Images were resized to size 6*7 and put in a one-dimensional vector, then pixel values were normalized to range (0,1) by dividing each element of the vector by the maximum value of the vector.

For the BPAMW classifier; number of multiwavelons was set to 40, the iteration number

was set to 5 and the learning rate was 0.01. The momentum term coefficient was 0.9. Results are summarized in **Table 1**. **Fig. 4** shows the training performance of the network. An average recognition rate of 97.75% was obtained over ten trials. Each trial involves training and testing. Since training uses the *rand()* function for parameter initialization, the final stored parameters upon convergence may differ slightly. This is why averaging the recognition rate over ten trials is performed to achieve stochastic ensemble averaging.

Table 1 Result of the BPAMW Classifier over ORL Database

Average Training MSE	Average Testing MSE	Average Recognition Rate
0.0034	0.0034	97.75

To compare the performance of the proposed BPAMW classifier with the BPW classifier, the same experiments were performed with the same parameters. Results are summarized in **Table 2**.

Fig. 5 shows the training performance of the network. An average independent recognition rate of 10.4% were obtained over ten trials.

Table 2 Result of the BPW Classifier over ORL Database

Average Training MSE	Average Testing MSE	Average Recognition Rate
0.2490	0.9846	10.4167

The proposed BPAMW classifier has a very good recognition rate of 97.75% in a very few iterations, which indicates that it has a very good recognition rate when there are variations in the facial expression and limited pose variations. Also the results show that BPAMW classifier is superior to BPW classifier because it achieved a higher recognition rate in the same number of iterations.

5. Conclusions

In this paper a classifier has been proposed for identification of human faces. The classifier is based on multiwavelet neural network. As an extension of wavelets, a multiwavelet can preserve all the advantages the wavelet has. Furthermore, it can simultaneously have several properties very useful in practical applications such as orthogonality, regularity, symmetry, and compact support, which is impossible for a scalar wavelet. Therefore, the network using the multiwavelet as activation functions has a better performance than the same network with wavelets as activation functions.

Experiments that were performed on AT&T "The Database of Faces" (formerly "The ORL Database of Faces") showed that BPAMW classifier has a very good recognition rate of 97.75% in the presence of facial expression, lighting and pose variations.

References

Bin Z., De-yuan H., and Tao L., "Research on the Application of Wavelet Neural Network in the Surrounding Rock Displacement Prediction," 2nd International Asia Conference on Informatics in Control, Automation and Robotics (CAR 2010), Wuhan, China, pp. 266-269, 6-7 March 2010.

Deniz O., Castrillfion M., and Hernfiandez M., "Face recognition using independent component analysis and support vector machines", Pattern Recognition letters, vol. 24, pp. 2153-2157, 2003.

Ensafi A.A., Khayamian T., and Tabaraki R., "Simultaneous Kinetic Determination of Thiocyanate and Sulfide Using Eigenvalue Ranking and Correlation Ranking in Principal Component-Wavelet Neural Network," Talanta, Vol. 71, Issue 5, pp. 2021-2028, March 2007.

Er M.J., Chen W., and Wu S., "High speed face recognition based on discrete cosine transform and RBF neural network", IEEE Trans. On Neural Network, vol. 16, no.3, pp. 679-691, 2005.

Er M.J., Wu S., Lu J., and Toh L.H., "face recognition with radial basis function (RBF) neural networks", IEEE Transactions on Neural Networks, vol. 13, no. 3, pp. 697-710, 2003.

Fan X., and Verma B., "A Comparative Experimental Analysis of Separate and Combined Facial Features for GA-ANN based Technique," Sixth International Conference on Computational

Intelligence and Multimedia Applications, pp. 279-284, Aug. 2005.

Huang L.L., and Shimizu A., "Combining Classifiers for Robust Face Detection," In Lecture Notes in Computer Science, 3972, Springer-Verlag, pp. 116-121, 2006.

Jiao L.C., Pan J., and Fang Y.W., "Multiwavelet neural networks and its approximation properties," IEEE Transactions on Neural Networks, Vol. 12, Issue 5, pp. 1060-1066, 2001.

Lee K., Chung Y., and Byun H., "SVM based face verification with feature set of small size", Electronic letters, vol. 38, no.15, pp. 787-789, 2002.

Li G., Zhang J., Wang Y., and Freeman W.J., "Face Recognition Using a Neural Network Simulating Olfactory Systems," In Lecture Notes in Computer Science, 3972, Springer-Verlag, pp. 93-97, 2006.

Liu L., and Liu Y., "MQPSO based on wavelet neural network for network anomaly detection," 5th International Conference on Wireless Communications, Networking and Mobile Computing (WiCom'09), Beijing, China, pp. 1-5, 24-26 Sep. 2009.

Long-yun X., Zhi-yuan R., and Rui-cheng F., "Gear Faults Diagnosis Based on Wavelet Neural Networks," Proceedings of IEEE International Conference on Mechatronics and Automation, Takamatsu, Japan, pp. 452-455, 5-8 Aug. 2008.

Lu K., He X., and Zhao J., "Semi-supervised Support Vector Learning for Face Recognition," In Lecture Notes in Computer Science, 3972, Springer-Verlag, pp. 104-109, 2006.

Lu X., Wang Y., and Jain A.K., "Combining Classifiers for Face Recognition," Proceedings of International Conference on Multimedia and Expo (ICME '03), Vol. 3, pp. 13-16, 2003.

Moghaddam B., "Principal manifolds and probabilistic subspaces for visual recognition", IEEE Transactions on pattern Anal. Machine Intelligence, vol. 24, no.6, pp. 780-788, 2002.

Othman H., and Aboulnasr T., "A separable low complexity 2D HMM with application to face recognition", IEEE Trans. Pattern. Anal. Machie Inell., vol. 25, no.10, pp. 1229-1238, 2003.

Pang S., Kim D., and Bang S.Y., "Face Membership Authentication Using SVM Classification Tree Generated by Membership-Based LLE Data Partition". In IEEE Transactions on Neural Networks, Vol. 16, Issue 2, pp. 436-446, 2005.

Park C., Ki M., Namkung J., and Paik J.K., "Multimodal Priority Verification of Face and Speech Using Momentum Back-Propagation Neural Network," In Lecture Notes in Computer Science, 3972, Springer-Verlag, pp. 140-149, 2006.

Plonka G., and Strela V., "Construction of Multi-Scaling Functions with Approximation and Symmetry," SIAM Journal on Mathematical Analysis, Vol. 29, Issue 2, pp. 481-510, March 1998.

Shen Y., Wang Q., and Yu S., "A Target Recognition of Wavelet Neural Network Based on Relative Moment Features," Proceedings of the 5th World Congress on Intelligent Control and Automation, Hangzhou, P.R. China, Vol. 5, pp. 4089–4091, 15-19 June 2004.

Turk M., and Pentland A., "Eigen faces for face recognition", Journal cognitive neuroscience, vol. 3, no.1, 1991.

Yang X., Kumehara H., and Zhang W., "Back Propagation Wavelet Neural Network Based Prediction of Drill Wear from Thrust Force and Cutting Torque Signals," Canadian Center of Science and Education (CCSE), Computer and Information Science Journal, Vol. 2, Issue 3, pp. 75-86, Aug. 2009.

Zhang B., Zhang H., and Ge S., "Face Recognition by Applying Wavelet Subband Representation and Kernel Associative Memory," In IEEE Transactions on Neural Networks, Vol. 15, pp. 166-177, 2004.

Zhao W., Chellappa R., and Krishnaswamy A,, "Discriminant analysis of principal component for face recognition", IEEE Transactions on Pattern Anal. Machine Intelligence, vol. 8, 1997.

Zhao W., Chellappa R., Phillips J., and Rosenfeld A., "Face recognition in still and video images: A literature survey", ACM Comput Surv vol. 35, pp. 399–458, 2003.

Zhao Y.Z., and Li X., "A Dual-Momentum Hybrid Wavelet Neural Net (DM-HWNN): Its Performance Evaluation and Application," 7th IEEE International Conference on Industrial Informatics (INDIN 2009), Cardiff, Wales, UK, pp. 325-330, 23-26 June 2009.

Zhou W., Pu X., and Zheng Z., "Parts-Based Holistic Face Recognition with RBF Neural Networks," In Lecture Notes in Computer Science, 3972, Springer-Verlag, pp. 110-115, 2006.

List of Symbols:

$C(\cdot)$	Objective Function to be Minimized in a Neural Network
$f(\cdot)$	Desired Output
J	Resolution Level of Multiscaling Function
K	Number of Output Nodes
L	Index of the Scaling Functions of a Multiscaling Function
M	Number of Wavelons or Multiwavelons
N	Number of Input Nodes (Input Dimension)
P	Number of Training Patterns
U	Input Vector
V	Input Weight Matrix
Z	The Set of All Integers
C	Output of the Competitive Layer
E	Difference Between Desired Output and Actual Output (Error)
H	Iteration Number (Epoch)
I	Index of the Wavelon or Multiwavelon
K	Index of Output Nodes
R	Multiplicity of Multiwavelet
s	Index of the Training Samples
T	Translation
U	Scalar Input
V	Weight Between the Input Layer and the Hidden Layer
W	Output Weight
Y	Output
z	Inner Product Between the Input Vector and the Input Weight Vector
Δ	Difference Operator
$\sum$	Summation Operator
$\Phi(\cdot)$	Multiscaling Function
$\Psi(\cdot)$	Multiwavelet Function
α	Momentum Coefficient
ε	Training Error Threshold
η	Learning Rate
λ	Dilation
τ	Input to the Wavelet or Scaling Function
$\phi(\cdot)$	Father Scaling Function
$\psi(\cdot)$	Mother Wavelet Function
$\psi'(\cdot)$	Derivative of Wavelet Function

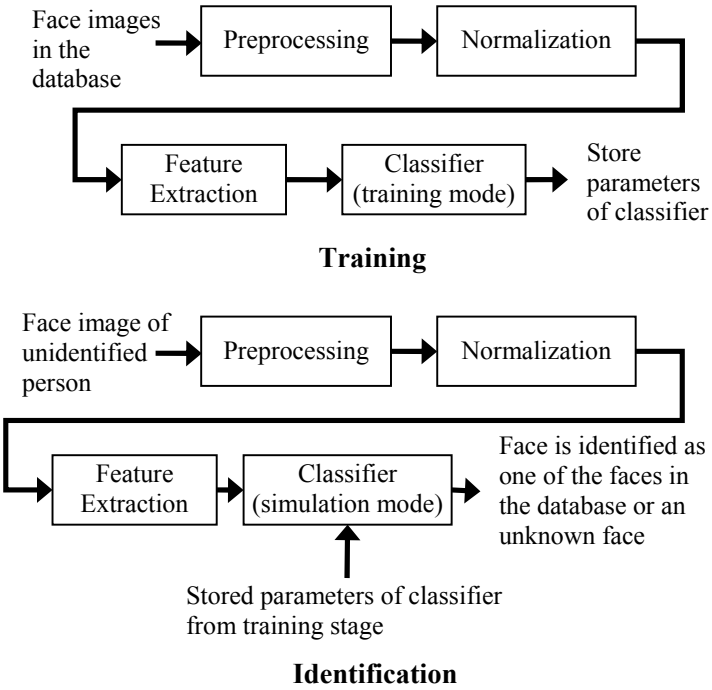

Fig. 1 The Proposed Face Identification System Block Diagram

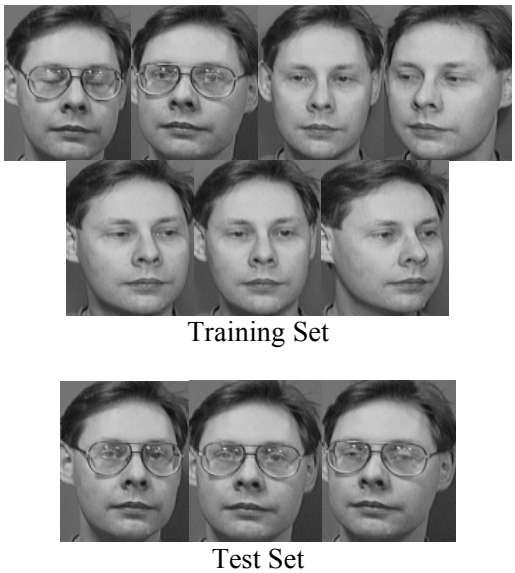

Fig. 3 Sample Images from the ORL Face Database

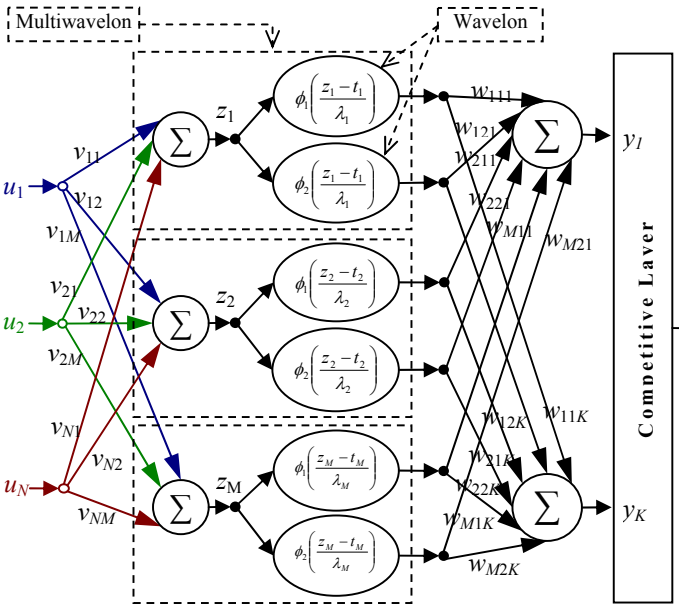

Fig. 2 The proposed BPAMW Classifier

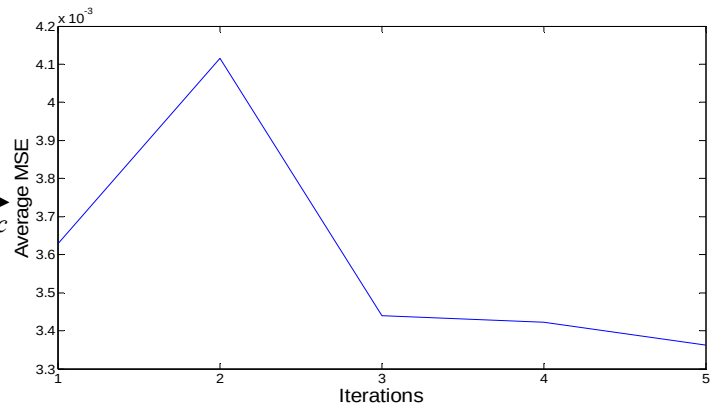

Fig. 4 BPAMW Classifier Performance over ORL Database: Average MSE vs. Iterations

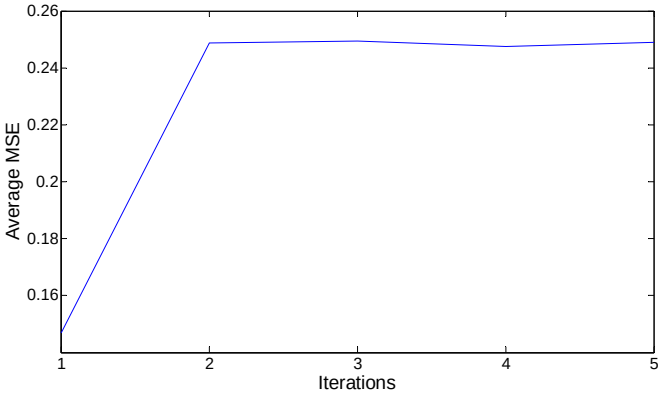

Fig. 5 BPW Classifier Performance over ORL Database: Average MSE vs. Iterations

Static Performance Characteristics Of Vortex Rate Sensor

Dr .Ali Abdul AL-Muhsen AL-Asady
Asst .Prof. Dept .of Mech .En
Baghdad University

Wisam Gasim Kadhum
Dept.of Mech .Eng.
Baghdad University

Abstract

The vortex rate sensor is a fluidic gyroscope with no moving parts and can be used in very difficult conditions like radiation, high temperature and noise with minimum cost of manufacturing and maintenance. A vortex rate sensor made of wood has been designed and manufactured to study theoretically and experimentally its static performance .A rig has been built to carry out the study, the test carried out with three different air flow rates (100, 150, and 200 l/min).The results show that the relation between the differential pressure taken from the sensor pickoff points and the angular velocity of the sensor was linear.The present work involved theoretical and experimental study of vortex rate sensor static characteristics .Vortex rate sensor has been designed and manufactured with dimensions-:

Radius of vortex chamber= 140 mm, Radius of sink tube r_s= 4.5 mm, the pickoff hole diameter = 2mm, Height of vortex chamber b= 19 mm, Height of pickoff pipe h= 25 mm.

Keywords :Vortex rate sensor, Angular vortex rate sensor, Rate gyro

الخلاصة:

متحسس معدل التدويم هو جايروسكوب مائعي بدون اجزاء متحركة ويمكن استخدامه بظروف صعبة جدا كالاشعاع ودرجات الحرارة العالية والضوضاء وبأقل كلفة تصنيع وصيانة. متحسس معدل التدويم مصنوع من ماده الخشب تم تصميمه وتصنيعه واستخدامه لوضع دراسة نظريه وعمليه للأداء الاستاتيكي للجهاز. كذلك تم بناء منظومة خاصة لإجراء الدراسة، في هذه الدراسة تم تسليط ثلاثة قيَم مختلفة لمعدل تدفق الهواء وهي (100,150 و 200 لتر\دقيقه) ووجد من خلال هذه الدراسة ان العلاقة ما بين فرق الضغط المأخوذ من الجهاز والسرعة الزاوية للجهاز هي علاقة خطيه.يتضمن هذا البحث دراسه نظريه وعمليه للخواص الاستاتيكيه للمتحسس . حيث تم تصميم وتصنيع المتحسس بالابعاد التاليه:

نصف قطر حجرة الدوامه(R)=140 ملم ، نصف قطر مجرى الخروج (r_s)=4,5 ملم،قطر فتحه الpickoff=2ملم، ارتفاع حجرة الدوامه (b)=19ملم، ارتفاع انبوب pickoff (h) =25 ملم.

[

Introduction

General introduction

The vortex rate sensor is a pure fluidic device with no moving parts that senses angular velocity about its axis and provides a differential pressure proportional to that velocity it can be used instead of a gyroscope .The three basic parts of the sensor are the coupling element, the vortex chamber, and the signal pickoff .The vortex rate sensor utilizes the tendency of the swirling flow to conserve the angular momentum imparted to it as a means of amplification to sense small rates of rotation . The existing vortex rate sensor consists of two coaxial disks separated by cylindrical coupling ring, which are often a porous material, with outlet sinks and two suitable pickoffs .The gaseous fluid flows through the coupling element of uniform length and porosity and discharges at the sink tube .The radial flow between the two coaxial disks is modified by the viscous shear and by the vertical flow created by the rotation of the unit about an axis parallel to its axis of symmetry .Thus, the confinement of the real flow and the subsequent modification of the velocity distribution in the sink tube cause appreciable reduction in the angular momentum imparted at the coupling . Attention is given to sensitivity, accuracy, and response time and to sensor design and fabrication with emphasis on housing and manifold, null adjust and built-in test and temperature compensation .A number of applications of the vortex rate sensor are considered :aircraft flight controls, ejection seat stabilization, and helicopter gun turret stabilization.

Various analyses have been carried out in the past with varying degrees of success and different specific objectives on vortex rate sensor.

[Organ H.D. 1965] changed the porous with cylindrical outer screen member and inner cylindrical screen member has a slightly smaller diameter than outer screen member . Positioned intermediate inner screen member and outer screen member are a plurality of glass balls having a small diameter approximately (0.15) It is clear that coupling means is porous in nature and allows fluid to pass through with a minimum of restriction.

[Barrete Doyle 1966] made vortex rate sensor with the same geometry but with another kind of pickoff, this kind includes optical means for providing an output signal indicative of the rotation of coupling relative to the structure .Optical means comprises a light source and two reflecting mirrors attached to intermediate light source and reflecting surface .A pair of photocells is attached to contiguous mirrors.

[Camarata F.J. 1969] Invented a twin vortex rate sensor .The invention contemn plates the provision of two counter-moving or rotating vortices, each having its axis or center line coincident with the axis about which movement of the body is to be sensed . The output flow or pressure of each vortex is compared with that of the other, and the differential of such output pressure or flows provides a signal indicative of the rate and direction in which a body containing such vortices is turning on the said axis .Thus, it will be seen that this applicant provides a device generally similar in function to a gyroscope, and it can be said that it is general object of this applicant to provide a device capable of sensing the rate and angular direction of movement of a body about a reference axis and capable also of producing a signal indicative of rate and direction so that the signal can be used in control of angular movement of the body.

[Hagiwara, etal.1973], studied the static characteristics of vortex rate sensor .A sensor probe is constructed of two stagnation pitot

tubes whose setting gap and angle are determined to be 3.6 mm and 67.5 deg . respectively for a sink tube with inner diameter of 8 mm by the preliminary experiments .In case of 100 *l*/min supply, output signal is 8.3 mm water per r.p.m and is linear up to 10 r.p.m for a sensor with the outer diameter of 280mm.Sensor efficiency is deduced theoretically and the results of the analysis are verified to coincide very well with the experimental results.

[Peter Norton 2006] invented a vortex angular rate sensor for measuring yaw rate or roll rate of an automotive vehicle comprises a freely rotating inertial disk and an angular rate sensor responsive to the rotation of the inertial disk relative to housing .In one embodiment the inertial disk presents an alternating magnetic field at its circumference .The rate and direction of rotation of the inertial disk relative to its housing is determined by three magnetic field sensor such as a linear Hall Effect sensor responsive to the field presented by the inertial disk .In another embodiment electronic cameras measure movement of fiducially marks on the inertial disk .Air surrounds the inertial and air viscosity gradually brings rotation to a stop .For yaw rate measurement the disk axis is oriented vertically and the inertial disk is supported in the radial direction by low friction bearing such as ball bearing or magnetic bearings and the axial direction by substantially frictionless bearing such as magnetic bearings .In certain embodiments two magnetic poles operate as both axial and radial bearings .For the purpose of sensing incipient or actual vehicle rollover, the axis of the inertial disk is oriented in the direction of the roll axis of the vehicle .The angle of recent rotation and rate of rotation of the inertial disk relative to the housing indicate the angle through which the vehicle has recently rotated about its roll axis and the roll rate of the vehicle .

Geometry Of The Sensor And Measuring Circuit

The sensor shown in the fig.1 made of wood type (NDF) for ease of machining.

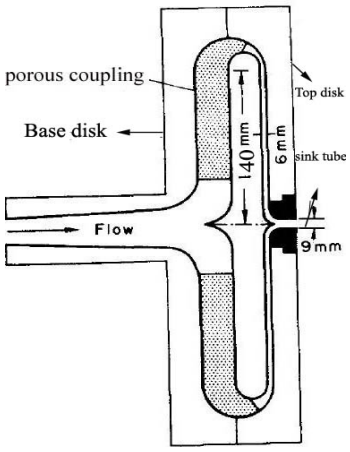

Fig.1 Schematic Drawing of vortex rate sensor

A series of slices and porous media made of sponge was inserted in the inlet region partly the purpose of the porous media and a slices were partially to ensure uniform flow at the periphery of the pancake.A single hole of 9mm diameter was drilled at the center line of the outer disk; a sink tube was fitted into this hole and tightened on the outer disk .The pickoff tube used at the exit of the sink tube called cylindrical pickoff tube as shown in **fig.2** placed across the sink tube.

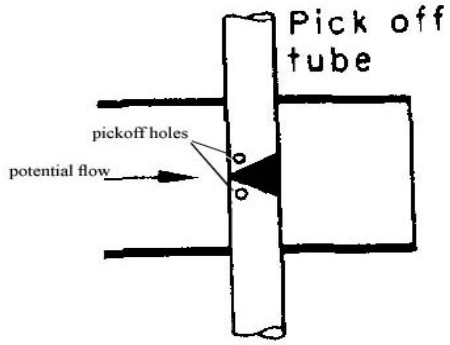

Fig.2 Schematic of Cylindrical Pickoff Element

[

The pickoff hole was positioned at 45 degree from the direction of flow in order to obtain maximum theoretical differential pressure across them .A straight forward analysis of potential flow about circular cylinder shows that whereas the rate of change of pressure with angular position is maximum at θ=45 degree .**Fig.3** shows the test rig, its consist of compressor to supply air, rotameter to measure the air flow rate and control it ,vortex rate sensor and pick off element, see **fig.4**, rate table for control and apply the angular velocity see **fig.5**, and U tube manometer to measure the output signal of vortex rate sensor

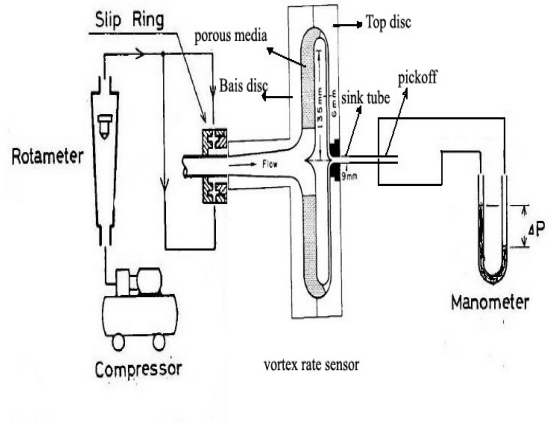

Fig.3 Testing Rig

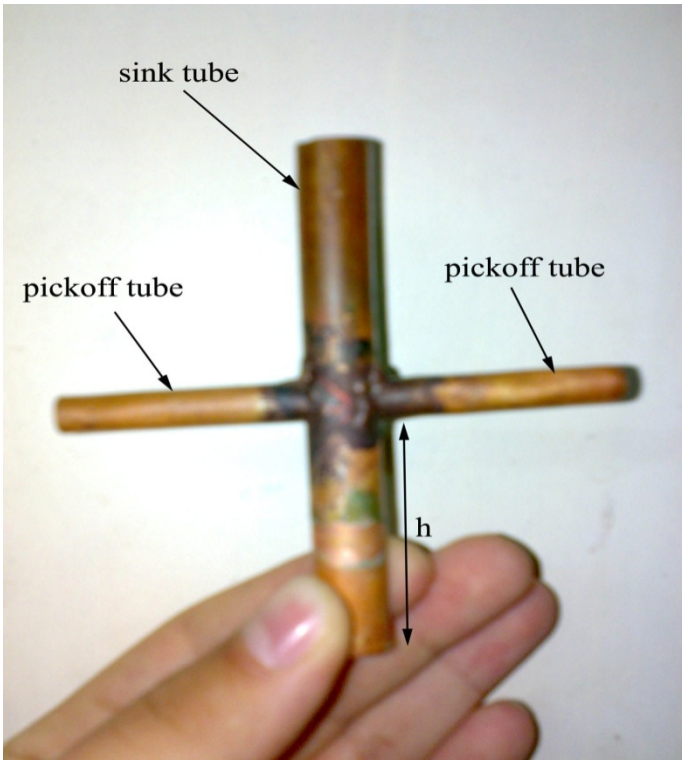

Fig.4 pickoff tube used in the test rig

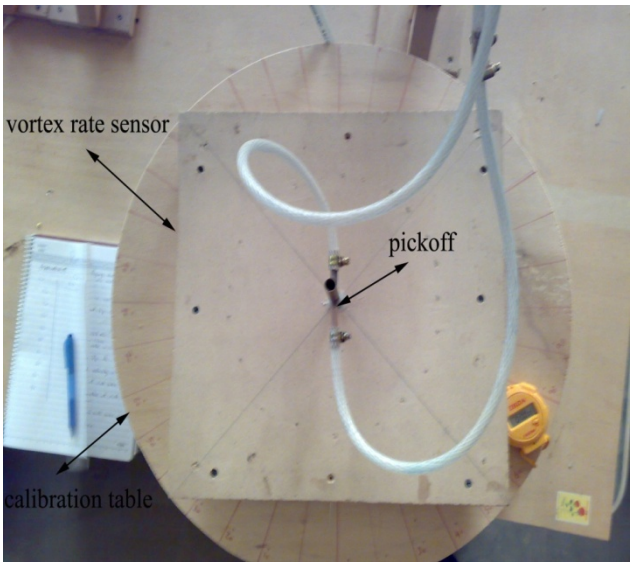

Fig.5 Calibration Table of vortex rate sensor

Analyses Of The Sensor Output

The principle work of pickoff element like the principle work of Pitot tube, because both of them determine the pressure at stagnation point(pickoff holes, pitot hole) which it's one of the application of Bernoulli's equation .It follow from Bernoulli's equation that the

pressure at stagnation point (total pressure P) is equal to the sum of the static pressure (P = 0) the dynamic pressure ($\frac{\rho U^2 \sin^2\theta}{2}$) of the flow .Apply the following assumption:

1. Neglect the viscosity (invisced) i.e $(\upsilon \nabla^2 V)$ .Is small, because the boundary layer is small compared with the chamber height.
2. The flow is incompressible (M< 0.3)
3. Neglect the body force (g=0).
4. Steady state.

The pickoff holes are set at angle **θ** against the sink tube axis and those holes are located at symmetrical distance – r_p and $+r_p$ from the center of sink tube respectively .If the vortex rate sensor is stationary and supply flow rate is constant, the detecting pressures of pickoff holes (P1 = P2).

$$P_1 = P_2 = 0.5\rho\beta^2 U^2 \sin^2\theta \qquad (1)$$

Eq. (1) represents the pressure distribution at pickoff hole when the vortex rate sensor is stationary .Where :

(β=1.12 for turbulent distribution flow) **[Pavila, C. 1972].**

As the vortex rate sensor rotates with angular rate ω_m, the jet from sink tube develops into spiral flow with the spiral angle Δθ .The differential pressure Δp between the pickoff holes (1) and (2) is produced.

$P_1 = 0.5\ \rho\ \beta^2\ U_s^2\ \sin^2\theta_1$ for pickoff hole (2)

$P_2 = 0.5\ \rho\ \beta^2\ U_s^2\ \sin^2\theta_2$ for pickoff hole (3)

$\Delta p = P_1 - P_2$ sub Eqs(2) and (3) that leads to:

$$\Delta p = 0.5\rho\beta^2 U_s^2 \Delta\theta \qquad (4)$$

Where $\Delta\theta \approx (\sin^2\theta_1 - \sin^2\theta_2)$

Noting that the swirling angle, resulting from the tangential velocity of fluid relative to the tangential velocity of pickoff hole; is given by **[Camarat, F. J 1996].**

$$\tan\Delta\theta = \frac{(U_{\theta rp} - r_p w)}{\beta U_s} \qquad (5)$$

$$\Delta\theta = \frac{U_{\theta rp}}{\beta U_s} \qquad (6)$$

Where $U_{\theta rp}$ is the maximum tangential velocity at radius $\mathbf{r_p}$ in sink tube, and that equal to:

$$U_{\theta rp} = \frac{E_2 \omega R^2}{r_p} \qquad (7)$$

r_p is The radial distance to the location of the pickoff hole which is also the radius where the tangential velocity is maximum.

$E_2 = \Gamma_p$,Γ_0= 0.716**[pavilan. C.1972].**

Sub eq (7) in (6) and then in eq (8) we obtain:

$$\Delta p = 0.5\rho\omega\beta E_2 U_s \left(\frac{R^2}{r_p}\right) \qquad (8)$$

The maximum tangential velocity occurs at a radial distance ranging from $0.3\,r_s$ to $0.4\,r_s$

Multiplying eq (8) by ($\frac{Q}{Q}$)

$\mathbf{r_s}$: the radius of sink tube .

Thus, writing :r_p=J .r_s

Where; J=const=0.376 **[peter Norton, 2006].**

Q=π. r^2_s. U_s then eq (8) is:

$$\Delta p = 0.34\left(\frac{\rho\omega Q}{r_s}\right)\left(\frac{R}{r_s}\right)^2 \qquad (9)$$

It is evident from eq (9) that the differential pressure signal increases most rapidly with degreasing sink tube radius, secondly with increasing sensor radius, and thirdly with increasing rate of rotation, flow rate and fluid density.

The standard deviation for the eq. (9) between the theoretical and experimental

[

results for (10) points curve at 100 l/min air flow rate is calculated as below;

$$\text{Standard deviation} = \frac{\sqrt{\frac{\sum(\delta(\Delta p))^2}{N-1}}}{\sqrt{N}} \qquad (10)$$

Where; N is the number of the corresponding points.

The standard deviation = 2.01108 mm water.

Obviously, there is a limit to the magnitude of each one of these parameters .The size of the pickoff element that in turn is limited by manufacturing difficulties, the flow rate is limited by the capacity of the available power source.

Test Procedure:

To collect and explain the relation between (Δp) and (ω) (static characteristics of vortex rate sensor) should follow the procedure bellow:

1) Turn on the compressor and start to press the air inside the container of compressor.
2) Open the valve of the rotameter and fix the float off on the flowmeter (50 L/min) firstly.
3) Before applying the angular velocity to the vortex rate sensor see that the signal in the differential manometer is zero.
4) Apply angular velocity started from (10, 20, 30, 40, 50, 60, 70, 80, 90) deg/sec respectively with no change in the value of the flow rate.
5) In each angular velocity has been applied on the vortex sensor, there is a signal produce as differential pressure measured in (mm water) on the differential manometer.
6) After that repeat the procedure again but with another flow rate (100, 150, 200) L/min respectively.

Results And Discussions:

The experiment that carried out for vortex rate sensor with this dimensions (Radius of vortex chamber (R)=140 mm , Radius of sink tub r_s = 4.5 mm, pickoff hole diameter =2mm , Height of vortex chamber (b)= 19mm, Height of pickoff pipe (h) =25 mm). Fig.6 shows the static characteristics theoretically for various flow rate and angular velocities .Note from Fig.6 that the linearity of vortex rate sensor keep in linear for ω=90 degree/sec and the Δp increases when increase the angular rate ω and when increase the flow rate of the input. Fig.7 shows the results of the vortex rate sensor experimentally for various flow rates and angular velocities .The range of linearity of signal obtained from cylindrical pickoff element was limited to approximately 70 deg/sec as shown in Fig.7 .This was in part due to the fact that the total velocity vector in the vicinity of the pickoff element was not in the plane normal to the cylinder, in the part due to the constricting effect of pickoff element which in turn altered the velocity profile and accelerated the flow, and in part due to the separation and vortex shedding behind the cylindrical coordinates .Fig.8 shows comparison between experimental and theoretical static characters and shows the relation between the differential pressure and angular velocity .It is, however; apparent from a cursory examination of the data presented here, the cylindrical pickoff yields a differential pressure output very good. So the output remains linear up to an angular velocity of approximately 70 deg/sec .This is partly due to the fact that the swirling flow has not been distributed by cylindrical pickoff and that the signal transition line has resulted in relatively more stream lined body there by significantly eliminating the flow separation , vortex shedding and noise.

There are many reasons that effect on the relation between the differential pressure and angular velocity:

1. Experimental errors (like stop watch, calibration table.)
2. The effect of viscosity on the swirl and flow in the sink tube.
3. The effect of the porous media and slices and several other secondary effects lead to reduce
   The efficiency.

The linearity of the vortex rate sensor to the differential pressure or between Δp and ω is also calculated from measuring the maximum input deviation and the maximum full scale input:

Non-linearity = ((max. input dev.)/(max. full scale input))*100 (11)

The non-linearity of the sensor is 5%, and form **fig.7** the curves make a line with a regression factor **0.9955** so we can say that the vortex rate sensor is linear to differential pressure Δp.

Resolution is the smallest measurement a sensor can reliably indicate .The resolution of the vortex rate sensor is 9 mm water differential pressure.

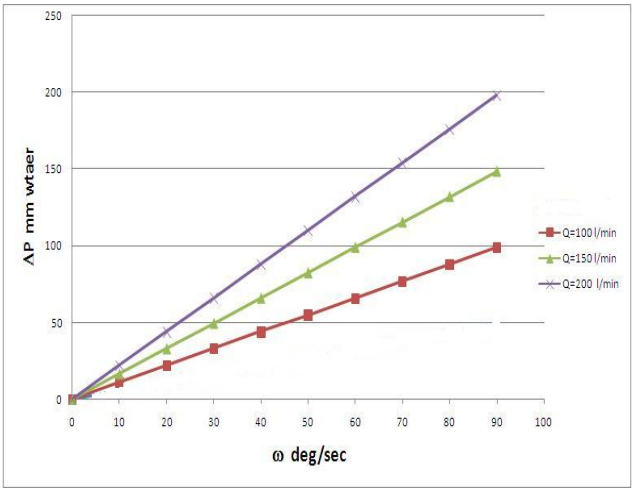

Figure.6 Theoretical static characteristics.

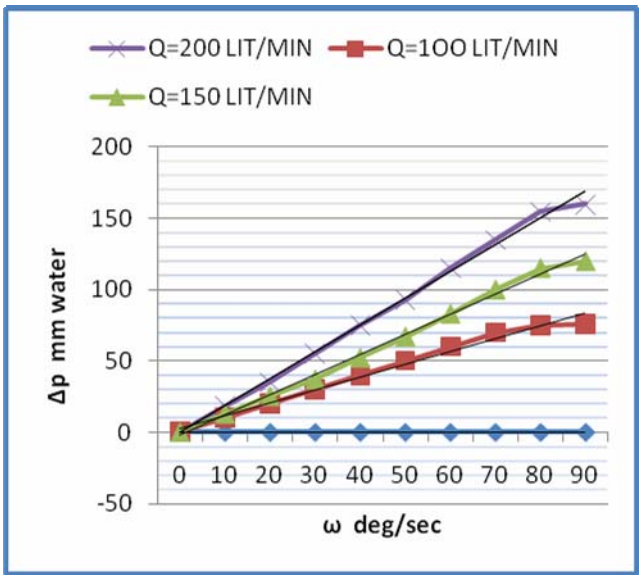

Figure.7 Experimental static characteristics.

Conclusions:

The static performance characteristics of vortex rate sensor are presented in fig (6, 7 and 8).from the figures it can be concluded that relation between the differential pressure and angular velocities is linear and the sensitivity of the instrument is increases as the flow rate increase.

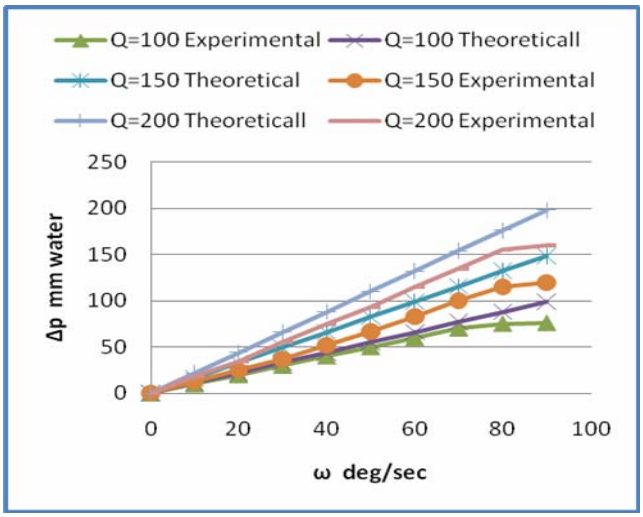

Figure.8 Comparison between theoretical and experimental static characteristics.

[

Refrenceses

Barrett Doyle, “Vortex Rate Sensor", U.S Patent 3,240,060 (Mar 1966).

Camarata, F.J.”Twin vortex angular rate sensor”, U.S patent 3,447,383 (June 1996)

Foster. K .&Parker, G.A,"Fluidics Components and Circuits", McGraw-Hill Company, 1970

Ogren .H .D, “vortex rate sensor” ,U.S patent 3,203,237 (Aug 1965).
Aeronautics and Space A demonstration, Washington, D.C, July 1969.

Paviln..,”Theoretical Analysis of Angular Momentum Conservation and Signal Transition in a Constant Speed Rate Sensor", Journal of fluid mechanics, Vol.8, pp 433-443, pergamon presses 1972.

Peter Norton, "Angular Rate Sensor ", U.S Patent 7,132,936 B1, (Nov 2006).

Sarpkaya. T, "A Theoretical and Experimental Study of Vortex Rate Gyro", advance in fluidics, ASME, 1967.

.Sarpkaya.T,"A Pneumatic Vortex-Angular Rate Sensor-Analysis and Experiments", second IFAC symposium on fluidics, Vol.9, pp.29-34, pergamon press, 1973.

Tatsaya, Chiaki Iwadare,”On a vortex angle ratesensor” J.S.M.E, vol.12, No.7, 1973

Wilton P .Lock and Sbu W.Gee, "Flight Investigation of A Fluidic Auto Pilot System", National
Tatsuya Hagiwara, Shoji Kamimura and Chiaki Iwadare. "On A Vortex Angular Rate Sensor", J.S.M.E, Vol.12, No.7, 1973.

Nomenclature

SYMBOL	MEANING
E_2	viscous efficient within sink tube
G	Acceleration due to gravity (m/ s^3)
M	mach number
P	Pressure distribution for potential flow across cylinder (mm water)
R	The effective radius of vortex rate sensor (mm)
r_p	The radial distance to the location of the pickoff hole (mm)
U_s	the average velocity in sink tube (mm)
$U_{\theta rp}$	Maximum swirl velocity in sink tube (mm/s)
B	coefficient depending on a velocity distribution in the sink tube
Γ	Kinematics viscosity (m^3 / s)
Θ	The swirl angel (degree)
P	The density of fluid (kg / m^3)
Ω	The angular viscosity (rad/s)
Γ_0	Circulation retained by the flow prior to the entrance into sink tube (m^2 / s)
Γ_p	Core circulation (m^2 / s)

Effect of Cryogenic Treatment on the Properties of Low Carbon A858 Steel

Dr. Abbas A. Hussein **Murtadha Qasim Idan AL-kinani**
Univ. of Baghdad/ Mech. Eng. Dept., Baghdad-Iraq

Abstract

This study is concerned with the effect of Deep Cryogenic Treatment (DCT) at liquid nitrogen temperature (-196 ^{o}C) on the mechanical properties and performance of low carbon steel (A858).
The tests specimens were divided in to two groups, the first group was subjected to the conventional heat treatment of normalizing, and the second group was also normalized then subjected to (DCT).
The results have shown that after (DCT), the Hardness, Tensile properties and the impact energy absorbed were all slightly increased. However the fatigue test showed some positive improvement in fatigue limit by 20(N/mm^2), and the volume wear rates at different loads were significantly decreased after (DCT).
The changes in microstructure due to (DCT) were clearly noticeable, the grain boundaries were no longer visible, and the Pearlite isles globalization was obvious.

Key Word: DCT, wear, fatigue limit; microstructure

تأثير المعاملة الزمهريرية العميقة على خواص فولاذ منخفض الكربون

الخلاصة

هذه الدراسة تتركز على تأثير المعاملة الزمهريرية العميقة عند درجة حرارة النتروجين المسال والبالغة (-196°C) على الخواص الميكانيكية وخـواص الأداء للفولاذ منخفض الكربون A858 .

عينات الاختبار قسمت إلى مجموعتين استنادا إلى ما قبل وما بعد المعاملة الزمهريرية ، المجموعة الأولى تضمنت المعاملة الحرارية التقليدية للفولاذ وهـي التطبيع، والمجموعة الثانية تضمنت المعاملة الزمهريرية ما بعد معاملة التطبيع.تم مقارنته نتائج الخواص الميكانيكية الناتجة بالمعاملة الزمهريرية العميقة مع تلك التي لم تتم معاملتها بهذه الطريقة. أن الاختبارات الميكانيكية تضمنت اختبارات الصلادة، الشد والصدمة بينما اختبارات الأداء تمثلت باختبارات الكلال والبلى.

اظهرت نتائج الاختبارات بعد أجراء المعاملة الزمهريرية العميقة ، زيادة قليلة في قيم الصلادة وخواص الشد (جهد الخضوع، المقاومـة القـصوى ، الاستطالة النسبية) وطاقة الصدم.

أختبار الكلال أظهر تحسينات ايجابية في قيم حد الكلال ما بعد المعاملة الزمهريرية ، حيث انها ازدادت بمقدار20 ن/ملم2. وبالنسبة لمعـدل البلـى ألحجمي عند أحمال مختلفة فقد أنخفض بعد المعاملة الزمهريرية بنسبة كبيرة ، مما يعني ان المعاملة الزمهريرية العميقة تحسن مقاومة البلي للفولاذ منخفض الكربون.

التغيرات في البنية المجهرية نتيجة المعاملة الزمهريرية كانت واضحة لهذا الفولاذ، حيث ان الحدود البلورية لم تظهر وحدث تكتل للبيرلايـت بـشكل واضح .

1. Introduction

Cryogenic treatment is a supplementary heat treatment that is performed on some finished steel component as an effective method to improve their performance. Two types of cryogenic treatments are generally applied, the shallow cryogenic treatment which is performed between (-60 ^{o}C) and (-90 ^{o}C), and the deep cryogenic treatment that is conducted at temperatures below (-196 ^{o}C).

Meng et al [1994] studied the wear resistance and microstructure of Fe–12Cr–Mo–V-1.4C tool steel both with and without cryogenic treatment. The study reveals that cryogenically treated samples show improvement from 110% to 600% through sliding wear test. From the microstructure of the steel it is reported that the improvement in wear resistance after cryogenic treatment can be attributed to eta-carbides precipitates.

Mohan Lal et al. [2001] studied the improvement in wear resistance and the significance of treatment parameters in AISI T1, M2, and D3 tool steel. It was found that cryogenic treatment imparts nearly 110% improvement in tool life. The un-tempered samples when cryogenically treated, yield 3%, 10%, and 10.6% extra life over tempered and cryogenically treated samples, respectively. Tempered samples when cryogenically treated at 133K for 24 hrs yielded negative results, but when cryogenically treated at 93K for 24 hrs, the results were favorable. The prescribed cycle yields 20% extra life as compared to the maximum life achieved through cold treatment.

Johan Singh et al. [2003] investigated the effect of cryogenic treatment on the axial fatigue performance of fillet welded cruciform joints of AISI 304L stainless steel, which failed in the weld metal. It has been observed that after the deep cryogenic treatment at 88 K, the fatigue life improved almost by a factor of two. During the treatment, significant microstructural changes that occurred accounted for the improved fatigue performance. Strain induced martensitic transformation was observed. During this transformation, the weld metal tends to expanded inducing compressive residual stresses in the weld metal.

Bensely et al. [2006] studied the effect of cryogenic treatment on the wear resistance of case carburized steel-En 353. Pin on disk wear test was carried out for three different load conditions and seven sliding speeds for the samples, which have undergone three different treatment conditions, conventional heat treatment (CHT), shallow cryogenic treatment (SCT), and deep cryogenic treatment (DCT). It was found that the wear resistance had been considerably increased due to SCT and DCT when compared to CHT. The study concluded that for better wear resistance, it is advisable to go for deep cryogenic treatment.

Hao-huai Liu et al. [2007] investigated the effects of (DCT) on the microstructure, hardening and abrasion resistance of 3Cr13Mo1V1.5 high chromium cast iron. The results showed that deep cryogenically treated specimens after sub-critical treatment had an increase in hardness and abrasion resistance. This was due to abundant retained austenite transforming into martensite and secondary carbides precipitation.

Franjo Cajner et al [2009] discussed the effect of deep-cryogenic treatment on impact fracture toughness, erosion wear resistance, and the microstructure of PM S390 MC high speed steel. A set of test samples was heat treated by conventional methods (hardened and three times high temperature tempered), and the other set were deep cryogenic treated. They concluded that the application of deep-cryogenic treatment results in significantly higher wear resistance, but no significant improvements in toughness have been observed.

G.Z. Ma, D. Chen et al [2010], studied a martensitic phase transformation from the B2 to the B19'CuZr phase in the Cu-Zr-Al bulk metallic glass (BMG) composite was induced by cryogenic treatment. The martensitic transformation causes the improvements of the microhardness and the ultimate compression fracture strength. When the cryogenic treatment time was 72 h, the microhardness and the ultimate compression fracture strength of the BMG composite increased about 18.55% and 37.5%, respectively.

The present work is aimed to study the effect of deep cryogenic treatment (DCT)

on the mechanical properties and performance of low carbon steel A858. In addition a comparison study of the obtained results from mechanical and microstructure tests with specimen's conventionally heat treatment (CHT).

Table (1): Chemical composition of A858 steel.

Element%	C	Si	Mn	Fe
Composition	0.13	0.25	0.45	Bal.

2. Expermential

2.1. Sample preparation

Commercially available 30mm diameter bar stock of A858 raw material was procured. In order to confirm the composition of the material, a chemical analysis of the steels was carried out by (Thermo ARL3460, optical Emission spectrometer), the results of which are shown in Table (1).

2.2 Heat treatment

All the specimens for fatigue, wear, tensile and impact tests were normalized; it was heated to a temperature of (900 °C) for a period of 20 minutes and then air cooled.

2.3 Deep Cryogenic Treatment (DCT).

To compare the effect of the cryogenic treatment on the mechanical properties and the performance of the A858 steel, the present work involves Deep Cryogenic Treatment by soaking the steel specimens at very low temperatures (-196 ^{o}C), using liquid nitrogen as the cooling medium. To avoid thermal shock due to quick quenching, the specimens were protected by a 10 mm all around shield of paraffin wax. It took 20 minutes for the specimens to reach the (-196 ^{o}C) from ambient temperature or approximately a cooling rate of 11 °C/min. Once the soak temperature (-196 ^{o}C) is reached the components are held at that temperature for a period of 24 hours .The cryogenic treatment of the samples were done in a cryogenic chamber which is fully covered with multilayer super insulation and is filled with liquid nitrogen which is used as the cooling medium.

After cryogenic treatment, a stress relieving process was applied by heating the specimens to (200 ^{o}C) for one hour and cooled in air to room temperature.

2.4 Mechanical Tests

2.4.1 Hardness Test

Brinell hardness test (HRB) was used and the Vickers hardness number (VHN) of the samples was also calculated from tables.

2.4.2 Tensile Test

The tensile test was carried out according to American Society for testing Material (ASTM) A370-05.A rod tensile specimen of geometry and dimensions shown in Figure (1).

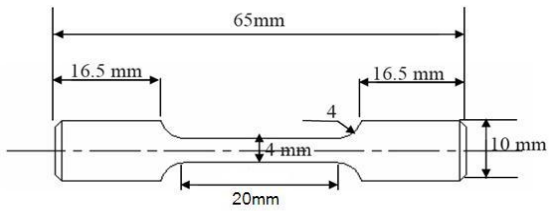

Fig. (1): Tensile Specimen.

2.4.3 Impact Test

An Izod impact test was carried out according to American Society for testing Material ASTM (E23) Izod cantilever beam type Y. Three specimens for each group were used to perform the Impact test. The average value of three tests was recorded. Figure (2) shows the impact test specimen.

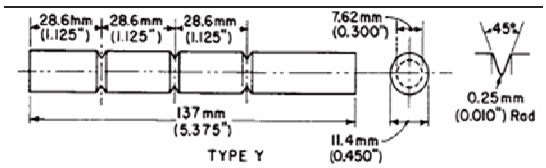

Fig.(2): Izod Impact Specimen.

2.5 Performance Test

2.5.1 Fatigue Test

A rotating bending fatigue machine was used to carry out the fatigue testing . A maximum capacity of (+800 N/mm^2) and a speed of (6000 rpm) were available with a capability of applying different stress levels with zero mean stress(stress ratio equal to (-1).Al the tests were performed at room temperature. The specimens are subjected to an applied load from the right side perpendicular to the axis of specimen and hence a bending moment is developed. The shape and dimensions of fatigue specimens used in the experimental work are as shown in figure (3). During manufacturing of the specimens, careful control was taken to produce a good surface finish and to minimize residual stresses. The outer surface at the reduced section of all fatigue specimens was polished to eliminate the effect of surface roughness caused by machining, hence all specimens obtained similar surface finish by using different grades of emery papers (400,600,800, 1200m1800 and 2000) .

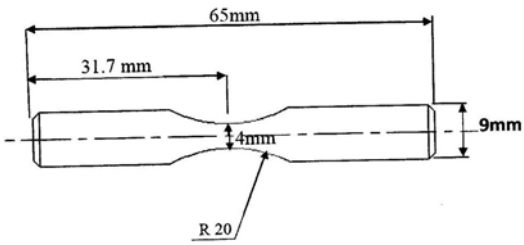

Fig.(3): Fatigue test Specimen.

2.5.2 Wear Test

Dry sliding wear tests were carried out on a pin on disc wear testing machine. The rotating friction disc was made of tool steel (surface hardness ≈385 VHN) , The wear tests were carried using three different normal loads :15 N, 25N and 40N at a constant linear sliding velocity of 2 ms−1, in dry condition at a room temperature of ~25°C and the time used was 10 min for each run. The specimens were prepared according to ASTM (G99-05) standard, where 10mm diameter and 30mm length were used as static pins. The faces of the pin specimens were polished by emery papers and cleaned prior to wear test. The weight method was used to calculate the wear resistance, where the specimens was weighted before and after applied load, the volume losses is given by relation:

$$WRv = \frac{\Delta w}{2\pi r n t \rho} \quad \text{.....} \quad (1)$$

Where:
WRv= volume wear rate in cm^3/cm
Δw =weight before applied load - weight after applied load.
ρ= Steel density =7.085 gm/cm^3
r= Effective disc radius=70 mm.
n= Friction disc rotational speed (277.4 rpm).
t= Time of applied load (10 min).

2.6 Micostructure Test

Samples for microstructure examination were ground using different grades of wet emery papers (220, 400, 800 and 1000), then polished using two grades of diamond paste (1um and 0.3 um). Distilled water and alcohol were used to clean the samples in succession. Etching was carried out using Nital etching solution (2% HNO3 in alcohol), followed by washing them with water and soup to remove stains, then rinsed with alcohol and dried. The microstructure examination is performed with an optical microscope which has a photo digital system and computerized by special imaging software. The images were photographed with a magnification of (800X).

3. Results

3.1 Hardness Test resilts

Table (2) shows the results of Rockwell Hardness tests (and its conversion to Vickers hardness) of the steel. The improvements caused by the DCT were calculated. It can be noticed that the

hardness increases after cryogenic treatment for this steels is only 2.66%.

Table (2): Results of Hardness test
(The results are averages of five tests).

Treatment	Impact energy (Kgf.m)	Improve %
Normalized	80.8333	
Normalized +DCT+T	82.8333	2.47%

3.2 Tensile test results

The tensile test results are presented in table (4) and figure (3). After DCT, the improvement in ultimate tensile strength (UTS), yield strength (σy) and elongation (є %) are only moderate.

Table (3): The results of Impact test.
(Each is an average of three tests).

Heat treatment	HRB	VHN	change %
Normalized	90.2	184	
Normalized+ DCT+T	92.6	201	2.66

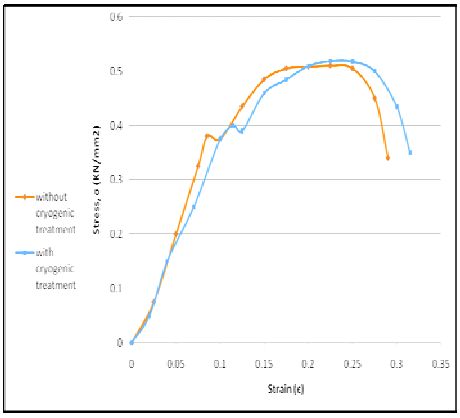

Fig.4: Tensile test profiles before and after DCT.

3.3 Impact test results

The impact test results are shown in table (5). The results show an increase in impact energy for this steel after DCT. The percent improvement is 2.47%. This improvement in this case can be attributed to the densification of the metal atoms and removal of residual stress.

Table (4): The results of tensile test.

treatment	UTS KN/mm^2	σy KN/mm^2	є%
Normalized	0.49	0.365	29.5
Normalized +CD+T	0.514	0.385	32

3.4 Fatigue test results

The fatigue test results for the normalized steel before and after DCT are presented in the forms of (S-N) curves as shown figure (5).Seven specimens were used to construct each curve.

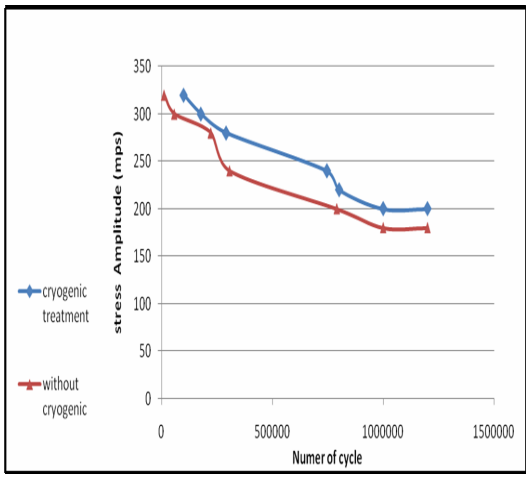

Fig. 5: S-N Curves before and after DCT.

3.5 Wear test results

The wear rates (WR) have been calculated as volume wear loss (cm^3) per unit sliding distance (cm) corresponding to the steady-state wear regime. The relation between the load and volume wear rate are shown in figures (6) and (7).They indicates a clear and significant improvement in wear resistance after DCT at all loads.

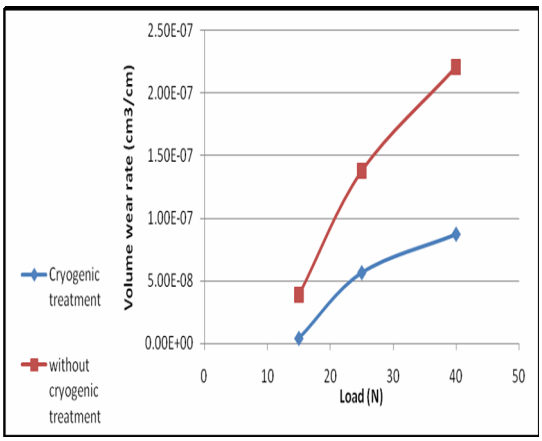

Fig. (6): The relation between the load and Volume wear rate.

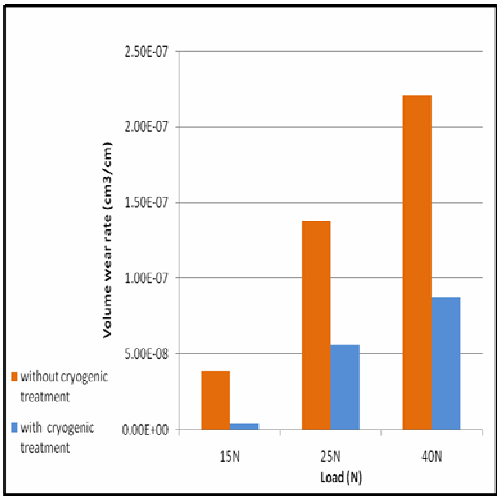

Fig. (7): Histogram showing the effect of DCT on wear rate.

5. Microstructure Tests

Figure (8) shows the microstructure of the normalized steel, and figure (9) shows the microstructure of the normalized steel after DCT, It can be observed that the microstructure contains usual phases which are present in this type of steel i.e. Ferrite (α-iron) and Pearlite (Fe3C+α-iron).However there are clear difference between them in which after DCT, the morphology of both phases are completely different, in which no grain boundaries can be seen and the Pearlite became globules.

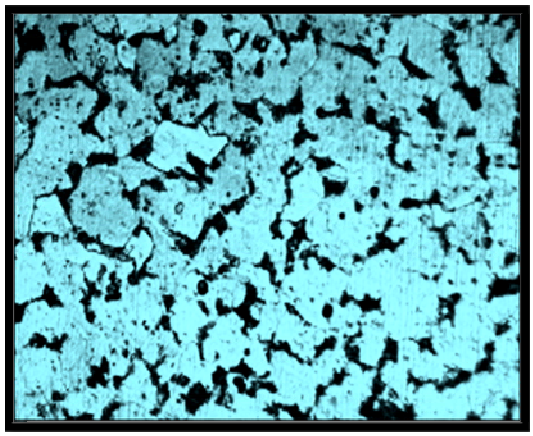

Fig.(8):Microstructure of normalized Steel before DCT, showing normal ferrite and pearlite(Dark) at grain boundaries.

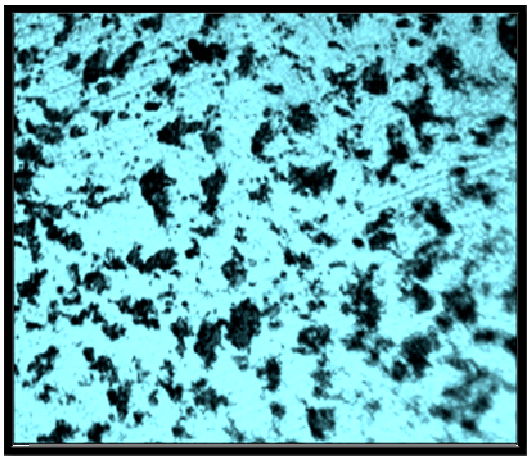

Fig.(9):Microstructure of normalized Steel after DCT. Showing (globalization) of Pearlite and no grain boundaries are visible.

6. Discussion

The main general aim of DCT is to improve the performance of the component, the result of all inspection showed significant improved performance in respect to fatigue and wear resistance .These are the most important aspects of

the mechanical parts, which are subjected to dynamic loading. The tested steel showed noticeable increase in fatigue limit, hence it can be concluded that DCT does improve the fatigue life of low carbon steel.

As for wear resistance improvement, the result was positive, and best performance was found at lower load (15N), this is a low carbon steel containing only (0.13%C) in normalize condition contains ferrite and Pearlite which is regarded a stable structure, yet it showed high response to DCT in which a major structure change occurred as shown in figure (9), although the increase in hardness was only 2%, which means that the improvement in wear resistance could be attribute to structure changes such as the (globalization) of Pearlite.

Figure (8) shows atypical structure of normalize low carbon steel, the grain and the grain boundaries are clearly shown and the Pearlite isles are distributed around the grains, generally on grain boundaries. But figure (9) in which the specimens was subject to DCT, the structure is completely different, in which the grain boundaries are no longer visible and the Pearlite isles are seem to be (globalized).

The disaperance of the grain boundary may attributed to the removal of the grain boundaries defects such as vacancies, and to the rearrangement of the grain boundary atoms, this could make the grain boundaries less vulnerable to etching solution.

As for the globalization of the Pearlite isles, a possible explanation is that due to sever contraction during DCT, the Pearlite which consist layers of hard Cementite and soft Ferrite will be squeezed by the contraction of the Ferrite matrix. However after warming up, the homogenous ferrite matrix will return back to its original shape, but the Fe3C lamella may have (cracked) hence the Pearlite can no longer regain its original shape. This may explain the (globalization) shape of the Pearlite. For this type of structure, no mention was found in the literatures.

6- Conclusions

From the results of the present investigation on the effect of cryogenic treatment on properties and structure of A858 steel, the following conclusions were drawn:

1-The hardness, ultimate tensile stress, yield stress, percentage elongation (ϵ) and impact energy for A858 steel were all moderately increased after DCT.

2- The fatigue limit of the steel increased by 20 KN after DCT.

3-The volume wear rate decreased significantly or wears resistance increased after DCT and best wear resistance was at (15N) load.

5- The grain boundaries after DCT were no longer visible, and the Pearlite isles were globalized.

Refrences:

Bensely, A. Prabhakaran, A. Mohan Lal and D. Nagarajan ,"Enhancing the wear resistance of case carburized steel En 353 by cryogenic treatment", *Cryogenics 45 pp:747-754* , (2006).

Franjo Cajner, Vojteh Leskovšek, Darko Landek, and Hrvoje Cajner, "Effect of Deep-Cryogenic Treatment on High Speed Steel Properties", *Materials and Manufacturing Processes, 24*, pp: 743–746, (2009).

G.Z. Ma, D. Chen, Y. Jiang and W. Li, "Cryogenic treatment-induced martensitic transformation in Cu-Zr-Al bulk metallic glass composite ", *Intermetallics 18*, pp: 1254-1257, (2010).

Johan Singh, P. Guha, B. Achar, D.R.G.," Fatigue life improvement of AISI 304L cruciform welded joints by cryogenic treatment", *Engineering Failure Analysis* 10, pp:1-10 (2003).

Liu, H. Wang, J. Shen, B. Yang, H. Gao and S. Huang, S.,"Effects of deep cryogenic treatment on property of 3Cr13Mo1V1.5 high chromium cast iron", *Materials and Design* 28, pp: 1059–1064, (2007).

Meng F. and Tagashira K., "Wear resistance and microstructure of cryogenic treated Fe–1.4Cr–1C bearing steel", *Hideaki Sohma, ISIJ Int.*, (1994).

Mohan Lal, D.Renganarayanan, S. Kalanidhi, A. "Cryogenic treatment to augment wear resistance of tool and die steels", *Cryogenics 41*, pp: 149-155 (2001).

Water Flow Visualization And Velocity Measurement Using Hydrogen Bubble Generation Technique In Low Speed Open Channel

Asst. Prof. Dr. Akram W. Ezzat **Taif M. Mansoor**
Univ. of Baghdad / Mech. Eng. Dept., Baghdad-Iraq

Abstract

Visualization of water flow around different bluff bodies at different Reynolds number ranging (1505 - 2492) was realized by designing and building a test rig which contains an open channel capable to ensure water velocity range (4-8cm/s) in this channel. Hydrogen bubbles generated from the ionized water using DC power supply are visualized by a light source and photographed by a digital camera. Flow pattern around a circular disk of (3.6cm) diameter and (3mm) thickness, a sphere of (3.8cm) diameter and a cylinder of (3.2cm) diameter and (10cm) length are studied qualitatively. Parameters of the vortex ring generated in the wake region of the disk and the separation angle of water stream lines from the surface of the sphere are plotted versus Reynolds number. Proper empirical formulas are investigated to describe the behavior of vortex ring parameters and separation angle versus Reynolds number. Vortex growth history in the wake region of the cylinder is identified by analyzing the photographs extracted from the digital camera used for photography purposes. Water velocity measurement in the upstream region and near the edge of the disk is conducted at different Reynolds number by measuring the length of Hydrogen bubble pulse streaks generated in the upstream region of the disk using electronic pulse generator circuit. Special electronic circuit is designed and fabricated to cut off the applied DC voltage. The calibration of the designed pulse generator is conducted using the proper oscilloscope device. The pictures extracted from the digital camera are used for analyzing the generated Hydrogen pulses.

Keyword: flow visualization, hydrogen bubble visualization method.

مشاهدة وقياس سرع جريان الماء باستخدام تقنية توليد فقاعات الهيدروجين في قناة مفتوحة ذات سرع واطئة

الخلاصة

تم مشاهدة جريان الماء حول اجسام مختلفة لقيم رينولدز تتراوح (١٥٠٥-٢٤٩٢) من خلال تصميم و تصنيع منظومة تحتوي على قناة مفتوحة تضمن سرع ماء تتراوح (٤-٨سم/ثانية) في هذه القناة. تمت مشاهدة فقاعات الهيدروجين المتولدة من الماء المؤين بواسطة مجهز قدرة للتيار المستمر من خلال اضائتها بمصدر ضوئي وتصويرها عن طريق كاميرا رقمية . تمت الدراسة النوعية لنمط الجريان حول قرص دائري بقطر (٣،٦سم) سمك (٣ملم) و كرة بقطر (٣،٨سم) و اسطوانة بقطر(٣،٢سم)وبطول (١٠سم).

تم رسم علاقة لمحددات حلقة الدوامة المتولدة في المنطقة الخلفية للقرص و زاوية انفصال خطوط جريان الماء من سطح الكرة مع رقم رينولدز. تم ايجاد معادلات تجريبية لتوضيح تصرف هذه المحددات و زاوية الانفصال مع رقم رينولدز. تم تعريف التسلسل الزمني لنمو الدوامة في المنطقة الخلفية للاسطوانة من خلال تحليل الصور من الكاميرا الرقمية المستخدمة لاغراض التصوير. تم اجراء قياس سرعة الماء في المنطقة الامامية و المنطقة القريبة من حافة القرص الدائري عند قيم رينولدز مختلفة من خلال قياس طول شرائح فقاعات الهيدروجين المتولدة بشكل نبضي باستخدام دائرة توليد النبضات الالكتروني. تم تصميم و تصنيع دائرة توليد النبضات الالكترونية لغرض تقطيع الفولتية المجهزة و معايرة هذه الدائرة باستخدام جهاز (اوسكلسكوب) . تم استخدام الصور المستخلصة من الكاميرا الرقمية لغرض تحليل نبضات الهيدروجين المتولدة.

Introduction

Flow visualization is an experimental tool for understanding flow pattern and measuring low fluid velocities. Flow visualization methods could be classified into three groups, addition of foreign material, optical methods and addition of heat and energy. Hydrogen bubble generation technique classified within addition of foreign material group. Hydrogen bubble technique is based on the electrolysis of water. When two electrodes are inserted in the water and a voltage applied between them, hydrogen bubbles are formed at the cathode and oxygen bubbles are formed at the anode. Normally the cathode is a very thin wire of diameter 0.05 mm or less. These wires produce very small hydrogen bubbles in size and the buoyancy forces become negligible compared to hydrodynamic drag forces causing little disturbance of actual flow conditions. A first description of the hydrogen-bubble technique has been given by Clutter and Smith (1961). Shraub et al. (1965) used the Hydrogen bubble technique for quantitative determination of time dependent velocity fields in low speed water flow. Davis and Fox (1967) revised the hydrogen bubble technique and applied it to the measurement of velocity profiles of water flowing in a circular clear plastic tube of the (35 ft x 1 in) dimensions. A tungsten wire of 0.002 in diameter was used as a cathode. Kline et al. (1967) used the hydrogen bubble technique for extensive visual and quantitative studies of turbulent boundary layer. The experiments conducted in open water channels. Water speeds at order of (0.06-0.21 m/sec) were employed. A platinum wire about o.15 m long and 0.025mm diameter was used as a cathode. Burley and Grigg (1970) described a compact solid state unit which provides voltage pulses for the hydrogen bubble flow visualization technique. They used this circuit to visualize boundary layer adjacent to a continuous web of material passing through a liquid. A Nicrom wire of 0.25mm diameter and 3cm length was used as cathode for generating hydrogen bubbles and a brass rod of 3mm diameter was used as anode. Ellis and Stefan (1986) used the hydrogen bubble technique extensively for flow visualization in water and a lesser extent for velocity determination. They used a circuit similar to that used by Shraub et al.[1965]. A tungsten wire of 0.001 in diameter was used as a cathode and hydrogen bubble generator. In this research, the hydrogen bubble velocity meter has proven to be capable of measuring low water velocities (0.4-8 cm/s). Strykowaki and Sreenivasan (1990) used the hydrogen bubble visualization technique to visualize the vortex shedding behind a circular cylinder in a water channel with a free surface at Reynolds number (Re = 80). Hydrogen bubbles generated from 0.05mm diameter steel wires tensioned across the test section orthogonal to the cylinder were used as a flow markers. Mahir and Rockwell (1996) used the hydrogen bubble technique to visualize the wake regions between and downstream of a tandem arrangement of two cylinders. Experiments were carried out in a free surface, closed-loop water channel having a cross-section of (610 mm x 610 mm). The free stream velocity in the channel was (0.03m/s), at Reynolds number (160) based on the cylinder diameter (4.7mm). Platinum wire of diameter 0.025mm was used as a cathode. Hiramoto and Higuchi (2003) used the hydrogen bubble technique to visualize the vortex shedding behind a pair of circular cylinders placed side-by-side at a small angle between them. The experiments were conducted in a water channel with a 0.61 x 0.61m test section. The Reynolds number was 440 based on the free-stream velocity and the diameter of a circular cylinder. The water speed was 0.035 m/s and the diameter of the cylinder was 12.7mm. The angle between the cylinders was 2.2^{o}. Pipe and Monkewtiz (2006) used the hydrogen bubble technique to visualize the vortex shedding from a (3mm) diameter stainless steel cylinder at Reynolds number (50-150). A stainless steel wire with a diameter of (70 μm) held parallel to the cylinder axis was used to perform flow visualization of the cylinder wake. Garica et al. (2007) used the hydrogen bubble technique to visualize qualitatively the flow in tubes of (32mm) diameter with wire coils. The test section had been placed at a distance of 45 diameters from the tube entrance to ensure a fully developed flow condition. A copper wire was used as a cathode for generating hydrogen bubbles.

The objective of present work uses the hydrogen bubble generation technique to study qualitatively and quantitatively the flow patterns around bodies with different shapes in open water channel. Low water velocity range (4–8 cm/sec) is used in the experiments which ensure different Reynolds number around the bluff bodies.

Vortex ring parameters and shear layer geometry in the wake region of a circular disk versus Reynolds number are investigated, flow separation around a sphere and the vortex growth history around cylinder are identified.

Investigation the relationship between the normalized velocities near the edge of the circular disk versus Reynolds number is conducted using quantitative approach of Hydrogen bubble generation.

Experimental Set-Up And Procedure

Fig.1 shows the system used in the present work which is designed and built according to water velocity range inside the water channel. A rectangular cross section glass water channel (1.5m length × 0.12m width × 0.15m depth) dimensions is used for the visualization of the water flow patterns around bluff bodies. The entrance and the exit of open channel is made in conical shape to ensure steady and uniform free stream lines as much as possible.

Downstream of the test section channel a feed tank of (70cm × 15cm × 40cm) dimensions is fixed to provide constant water flow rate into the test section during water velocity measurements. The open channel receives water from the feed tank by (1in) diameter PVC type pipe which is fixed parallel to the channel inlet.

A (SAER) type pump of (0-6m³/h) discharge is used for circulating the water in the test section. A PVC (LZS-32) type flow meter is used for the measurement of water flow rate in the open channel. The range of the flow meter is (0.6-6 m^3/h).The water flow rate in the test section is controlled by two valves. One of these valves is fixed in the water feed line of the test section while the other is fixed in the bypass line between the downstream and upstream lines of the test section.

A (FARNELL L 30E 30volts-5 Amp) type power supply was used for water ionization .The voltage from this power supply was cut off by means of pulse generation circuit. This pulse generation circuit is used for quantitative measurements. A square wave pulse generation circuit shown in Fig.2 is used in the present experiments which was designed and built according to water velocity range inside the test section. It consists of IC 555 timer, two variable resistances (10kΩ, 4MΩ) and two capacities (1μF, 0.01μF). Rv1 was used to change the pulse duration time. Pulse generation circuit is checked and calibrated before usage by a (UT3025C) type digital storage oscilloscope. The electronic circuit that has been constructed in the present experiments to cut off the applied voltage and generate the hydrogen bubbles streaks for quantitative measurements is shown in fig.3. Sony (DSC-S2100) type digital camera is used for photography purposes of the instantaneous generated hydrogen bubbles illuminated by a light source of 1000W tungsten halogen bulb fixed a side of the channel in front of the slit prepared to pass the light in a direction parallel to the level of water ionization wire fixed inside the open channel. The test section consists of a hydrogen bubble Generation wire and photographic setup which is installed at (60cm) distance from water entrance to the test section. In the present experiments, a copper wire of 0.05mm diameter is used as a cathode for generation hydrogen bubbles. The production of acceptable light levels and contrast is strongly dependent on the angle of the incident light on the bubbles with respect to the line of sight of the camera or viewer. For best results this angle should be approximately (65˚) with respect to the perpendicular line drawn on the water surface in the opposite direction of the incident light [Shraub et al. (1965)]. Dark background is necessary and all incidents light other the collimated sheet should be minimized.

Results And Discussion

A- Qualitative Investigation

Fig.4.shows the vortex ring formed behind a circular disk of (3.6cm) diameter at different Reynolds number ranging(1605-2216).Vortex parameters measured directly from the above mentioned figure plotted versus Reynolds number which is based on disk diameter and the water velocity in the upstream region of the disk as shown in figures (5), (6) and (7) .These figures show that vortex ring radius and the distance between the vortex edge and disk edge are proportional to the Reynolds number, as they are increasing by increasing Reynolds number.

Following relationships are investigated for the above proportionalities which are applicable for the above mentioned range of Reynolds number:

$$\frac{r_v}{R_D} = 4.75 \times 10^{-8} (Re)^{2} \quad (1)$$

$$\frac{S_v}{R_D} = 1.38 \times 10^{-5} (Re)^{1.3} \quad (2)$$

Fig.8 shows the shear layer affected zone, shear layer thickness formed behind a circular disk of (3.6cm) diameter at different Reynolds number ranging (1605-2492). Shear layer parameters measured directly from the above mentioned figures are plotted versus Reynolds number based on disk diameter and the water velocity in the upstream region of the disk as shown in figures (9) and (10) which show that the distance between the position of maximum shear layer thickness and the disk rear surface and the distance between the edge of maximum shear

layer thickness and the disk edge are proportional to the Reynolds number as they are increasing by increasing Reynolds number.

Following relationships are investigated for the above proportionalities which are applicable for the above mentioned range of Reynolds number:

$$\frac{X_m}{D} = 3.2 \times 10^{-6} (Re)^{1.6} \quad (3)$$

$$\frac{S_m}{D} = 2 \times 10^{-3} (Re)^{0.7} \quad (4)$$

Fig.11 shows the growth history of the vortex behind a (3.2 cm) diameter cylinder at Reynolds number (Re =1623).The justification of this growth history is that boundary layer over the cylinder surface separates due to the adverse pressure gradient imposed by the divergent geometry of the flow environment at the rear side of the cylinder. As a result of this, shear layer is formed. The boundary layer formed along the cylinder contains a significant amount of vorticity. This vorticity is fed into the shear layer to roll up into a vortex with a sign identical to that of the incoming vorticity. Vortex (B) will grow larger than the other (A). The vorticity in the one of these vortices is in the clockwise direction, while the vorticity in the other vortex is in the anti-clock wise direction. Both directions are towards the centerline of the open channel where the wake velocity behind the cylinder approvers to zero.

Fig.12 shows the separation of streamlines from the surface of (3.8cm) diameter sphere at different Reynolds number ranging (1505-2414). Separation angle (θ) versus Reynolds number (Re) are plotted as shown in Fig.13 which shows that separation angle (θ) is proportional to the Reynolds number, (θ) as it increases by increasing Reynolds number.

Following relationships is investigated for the above proportionality which is applicable for the above mentioned range of Reynolds ranging (1500-2500):

$$\theta = 75 + 1.76 \times 10^{-3} Re^{1.1} \quad (5)$$

B- Quantitative Investigation:

Fig.14 shows the hydrogen streak generated in the water flowing in the open channel using the pulse generator circuit at different flow rates ranging (1.6-3.1 m^3/h). The streak length generated from water ionization is proportional to the water velocity by using the following equation:-

$$U_\infty^\circ = L_h \times CF \times f \quad (6)$$

Fig.15 shows the water velocity measurement using the hydrogen bubble generation (U_∞°) versus its magnitude using water flow meter (U_∞^*). Fig.16 shows the hydrogen streak generated near the edge of the disk using the pulse generator circuit at different Reynolds number ranging (1533-1680). The streak length generated from water ionization is proportional to water velocity.

Fig.17 shows that the absolute U_e° values of the water velocity near the edge of the disk measured using hydrogen bubble generation technique increases by increasing the velocity in the upstream region of the disk, U_∞°, knowing that the effect of the channel walls on water velocity is excluded by replacing the absolute values of the water velocity near the edge of the disk U_e°, by corrected value ($U_{\infty c}^\circ$) according to the real flow area:-

$$U_{\infty c}^\circ = \frac{U_\infty^\circ \times A}{A - A_d} \quad (7)$$

Fig.18 shows the normalized value of water velocity near the edge of the disk to its value in the upstream region of the disk (U_e°/U_∞°) versus Reynolds number. It is clear that the average value of this ratio is (1.08).

Conclusion

1-Radial and axial distance of the vortex formed in the wake region of a disk in low range of water velocity and its radius are proportional to the Reynolds number based on disk diameter, this could be concluded from equations(1) and (2).

2- The boundary of the wake region prolongs axially and radically to further distances as Reynolds number increases as shown from the figures related to the wake region of circular disk. This could be concluded from equations (3) and (4).

3- The separation of streamlines from the surface of the sphere proves that separation in

the laminar range of Reynolds number which is ranging from (1505-2414) takes an average value of (82.5°).

4- The pictures related to the wake region of cylinder prove that the shear layer formed along it contains a significant amount of vorticity and that the formations of these vortices are random. This conclusion is proved by some pictures extracted from the wake region of the cylinder at different time intervals

The quantitative approach of the study concludes the following:

1- The average normalized value of water velocity near the edge of the disk to its value in the upstream of the disk using hydrogen bubble generation technique demonstrates that water velocity near the edge of the disk increases by (8%). This estimation excludes the effect of water flow area change between the disk edge and the channel wall.

2-The reliability of water velocity measurement using hydrogen bubble generation is limited to velocity rang lower than 8 cm/sec with percentage error of 5% due to the adverse effect of flow disturbance on the bubbles during its movement with water flow which prevent the visualization when these bubbles across the light slit to higher lever.

Reference

Burley, R., and Grigg, P.J., "**A Solid State Pulser for the Hydrogen Bubble Flow VisualizationTechnique**" J.Phys.E:Sci.Instrum, Vol.3, 1970, PP.1018-1020.

Clutter, D.W. and Smith, A.M.O., "**Flow Visualization by Electrolysis of Water"**, Aerospace Eng, Vol. 20, 1961, pp. 24-27.

Davis, W., and Fox, R.W., "**An Evaluation of the Hydrogen Bubble Technique for the Quantitative Determination of Fluid Velocities within Clear Tubes**", Journal of Basic Engineering, Vol. 89, 1967, PP. 771-781.

Ellis, C.R. and Stefan, H.G., "**Development of Hydrogen Bubble Velocity Meter** ", Journal of Hydraulic Engineering, Vol.112, 1986, pp. 59-64.

Garcia, A. Solano, J.P., Vicente, P.G., and Viedma, A., "**Flow Pattern Assessment in Tubes with Wire Coil Inserts in Laminar and Transition regimes** ", International Journal of Heat and Fluid Flow, Vol. 28, 2007, PP. 516-525.

Hiramoto R. and Higuchi H., "**Vortex Shedding behind a Non Parallel pair of Circular Cylinders** "Journal of Fluids and Structures, Vol. 18, 2003, PP. 131-143.

Kline, S. J., Reynolds W.C., Shraub F.A. and Runstadler P.W., "**The Structure of Turbulent Boundary Layer"**, Journal of Fluid Mechanics, Vol. 30, 1967, pp. 741.

Mahir, N., and Rokwell, D. ,"**Vortex Formation from a Forced System of Two Tandem Arrangement Cylinders** ", Journal of Fluids and Structures, Vol.10, 1996, PP.473-489.

Pipe, C.J. and Monkewtiz, P.A., "**Vortex Shedding in Flows of Dilute polymer solutions**", Journal of Non-Newtonian Fluid Mechanics, Vol. 139, 2006, pp. 54-67.

Shraub, F.A., Kline, S.J., Henry, J., Runstadler, P.W., and Littell , JR. A. "**Use of Hydrogen Bubbles for Quantitative Determination of Time-Dependent Velocity Fields in Low-Speed Water Flows**", Journal of Basic Engineering, Vol. 87, 1965, PP. 429-444.

Strykowski, P.J., and Sreenivasan, K.R., "**on the Formation and Suppression of Vortex Shedding at Low Reynolds Numbers** ", Journal of Mechanics, Vol. 218, 1990, PP.71-107.

Nomenclature

Symbol	Meaning	Units
A	Flow cross section area	cm^2
A_d	Disk area	cm^2
CF	Correction factor based on the ratio of the real disk diameter to the disk diameter as measured from the photo	
D	Diameter of the disk	cm
f	Pulse frequency of pulse generator	s^{-1}
L_h	The length of the hydrogen bubbles line as measured from the photographs	cm
Q	Water flow rate	m^3/h
Re	Reynolds number	
R_D	Radius of the disk	cm
r_v	Radius of the vortex ring	cm
R_v	Distance between the vortex ring center and the disk center	cm
S	Shear layer thickness, the distance between the outer edge of the disk and the edge of shear layer initiated in the wake region of the flow across disk.	cm
S_v	Distance between the outer edge of vortex ring and the outer edge of the disk	cm
S_m	The distance between the edge of maximum shear layer thickness and the disk edge	cm
t	Time	Sec
U_∞°	Upstream water velocity measured by hydrogen bubble technique	cm/sec
U_∞^{*}	Upstream water velocity measured by flow meter	
U_e°	Velocity at the edge of the disk measured by hydrogen bubble technique	cm/sec
X_m	The axial distance between the position of maximum shear layer thickness and the disk rear surface	cm

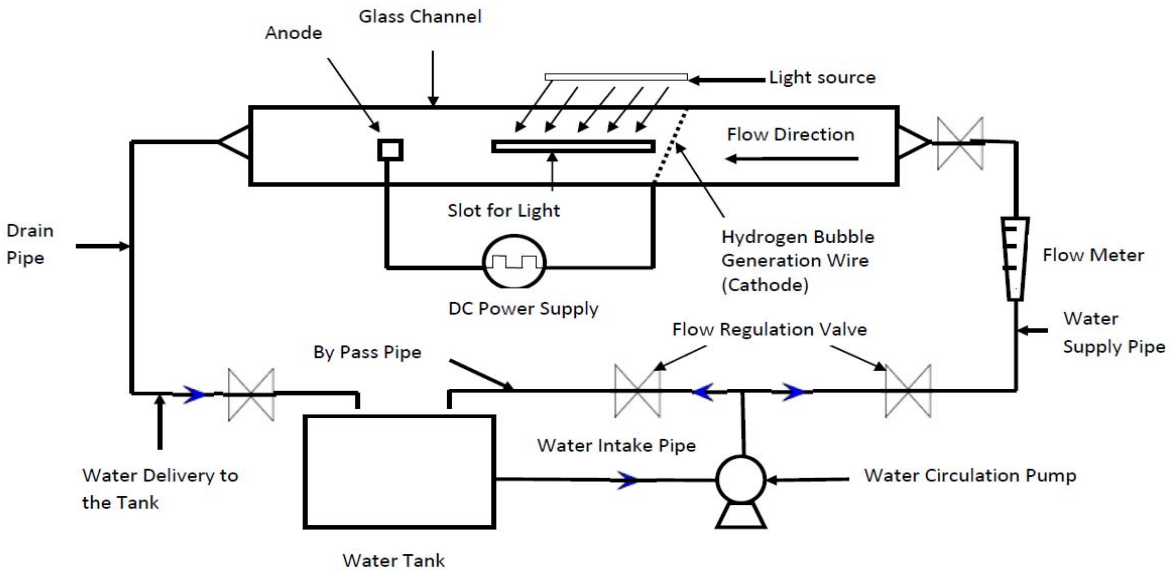

Fig.1. Configuration of water velocity measurement and flow visualization system using hydrogen bubble generation technique

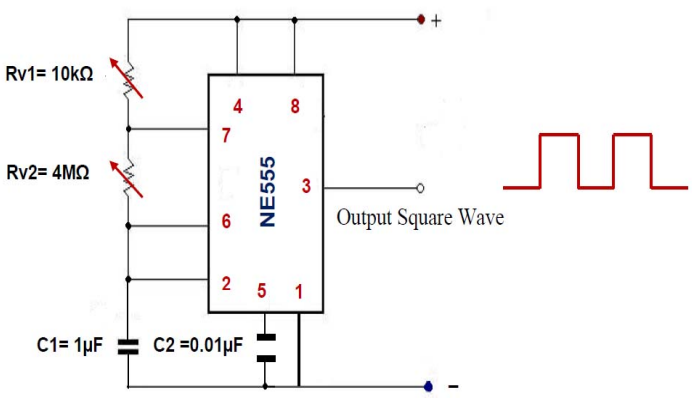

Fig. 2. Simple electronic voltage pulsing circuit with IC555 timer used in the present experiments.

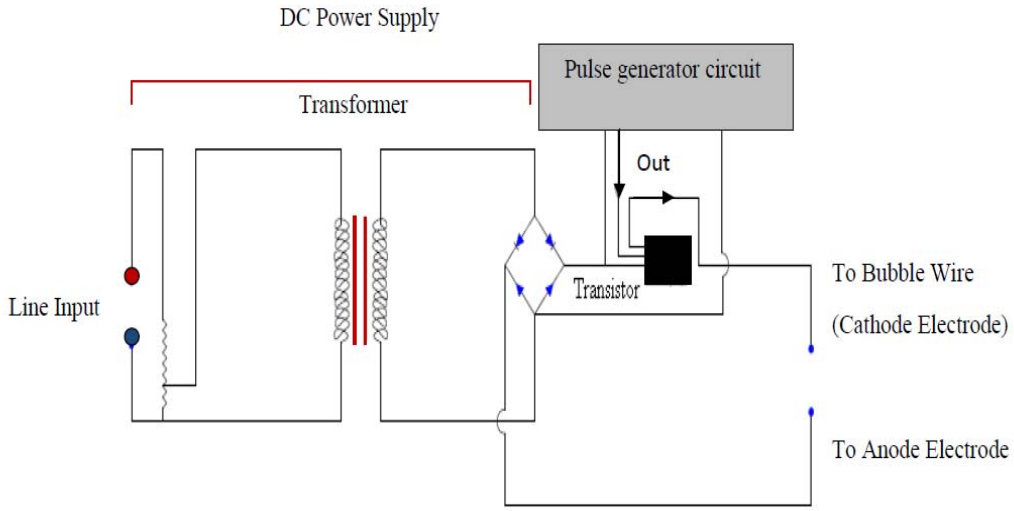

Fig.3 The electronic circuit used in the present experiments.

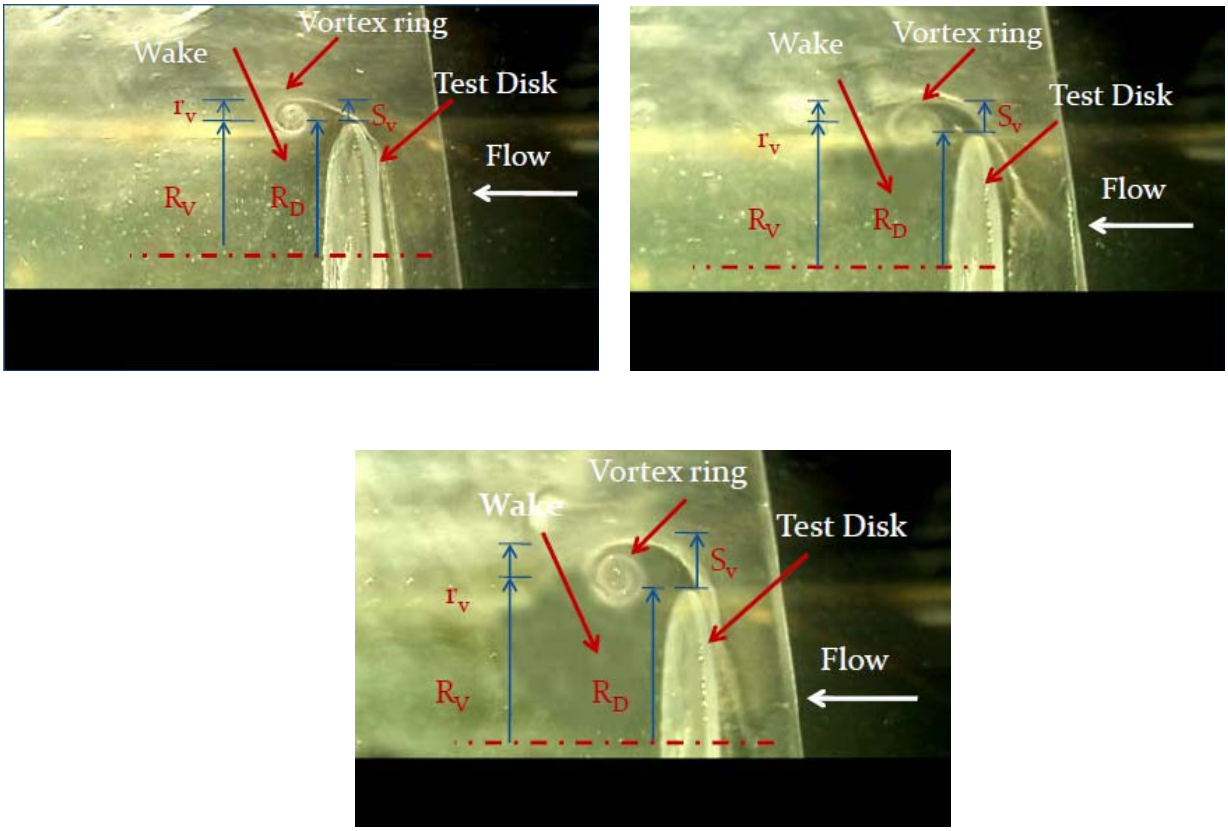

Fig.4. Vortex ring formed behind a (3.6cm) disk at Reynolds number: A (Re= 1605), B (R= 1887), C (Re= 2216)

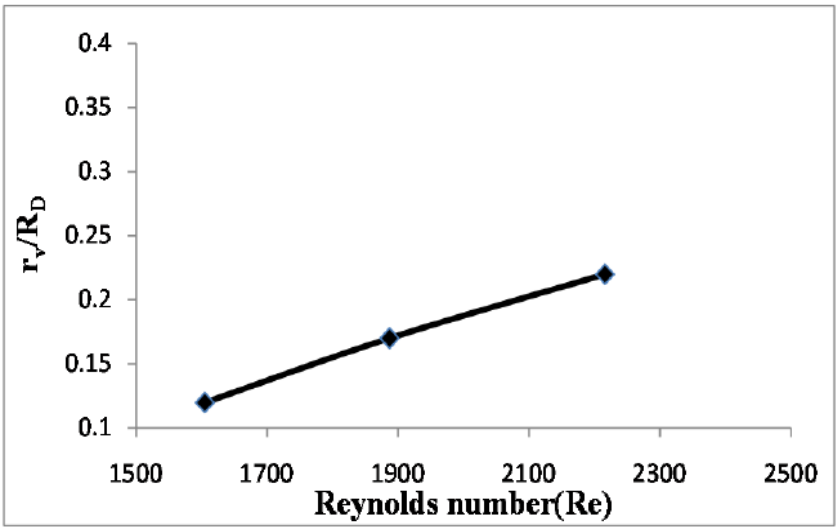

Fig.5. Normalized vortex ring radius to the disk radius versus Reynolds number.

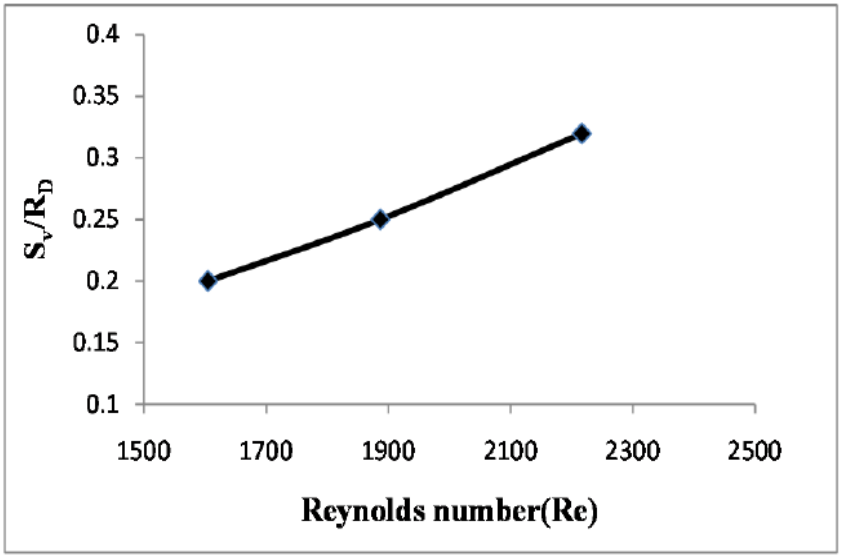

Fig.6. Normalized distance between vortex ring edge and disk edge to the disk radius versus Reynolds number

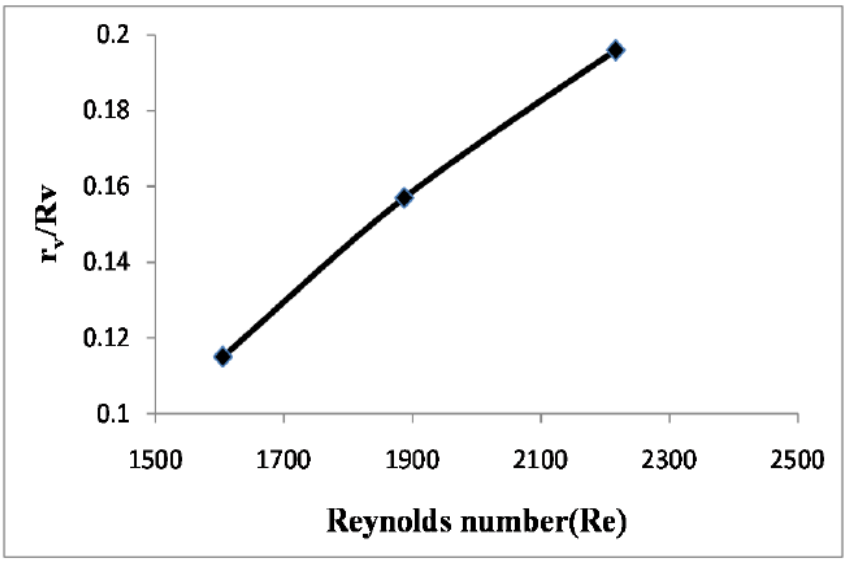

Fig.7. Normalized vortex ring radius to the distance between vortex ring center and disk center versus Reynolds number

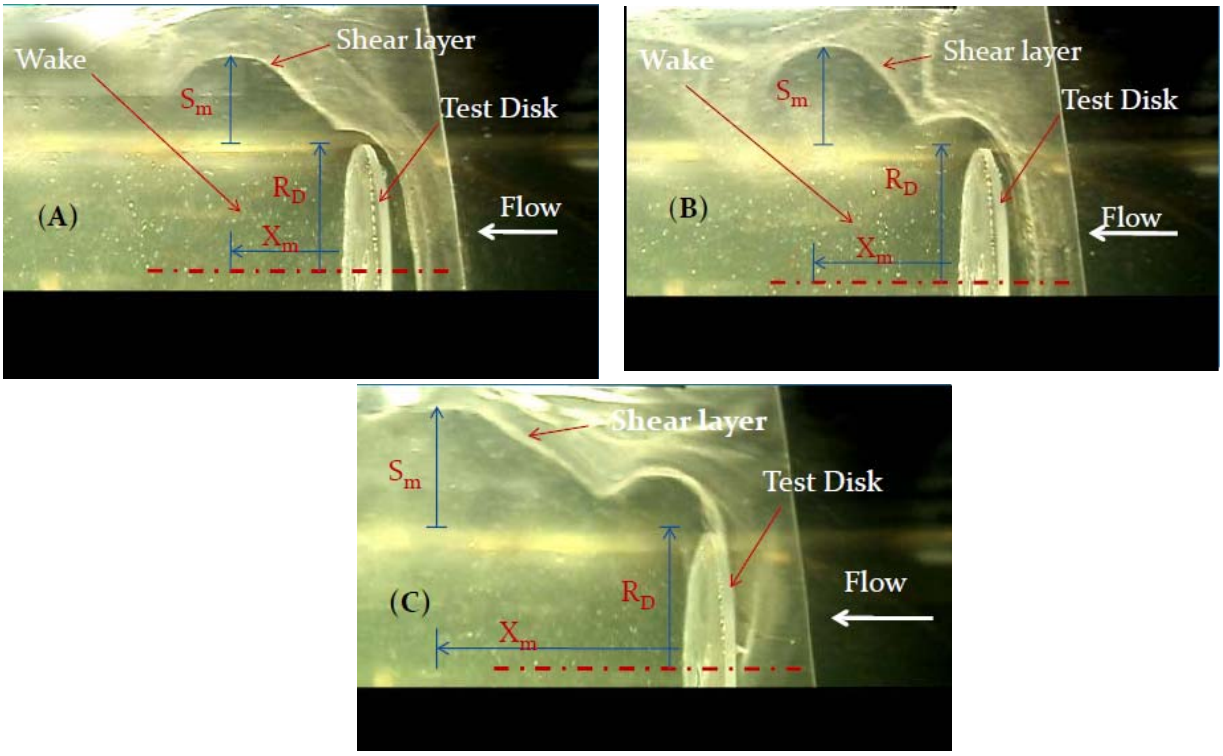

Fig.8. The wake boundary, shear layer affected zone behind a (3.6) cm disk at Reynolds number A (Re= 1605), B (R= 1887), C (Re= 2216)

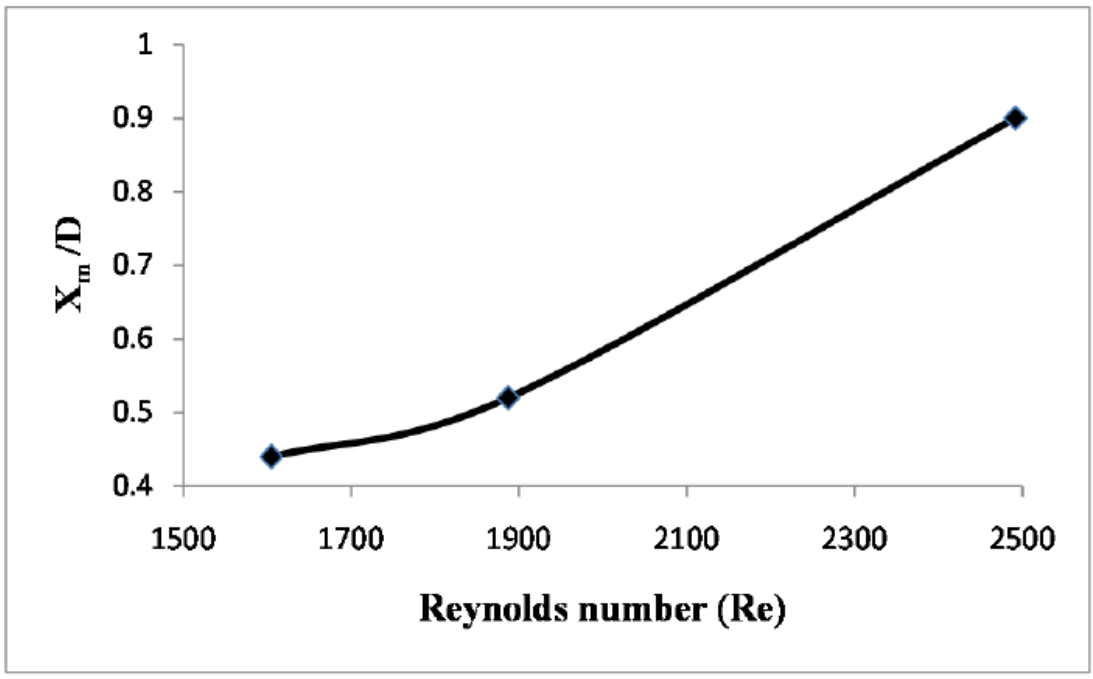

Fig.9. Normalized distance between the position of maximum shear layer thickness and disk rear surface to the disk diameter versus Reynolds number

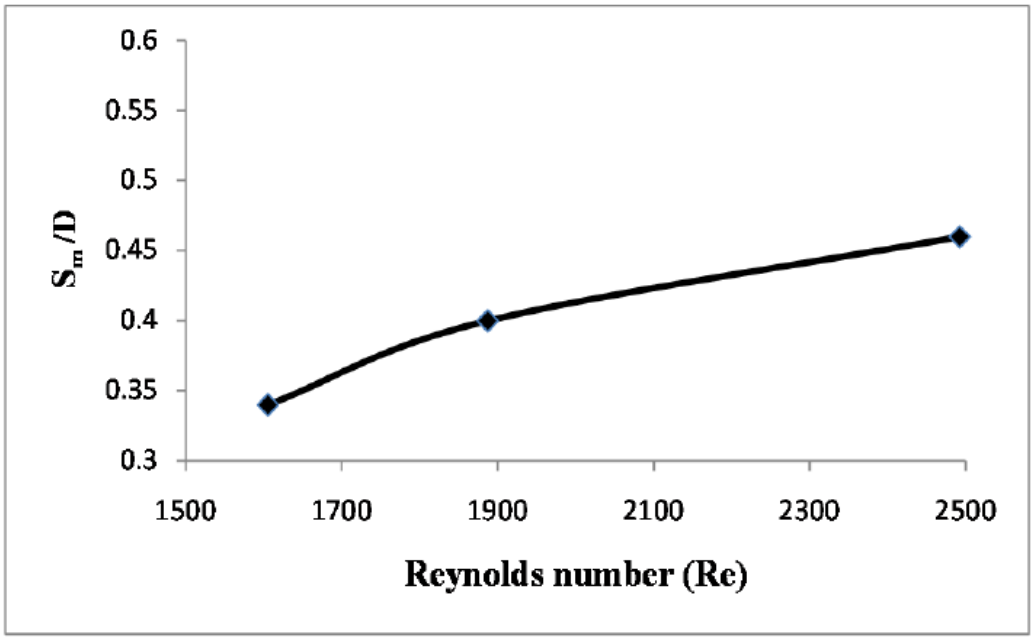

Fig.10. Normalized distance between the edge of maximum shear layer thickness and the disk edge to the disk diameter versus Reynolds number.

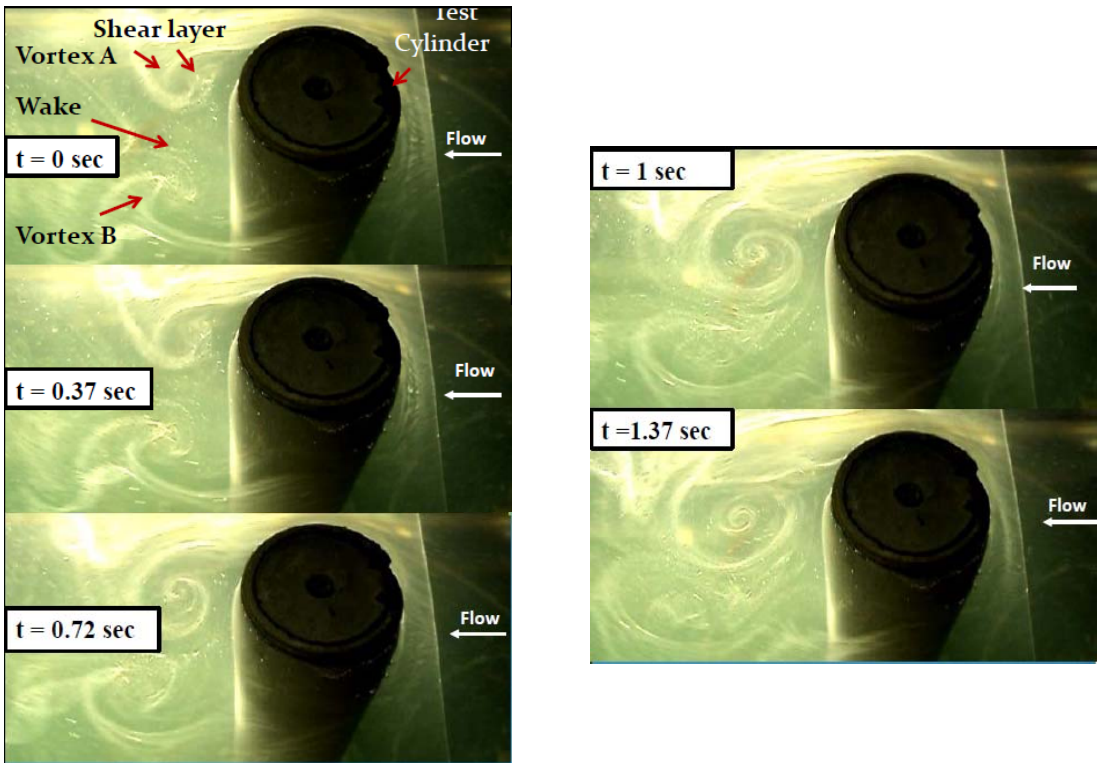

Fig.11. Development of vortex shedding in the wake region of (3.2cm) diameter cylinder at (Re =1623) during different elapsed time intervals

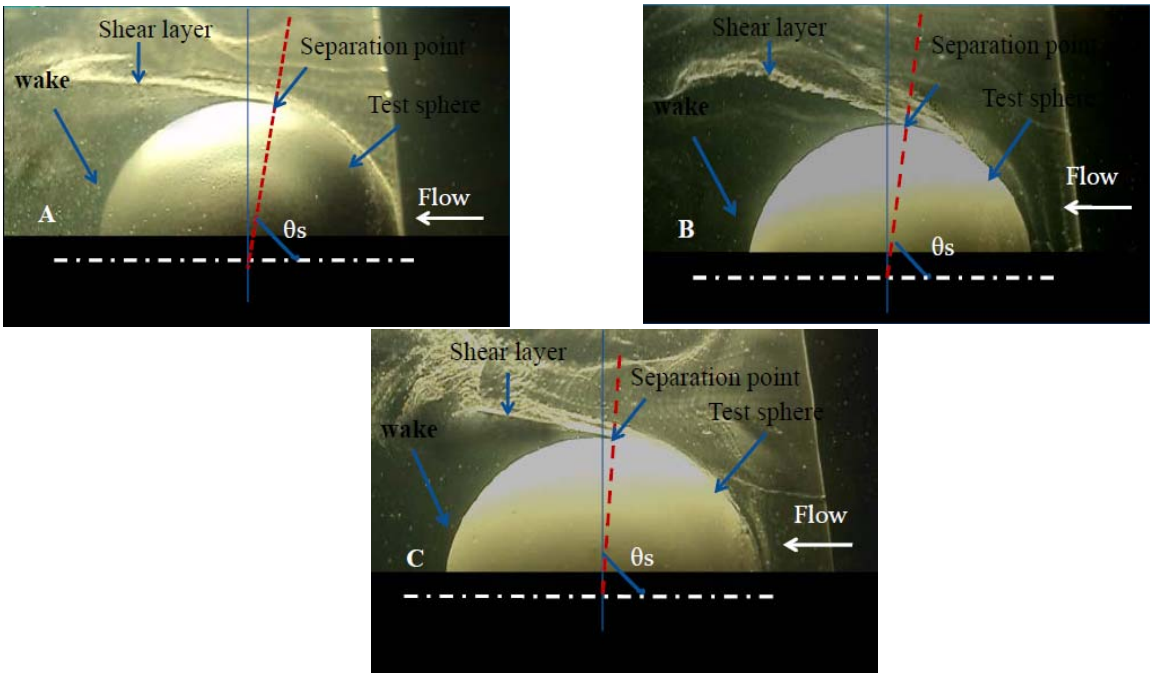

Fig.12. Flow separation from (3.8cm) sphere surface at Reynolds number A (Re= 1605), B (R= 1887), C (Re= 2216)

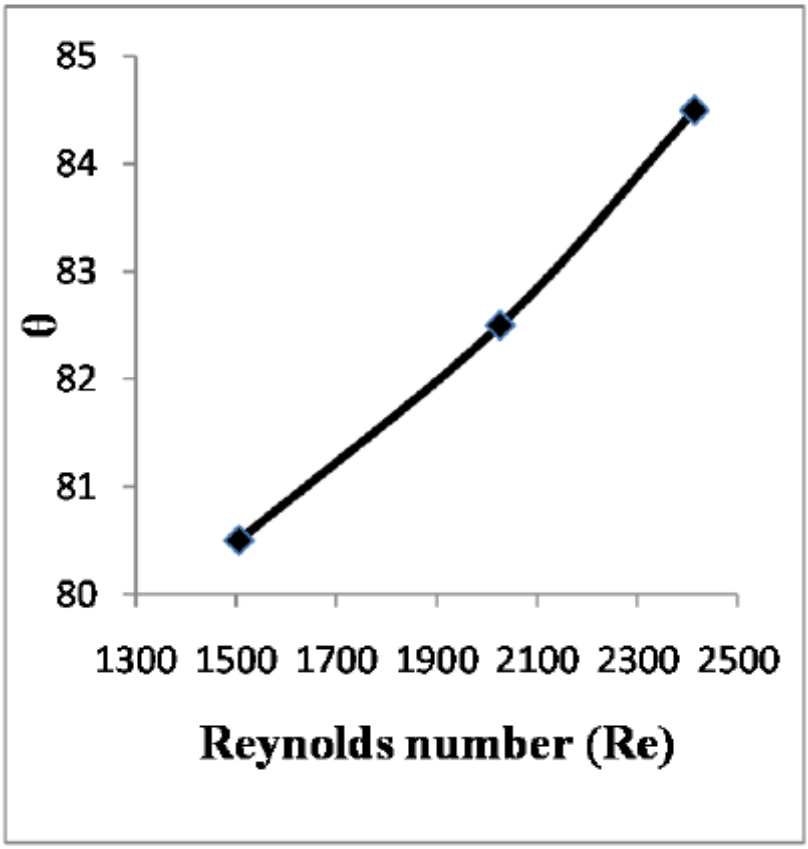

Fig.13 Flow separation angle from a (3.8cm) sphere surface versus Reynolds number

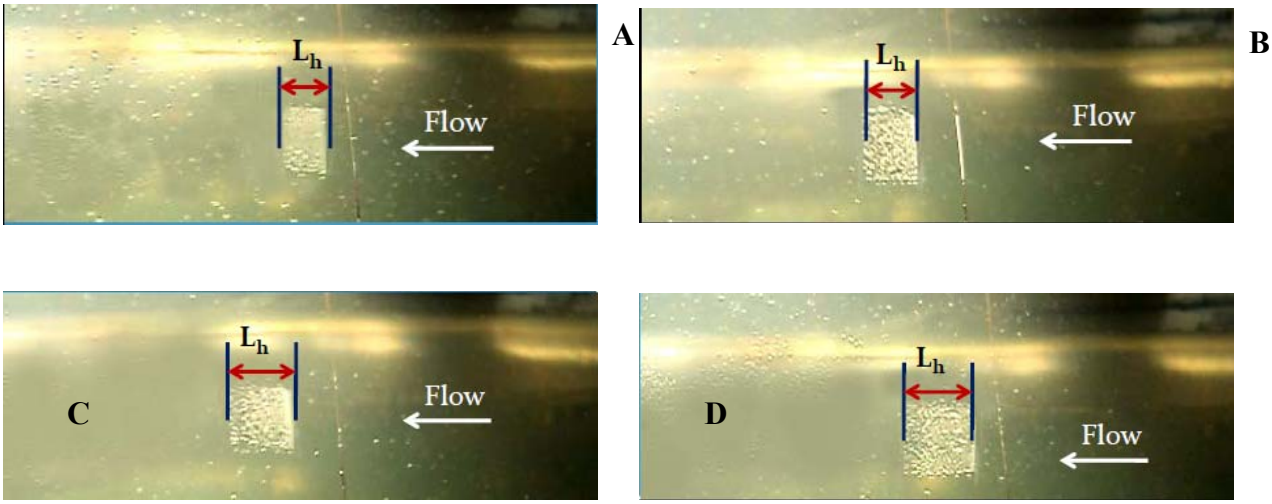

Fig.14. Water average velocity measurement in the open channel using hydrogen bubble generation technique at water flow rates: A (Q=1.6 m^3/h), B (Q= 2.1 m^3/h), C (Q=2.7 m^3/h), D (Q =3.1 m^3/h)

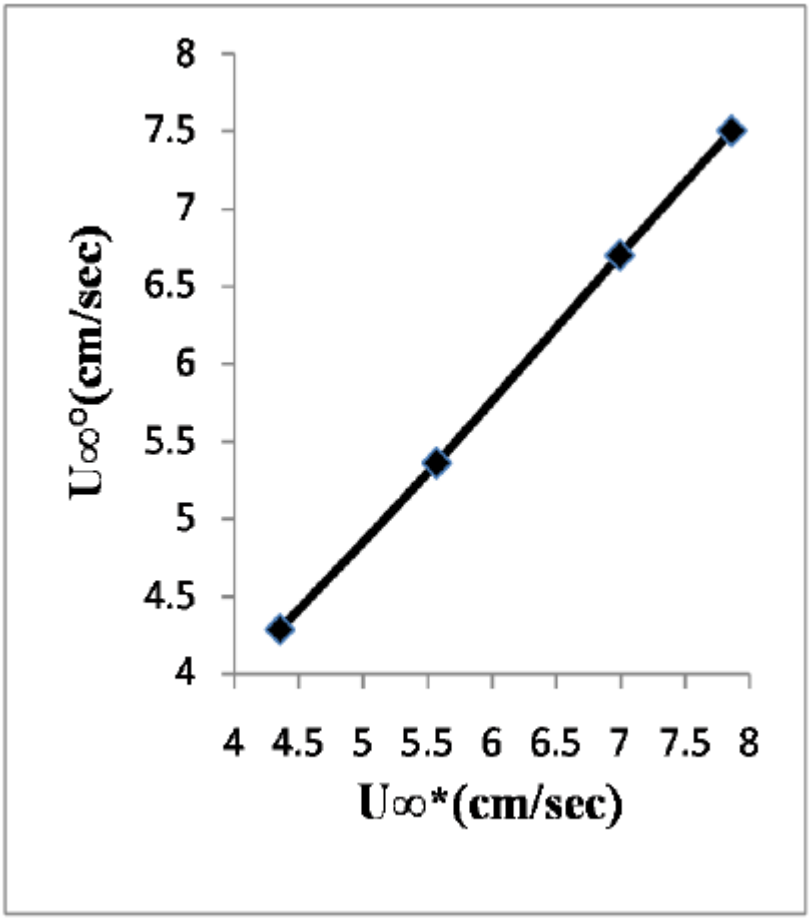

Fig.15. Water velocity measured using hydrogen bubble generation, U∞° versus its magnitude based on the water flow rate measurement, U_∞^* in the open channel

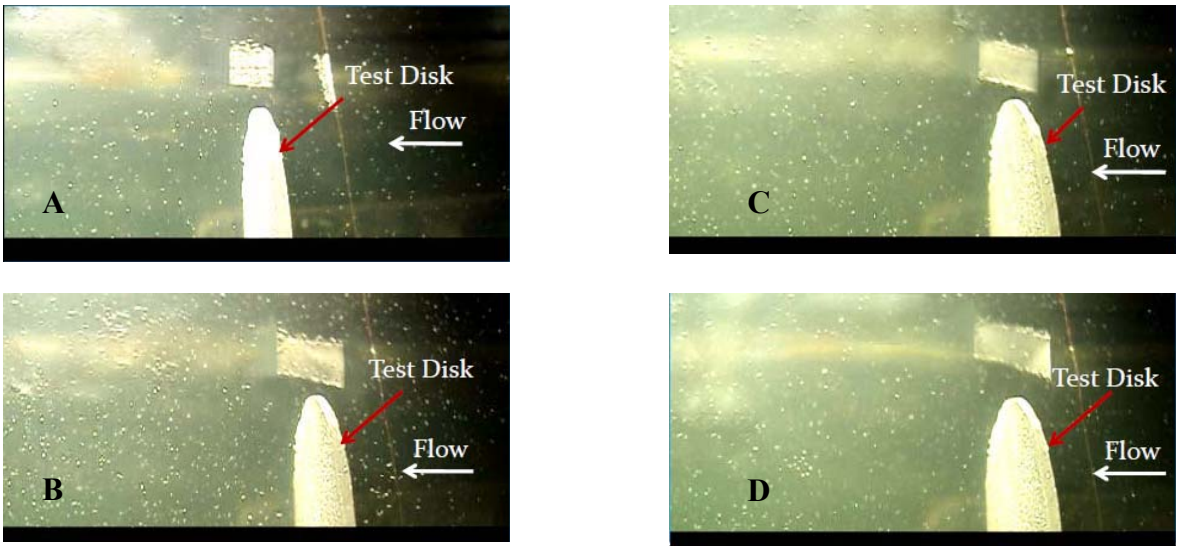

Fig.16. Water velocity measurement near the edge of the disk at Reynolds number: A (Re= 1533), B (R= 1916), C (Re= 2395), D (Re= 2680)

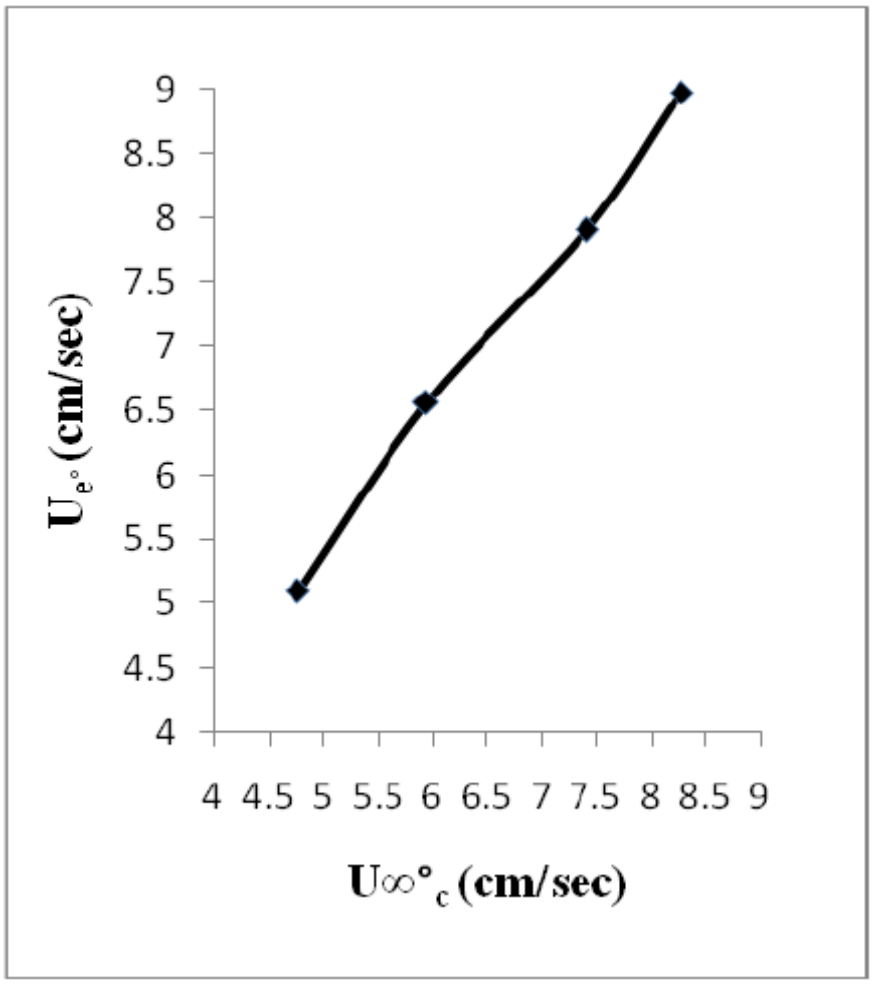

Fig. 17: Water velocity near the edge of the disk, U_e° versus its value in the upstream of the disk corrected according to the new flow area, $U_{\infty c}^{\circ}$ using hydrogen bubble generation technique.

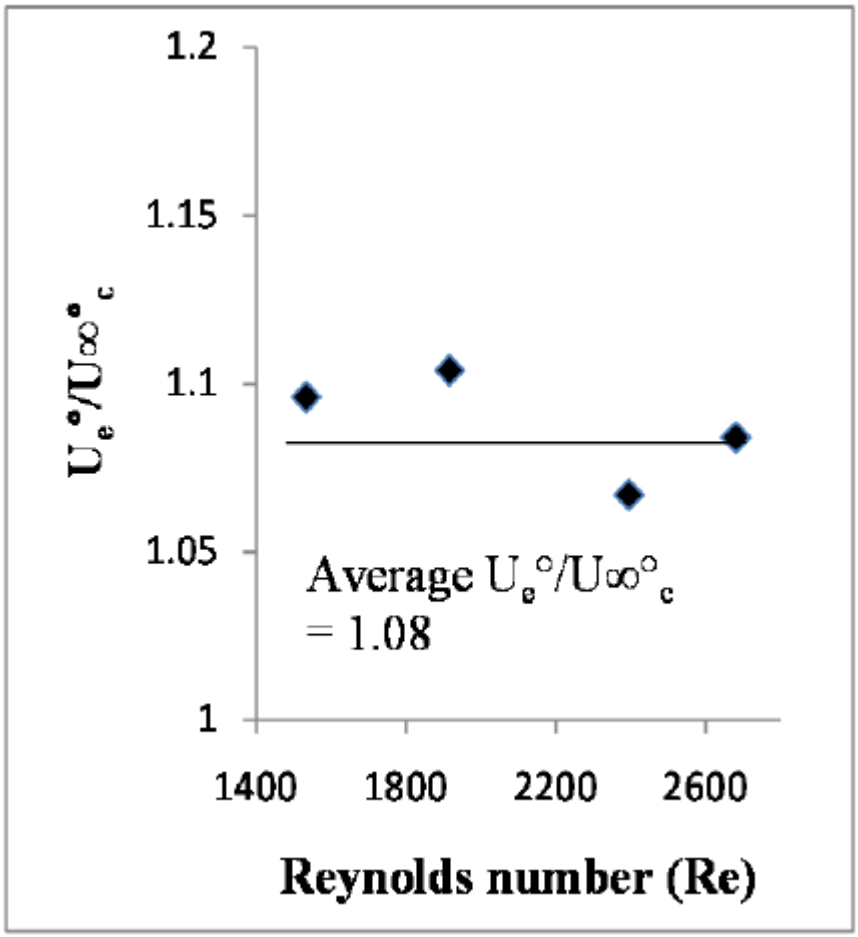

Fig.18. Water velocity near the edge of the disk normalized to its value in the upstream of the disk corrected according to the new flow area $U\infty°_c$ measured using hydrogen bubble technique versus Reynolds number

مجلة الهندسة

ISSN 1726-4073

مجلة علمية محكمة تصدرها
كلية الهندسة ـ جامعة بغداد

تموز
2012

العدد 7

المجلد 18

Journal of Engineering

ISSN 1726-4073

A Scientific Refereed Journal Published by College of Engineering University of Baghdad

July

2012

Number 7

Volume 18

Preparation of Design Charts for Estimation of the Length of an Upstream Impervious Blanket in a Homogenous Earth Dam

Raghad Samir Mahmood, M.Sc.
Department of Civil Engineering, University of Baghdad

Abstract

Earth dams are constructed mainly from soil. A homogenous earth dam is composed of only one material. The seepage through such dams is quite high. Upstream impervious blanket is one of the methods used to control seepage through the dam foundations. Bennet's method is one of the commonly used methods to design an impervious upstream blanket.

Design charts are developed relating the length of blanket, total reservoir head, total base width of the dam (excluding downstream drainage), the coefficient of permeability of the blanket material, blanket thickness, foundation thickness, and coefficient of permeability of the foundation soil, based on the equations governing the Bennet's method for a homogenous earth dam with a blanket of uniform thickness.

The length of the upstream impervious blanket can be determined by using the developed charts. The length of the blanket is inversely proportional to the coefficient of permeability of the blanket material. The length of blanket is directly proportional to the total reservoir head, total base width of the dam (excluding downstream drainage), blanket thickness, foundation thickness, and coefficient of permeability of the foundation soil.

Keywords :Earth dams, homogenous, blanket, permeability, seepage, upstream, charts.

الخلاصة

ان السد الترابي ينشا بصورة رئيسة من التربة. السد الترابي المتجانس يتركب من مادة واحدة فقط. الرشح او التسرب خلال هذه السدود عالي جدا. ان الطبقة الصماء في مقدم السد هي واحدة من الطرق المستعملة للسيطرة على التسرب او الرشح خلال اساس السد. طريقة بينت هي واحدة من اشهر الطرق المستعملة لتصميم الطبقة الصماء في مقدم السد.

تم اعداد مخطط بياني يربط العلاقة بين طول الطبقة الصماء ،شحنة الخزان الكلية ،عرض قاعدة السد(ماعدا مبزل مؤخر السد) ،معامل النفاذية لمادة الطبقة الصماء ،سمك الطبقة الصماء، سمك اساس السد، ومعامل النفاذية لتربة اساس السد بالاعتماد على المعادلات التي تحكم طريقة بينيت لسد ترابي متجانس وبسمك طبقة صماء ثابت .

يمكن الحصول على طول الطبقة الصماء باستعمال المخطط البياني المعد. يتناسب طول الطبقة الصماء عكسيا مع معامل النفاذية لمادة الطبقة الصماء ويتناسب طرديا مع شحنة الخزان الكلية ، عرض قاعدة السد(ماعدا مبزل مؤخر السد)، سمك الطبقة الصماء، سمك اساس السد، معامل النفاذية لتربة اساس السد.

Introduction

Earth dams are constructed mainly from soil. A homogenous earth dam is composed of only one material. Generally, the material used is either semi-impervious or impervious soil to limit the seepage through the dam. Homogenous earth dams are built where only one type of material is economically available near the site and the height of the dam is low. Upstream impervious blanket is one of the methods used to control seepage through the foundation. An upstream impervious blanket is usually economical. The soil used in the blanket should have a very low permeability. The thickness and length of the upstream blanket depend upon a number of factors, such as; the permeability of the blanket material, thickness of pervious foundation stratum, and the maximum depth of water in the reservoir. A longer length upto about 10 times the head is generally required for the control of sub-surface erosion and for reducing seepage to desirable limits. The thickness of the blanket usually varies from 1.5 to 3 m (Arora, 1996).

Uginchus and Roboty, 1935, discovered the differential equation of seepage in upstream blanket dams and resolved it for the dams with finite and infinite length of the blanket.

The seepage of water in the body and foundation of clay dams is one of the most important subjects in earth dam studies. This kind of seepage that is known as drainage water, is important from viewpoints of calculation of water wasting that may be a considerable percentage, stability of dam, calculation of sub pressure, calculation of thickness and length of drainages, the necessity of injection, dam wall plan and many other factors (Biswas, 2005).

Goharnejad, H., Noury, M. , Shamsaie, A., and Goharnejad, A., 2010, discussed decrease the seepage in dam's foundation, the effects of upstream clay blankets, its advantages and limitations, and the execution methods. The SEEP/W software (GEO-SLOPE Company) has been used for modeling and analyzing the seepage. The geometry and dimension of the upstream clay blanket have been studied and the results have been compared with the results of Bennet equation. Based on the above analysis and considering Bennet equation, it is suggested to use the clay blanket with the length of 150m and thickness of 0.75m which shall extend over the upstream shell. This will result in a seepage rate decreased by about 73% which seems to be more effective rather than other available methods.

The main objectives of this paper are to develop charts relating the length of blanket, total reservoir head, total base width of the dam (excluding downstream drainage), the coefficient of permeability of the blanket material, blanket thickness, foundation thickness, and coefficient of permeability of the foundation soil, based on the equations governing the Bennet's method for a homogenous earth dam with a blanket of uniform thickness.

Governing Equations

Bennet's method is one of the methods used to design an impervious upstream blanket. The Bennet solution is based on the following assumptions:

1. The permeability of the foundation soil is very large (at least 10 times) as compared to that of the blanket material,
2. The water seeps vertically through the blanket and then it moves horizontally through the foundations,
3. There is no seepage through the dam,
4. There is no natural impervious layer over or within the pervious foundation, and
5. A vertical line passing through the upstream end of the blanket is an equipotential line at the full reservoir level.

Fig. 1 is a schematic representation of an earth dam with a homogenous section provided with an impervious blanket. Details of this method can be found in reference (Bennet, 1946). The pressure head dissipated through the blanket can be expressed by:

$$\frac{d^2h}{dx^2} = \frac{K_b h}{K_f Z_b Z_f} \qquad (1)$$

in which

h=loss of head through blanket, (L),
x=horizontal distance along blanket, (L),
K_b= coefficient of permeability of the blanket material, (L/T),
K_f=coefficient of permeability of the foundation soil, (L/T),

Z_b=blanket thickness, (L), and
Z_f= thickness of the pervious foundation stratum, (L).

The solution of **eq. (1)** was obtained for the case of a blanket of uniform thickness throughout its length. Therefore, **eq. (1)** may be written as

$$\frac{d^2h}{dx^2} = a^2 h \qquad (2)$$

Where
a is constant given by $\sqrt{\frac{K_b}{K_f Z_b Z_f}}$

When **eq. (2)** is solved for the finite length of the blanket it yields:

$$X_r = \frac{1}{a}\left(\frac{e^{2ax}-1}{e^{2ax}+1}\right) \qquad (3)$$

Equivalent resistance of the foundation,(X_r), it is a measure of the efficiency of the blanket of any length x. It is defined as the length of a prism of the foundation material of thickness Z_f and permeability K_f which under a head loss h would deliver a flow equal to that actually passes through the blanket (Arora, 1996).

The loss of head through the blanket of uniform thickness is given by:

$$h_o = \left(\frac{X_r}{X_r + X_d}\right) * H \qquad (4)$$

Where
h_o=loss of head up to the end of the blanket, (L),
H=total reservoir head, (L), and
X_d=total base width of the dam (excluding downstream drainage), (L).

The percentage reduction in discharge (P) is given by:

$$P = \left(\frac{X_r}{X_r + X_d}\right) * 100 \qquad (5)$$

Design Procedure for the Blanket of Uniform Thickness

The procedure that was applied to obtain blanket length starts by assuming a suitable thickness of the blanket. The value of the parameter a is than obtained. Then, the equivalent resistance is calculated from **eq. (3)** by assuming a suitable length of the blanket. Then, the head dissipated through the blanket is determined by applying **eq. (4)** for the assumed length. The percentage reduction in the discharge is calculated by applying **eq. (5)**. Then, computations of equivalent resistance, head dissipated, and percentage reduction in the discharge is repeated for several lengths of the blanket. The maximum length of the blanket is selected such that if the length is increased. There is no appreciable change in the head dissipated and the percentage reduction in discharge.

The design procedure for a blanket of uniform thickness was computerized by using Visual basic language to facilitate the design procedure for the blanket of uniform thickness. **Fig. 2** is a flow chart to describe the main steps of the computer program used to obtain the length of the blanket.

Chart Design for the Blanket of Uniform Thickness

The computer program was used to develop design charts relating the length of blanket, the parameter a, total reservoir head, and total base width of the dam (excluding downstream drainage). The inputs used included thickness of blanket, ranging from 0.5m to 10m, thickness of the pervious foundation stratum ranging from 10m to 100m, coefficient of permeability of the blanket material ranging from 0.02m/d to 0.1 m/d, coefficient of permeability of the foundation soil ranging from 20m/d to 100m/d, and the parameter a was calculated accordingly . The height of the dam ranged between 5m and 50m. It was assumed that the minimum free board is 3m. The upstream and downstream slopes of the dam ranged between 2:1 and 4:1. The crest width (i.e. top width) was varied from 6 to 12m. Horizontal drainage blanket was not longer than two-thirds of the base width of the dam. Total base width of the dam (excluding downstream

drainage) was obtained from the following relationship:

$$X_d = (b + (m_1 + m_2) * H_t) - D \qquad (6)$$

$$H_t = H + F.B \qquad (7)$$

in which

b=crest width, (L),
m_1=upstream slope,
m_2=downstream slope,
H_t=height of the dam, (L),
D= downstream drainage width, (L), and
$F.B$=free board, (L).

A blanket length increment of 1m was used, and a calculation tolerance limit of 0.002 units, for both head dissipated and percentage reduction in discharge, was adopted.

By applying regression technique relationship among the length of blanket in meters, the parameter *a*, total reservoir head in meters, and total base width of the dam (excluding downstream drainage) in meters was obtained, with a correlation coefficient of 0.935; this relationship is expressed as follows:

$$L_b = 107.6H^{0.38}X_d^{0.21}e^{-152.58a} \qquad (8)$$

In which

L_b=length of the blanket, (L).

Fig. 3 shows the design charts relating the length of blanket, the parameter *a*, total reservoir head, and total base width of the dam (excluding downstream drainage). The length of the blanket is inversely proportional to the parameter *a* and directly to the total reservoir head and total base width of the dam (excluding downstream drainage). From the results depicted in **Fig. 3** it can be seen that at small values of the parameter a, the effect of the total base width of the dam (excluding downstream drainage) and total reservoir head on the length of the blanket is larger than its effect at the large values of a. At small total base width of the dam (excluding downstream drainage) the effect of the parameter *a* on the length of the blanket is smaller than its effect at large widths. At low total reservoir head the effect of the parameter *a* on the length of the blanket is smaller than its effect at high heads.

Several factors were taken into consideration when trying to investigate the effect of the parameter *a* on the length of the blanket. These factors include blanket thickness, thickness of the pervious foundation stratum, coefficient of permeability of the blanket material, and coefficient of permeability of the foundation soil on the blanket length. Total reservoir head was set at 17m, and total base width of the dam (excluding downstream drainage) was set at 77m. **Fig. 4** shows the effect of blanket thicknesses and thickness of the pervious foundation stratum on the length of the blanket with the coefficient of permeability of the blanket material being 0.07m/d, and coefficient of permeability of the foundation soil being 70m/d. The length of the blanket is directly proportional to the blanket thickness and foundation thickness.

Fig. 5 shows the effect of using different coefficients of permeability of the foundation soil and coefficient of permeability of the blanket material on the length of the blanket with a blanket thickness of 1.5m and a thickness of the pervious foundation stratum of 10m. It is clear that the length of the blanket is inversely proportional to the coefficient of permeability of the blanket material and directly proportional to the coefficient of permeability of the foundation soil.

Conclusions

The following conclusions can be withdrawn:

1. The length of the upstream impervious blanket can be determined by using the developed charts relating the length of blanket, the parameter *a*, total reservoir head, and total base width of the dam (excluding downstream drainage), based on the equations governing the Bennet's method for a homogenous earth dam with a blanket of uniform thickness.
2. The length of the blanket is directly proportional to the total reservoir head and total base width of the dam (excluding downstream drainage).
3. The length of the blanket is directly proportional to the blanket thickness and foundation thickness.
4. The length of the blanket is inversely proportional to the coefficient of permeability of the blanket material and directly proportional to the coefficient of permeability of the foundation soil.

Recommendations

The following recommendations are found to provide a guide for further studies:

1. Prepare design charts for the length of upstream impervious blanket for a homogenous earth dam with a blanket of variable thickness.
2. Prepare design charts for the length of upstream impervious blanket for a zoned earth dam for the two cases: blanket of uniform and variable thickness.
3. Study the optimal design criteria for the upstream impervious blanket.

References

- Arora, K. R., 1996, Irrigation, Water Power and Water Resources Engineering, 4th Edition, Standard Publishers Distributors, 1705-B, Nai Sarak, Delhi-110006.

- Bennett, P.T., 1946, The Effect of Blanket on Seepage through Pervious Foundation, trans. ASCE, 3: 52-61.

- Biswas, S., 2005, Study of Cohesive Soil-Granular Interaction Incorporating Critical Hydraulic Gradient and Clogging, School of Civil, Mining and Environmental Engineering, pp: 264.

- Goharnejad, H., Noury, M. , Shamsaie, A., and Goharnejad, A., 2010, The Effect of Clay Blanket Thickness to Prevent Seepage in Dam Reservoir, J. Environ. Sci. 4(6):558-565.

- Uginchus, A., 1935, Seepage through Earth Dams with Aprons, Moskvavolgostroi, 11: 67-79.

- Wilson, S.D., 1979, Current Trends in Design and Construction of Embankment Dams, ASCE, New York, pp: 57-65.

List of Symbols

a =a parameter,
b=crest width, (L),
D= downstream drainage width, (L),
$F.B$=free board, (L),
h=loss of head through blanket, (L),
H=total reservoir head, (L),
h_o=loss of head up to the end of the blanket, (L),
H_t=height of the dam, (L),
K_b= coefficient of permeability of the blanket material, (L/T),
K_f=coefficient of permeability of the foundation soil, (L/T),
L_b=length of the blanket, (L),
m_1=upstream slope,
m_2=downstream slope,
P=percentage reduction in discharge, (%),
x=horizontal distance along blanket, (L),
X_d=total base width of the dam (excluding downstream drainage), (L),
X_r=Equivalent resistance of the foundation,
Z_b=blanket thickness, (L), and
Z_f= thickness of the pervious foundation stratum, (L).

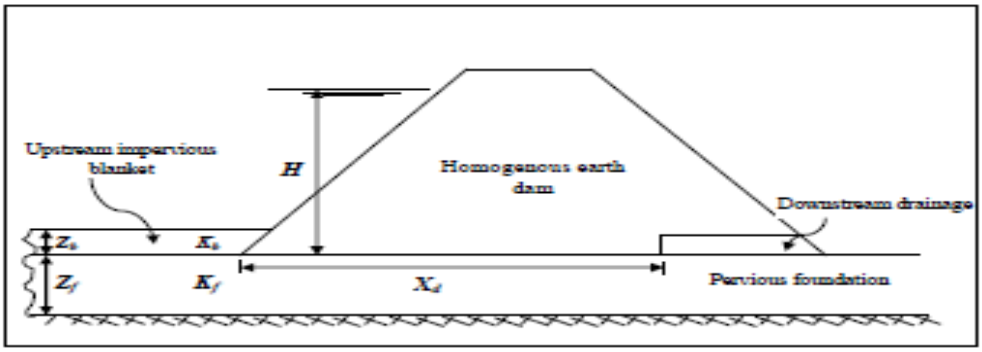

Figure. (1). A Schematic Diagram of a Homogenous Earth Dam.

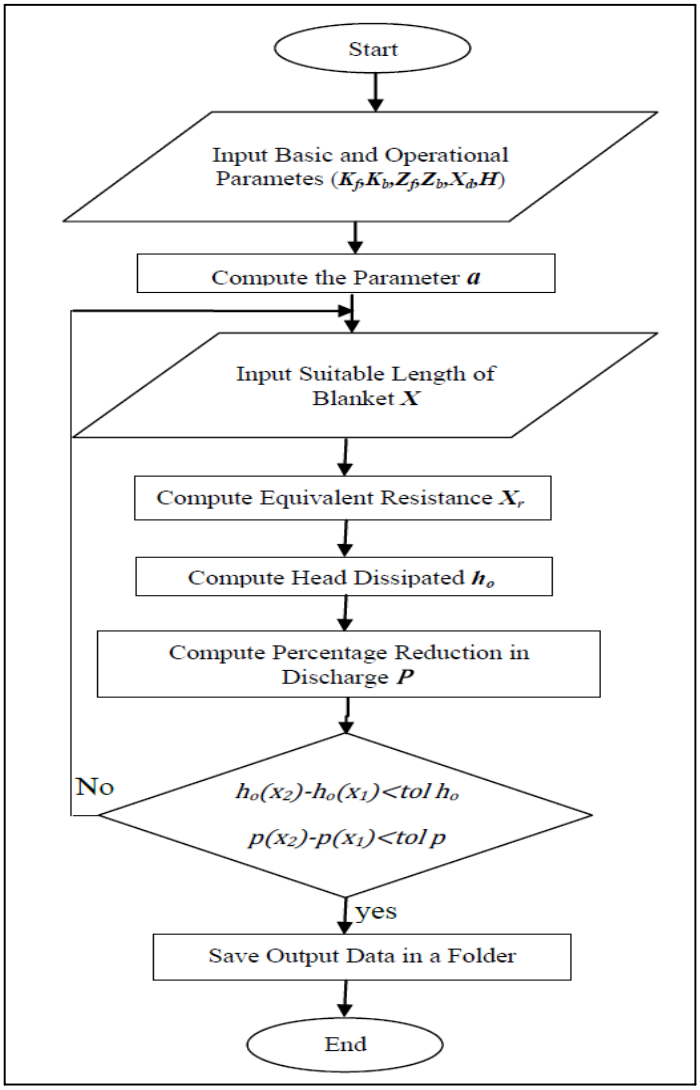

Figure. (2). Flow Chart of the Computer Program Used to Obtain the Length of the Blanket.

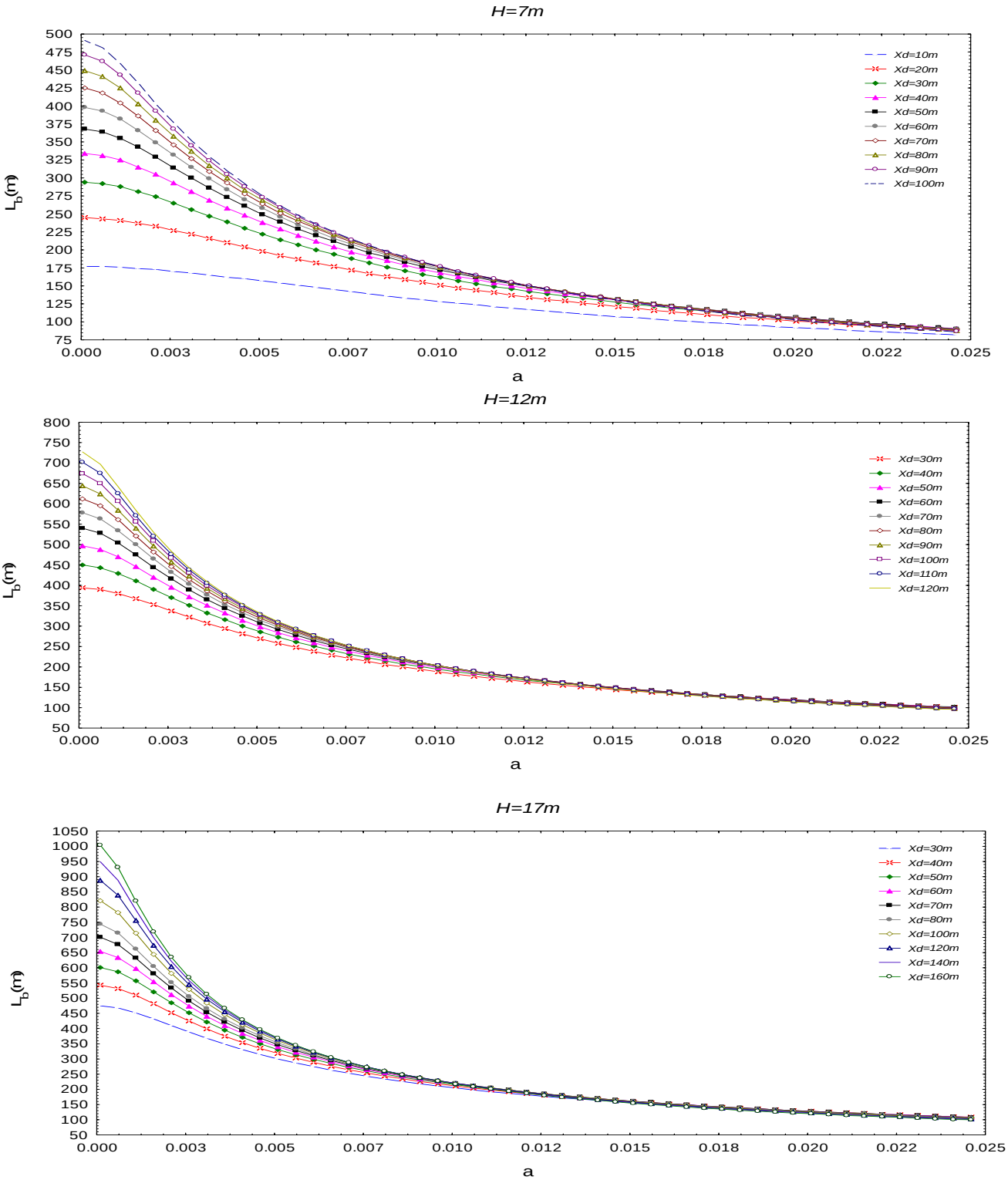

Figure.(3). Design Chart for the Length of Upstream Impervious Blanket for a Homogenous Earth Dam for the Blanket of Uniform Thickness.

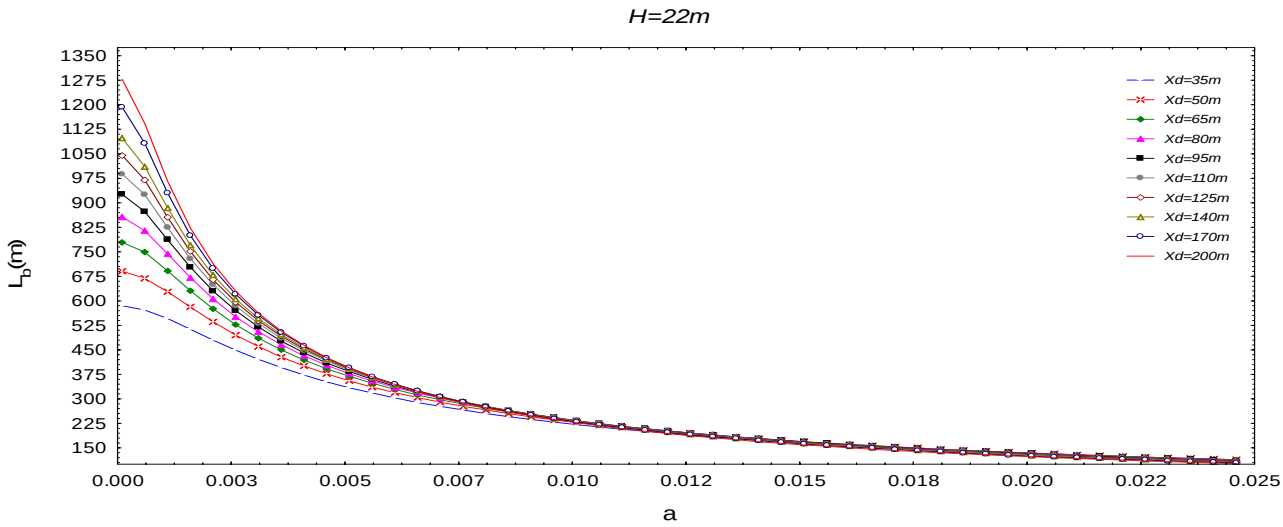

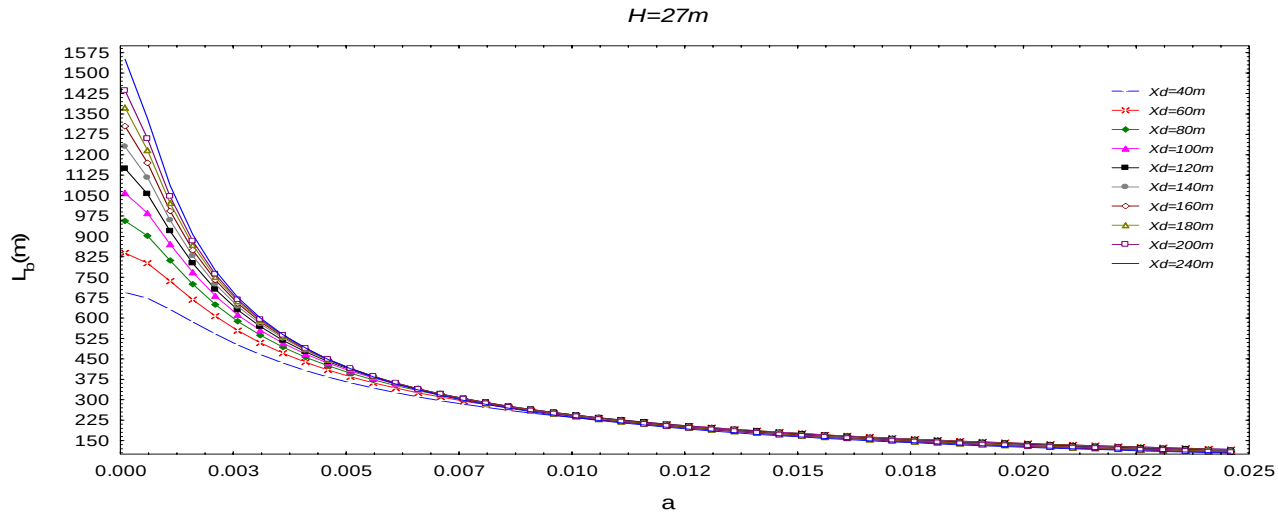

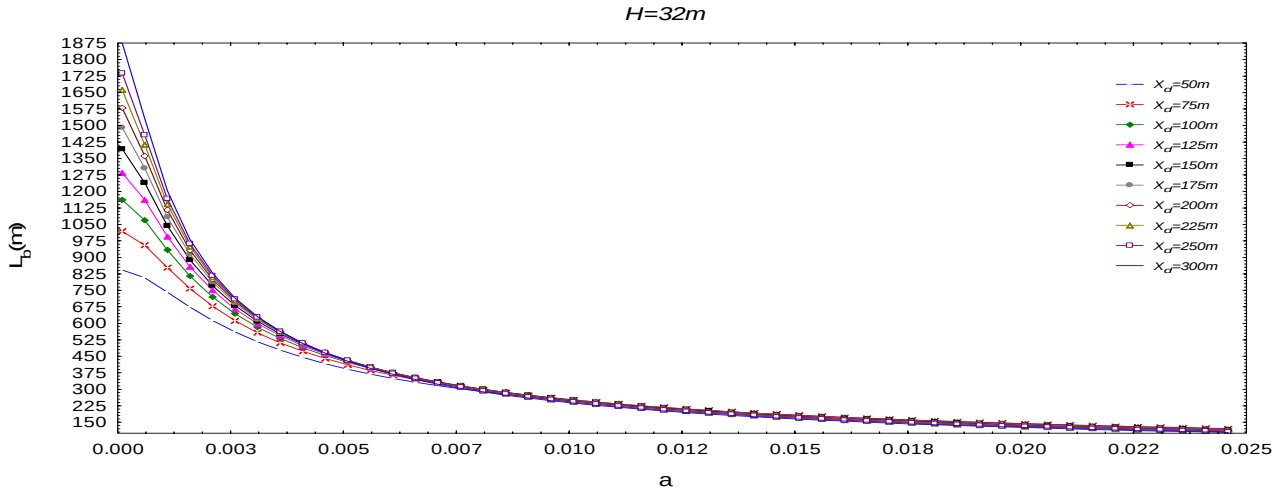

Figure.(3). Cont.

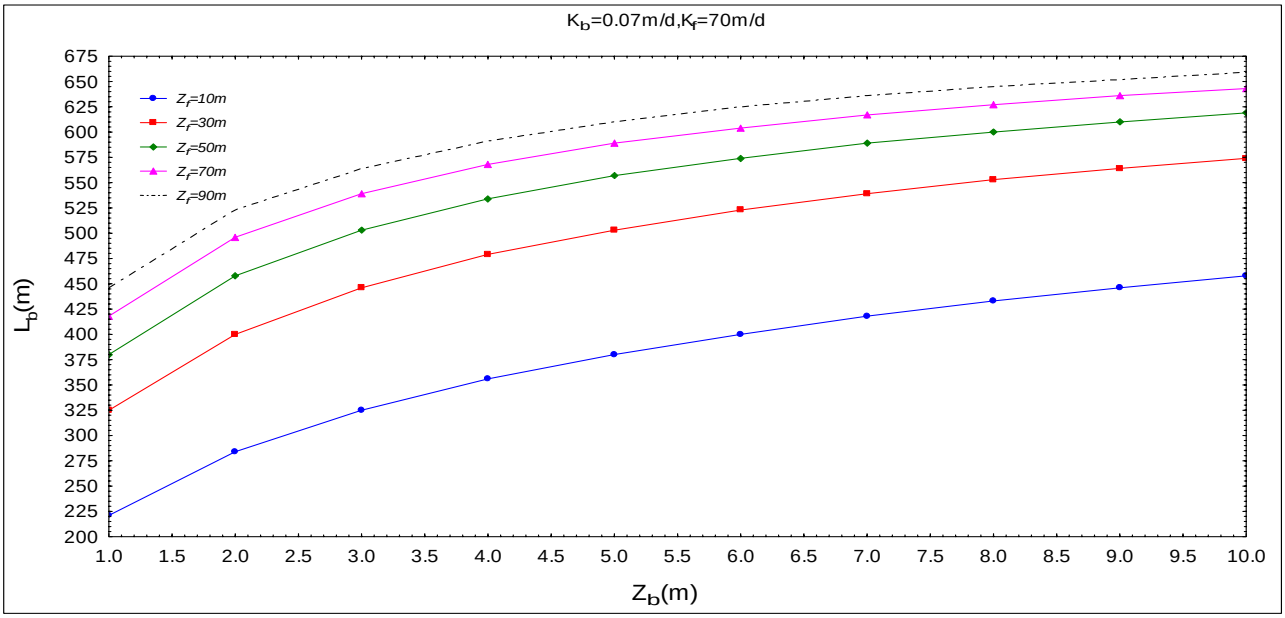

Figure. (4). Effect of Using Different Blanket Thicknesses and Thickness of the Pervious Foundation Stratum on the Length of the Blanket.

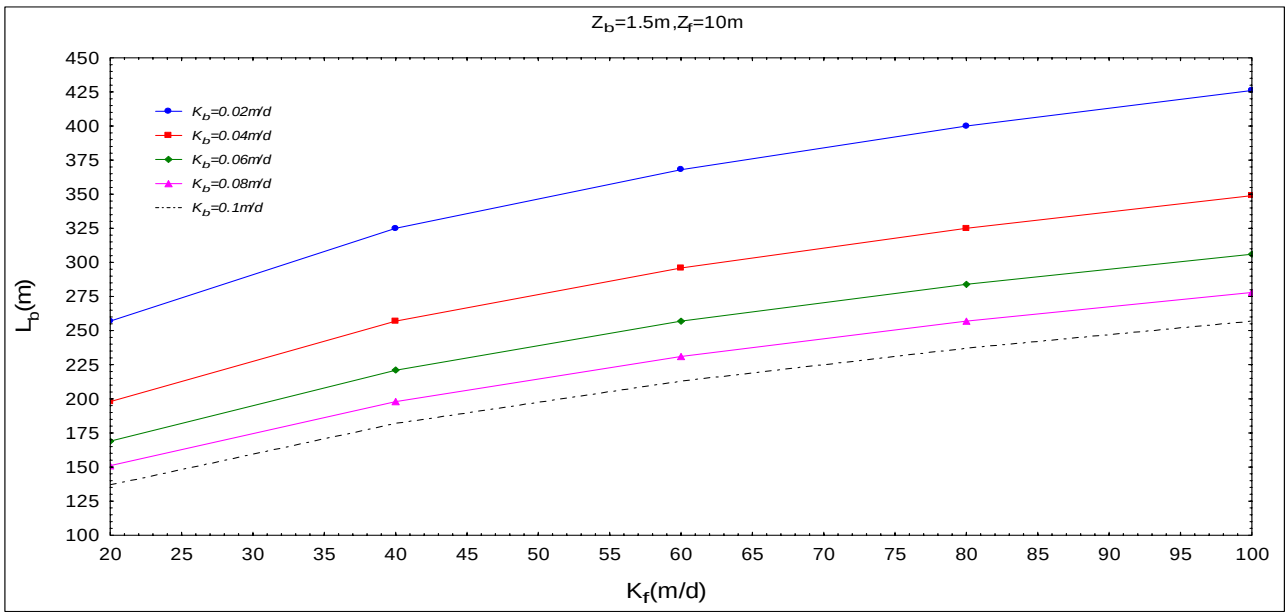

Figure. (5). Effect of Using Different Coefficients of Permeability of the Foundation Soil and Coefficient of Permeability of the Blanket Material on the Length of the Blanket.

Removal of Cadmium Ions from Simulated Wastewater Using Rice Husk Biosorbent

Assist. Prof. Dr. Shahlaa Esmail Ebrahim and Sarah Yaarub Mohammed
shahlaaaga@yahoo.com eng_sarahyaarub@yahoo.com
Baghdad University, College of Engineering, Environmental Engineering Department

Abstract

Biosorption of cadmium ions from simulated wastewater using rice husk was studied with initial concentration of 25 mg/l. Equilibrium isotherm was studied using Langmuir, Freundlich, BET and Timken models. The results show that the Freundlich isotherm is the best fit model to describe this process with high determination coefficient equals to 0.983. There was a good compliance between the experimental and theoretical results. Highest removal efficiency 97% was obtained at 2.5g of adsorbent, pH 6 and contact time 100 min.

Keywords: **Cadmium, Biosorption, Rice Husk, Natural Adsorbents, Isotherm Model**

ازالة ايونات الكادميوم من المياه المحضرة مختبرياً باستخدام قشور الرز كمادة مازة طبيعية

أ.م.د. شهلاء اسماعيل ابراهيم و م.أ. سارة يعرب محمد
جامعة بغداد- كلية الهندسة – قسم الهندسة البيئية

الخلاصة:

تم دراسة عملية امتزاز ايونات الكادميوم (بتركيز 25 ملغرام \ لتر) من المزيج المحضر مختبريا باستخدام مادة طبيعية هي قشور الرز كمادة مازة. وقد استخدمت عدة موديلات لتمثيل عملية الامتزاز ووجد ان Freundlich model هو الموديل الافضل. وان كفاءة عملية الامتزاز تتأثر بشكل واضح بكمية المادة المازة و قيمة ال pH حيث وجد ان اعلى كفاءة (97 %) تم الحصول عليها عند استخدام 2.5 غرام من المادة عند 6pH وبزمن 100 دقيقة .

الكلمات الرئيسية: الكادميوم ، الامتزاز الحيوي، قشور الرز، المواد المازة الطبيعية ، التمثيل الرياضي.

1. Introduction

Among the various known forms of pollution, water pollution is of great concern, years of increased industrial, agricaltural and domestic activities have resulted in the generation of large amount of wastewater containing a number of toxic pollutants.

The presence of heavy metals in the environment is a major concern because heavy metals will not degrade into harmless end products and it is toxicity for many life forms; it is accumulate in living organisms, causing various diseases and disorders. Therefore, the elimination of heavy metals from water and wastewater is important to protect public health and ecosystem (Cheung *et al*., 2001).Cadmium is one of the principal heavy metals responsible for causing kidney damage, renal disorder, high blood pressure, bone fracture and destruction of red blood Cells

It is discharged in the effluents of many industries such as electroplating, paint pigments, plastics manufacturing, mining and metallurgical processes (Drush, 1993).

Cadmium is widely used and extremely toxic in relatively low dosages, human beings have reported nausea and vomiting at a level of 15 mg/l of cadmium, with no adverse effects at 0.05 mg/l (Kumar *et al*., 2010). The drinking water guideline value recommended by World Health Organization (WHO) is 0.005 mg Cd/l. As a resulte of the serious efforts of researchers all over the world in the field of pollution control and management a number of methodologies with varying degrees of success have been developed. 'Adsorption' is process which considered the better as compared to other methods because of convenience, easy operation, simplicity of design, and it has been shown to be an economically feasible alternative method for removing trace metals from wastewater and water supplies. Further this process can remove/minimize different types of pollutants, while activated carbon has been the most used adsorbent; nevertheless, it is relatively expensive. Cost is an important parameter for choosing the adsorbent materials

In general, adsorbent can be assumed to be low cost if it requires little processing, abundant in nature or a byproduct or waste material from another industry (Bailey *et al*., 1999).

Many materials which they are cheap and readily available sources such as coal, coke, peat, wood, or rice husk may be successfully employed for the removal of cadmium and other toxic heavy metals from aqueous solutions (Ajmal*et al*., 2003).

The utilization of agricultural waste materials is increasingly becoming important concern because these wastes represent unused resources and, in many cases, present serious disposal problems (Sun and Shi, 1998).

2 Materialand Methods

2.1 Materials (Stock Solutions)

A stock solution of cadmium ions with desired concentration was prepared by using $Cd(NO_3)_2$. Cadmium nitrate was dissolved in distilled water and analysis by atomic absorption spectrophotometer (Buck, USA).

2.2 Preparation of Biosorbent

The rice husk used was obtained from local Iraqi mill. The rice husk was crushed, sieved to 0.775 mm in diameter; and washed with distilled water to remove impurities; then dried by exposure to the sun light for 12 hr. The dried husk was stored in desiccators until used.

Table 1 Listed the physical & chemical property.

2.3 Experimental System

The different weight of adsorbent (0.1, 0.2, 0.5, 1, 2 and 2.5)g were usedto study the adsorption isotherm. The adsorbents were put in 250 ml volumetric flask with 100 ml of cadmium solution (conc. =25 mg/l). The pH of the solutions was adjusted to the pH 6 using 0.1M NaOH or 0.1M HNO_3. Thenthe flasks placed on a shaker (SM-25, Edmund bühler, Germany)and agitated continuously for 3hr at 150 rpm. The samples were filtered by filter paper (Whatman 42). The adsorbed amount was calculated by the following equation (Sulaymon*et al*., 2010):

$$q_e = \frac{V_L(C_o - C)}{W} \quad (1)$$

Where C_o and C are the initial and equilibrium concentrations (mg/l) of cadmium solution, respectively; V_L is the volume of solution (l), and W is the mass (g) of the adsorbent

The biosorption isotherms were obtained by plotting the mass of solute adsorbed per unit mass of adsorbent (q_e) against the equilibrium concentration of the solute in the solution (C).

2.4Fourier-Transform Infrared Analysis (FT-IR)

In order to determine which functional groups were responsible for metal uptake, an FT-IR analysis in solid phase was performed on the biomass prepared in a KBr disk. FT-IR spectra were obtained for adsorbent solid samples before and after the biosorption process. Dry biomass samples were examined with the FT-IR spectrophotometer (Shimadzu FTIR 8000).

A 2.5 g of dry biomass was placed in 100 ml of Cd(II) solutions of 25 mg/l concentration. The contents of volumetric flask were adjusted to pH value of 6. The samples were shacked for 100 min at agitation speed of 150 rpm, the supernatant was discarded and the biomass was left to dry. Dried samples were collected and analysis.

2.5 Biosorption Isotherms Model

The analysis of the isotherm data by fitting them to different isotherm models is an important step to finding a suitable model that can be used for design purpose. The biosorption capacity of this system was investigated with the Langmuir, Freundlich, BET and Temkinbiosorption isotherms models.

3.1 Results And Discussion

Mass of adsorbent is one of the important parameters in biosorption processes because it determines the capacity of an adsorbent for a given initial concentration of the adsorbate. Under a given set of operating conditions this effect is explain in **Fig.1** and **2**. These figures show that the adsorption of Cd(II) increases rapidly with increasing the mass of adsorbent from 0.1 to 2.5 g with removal efficiency from 20 to 97 % .

The increase in the removal efficiency may be attributed to the fact that, with an increase in the mass of adsorbent, more adsorbent surface is available for the solute to be adsorbed. While a significant decrease in uptake was observed when the mass was increased and the maximum up take was obtained is 9 mg of Cd(II)/g of rice husk.

Also, the percentage removal of metal ion was decreased with the decrease in pH, because the competition between protons and metal ions for sorption sites on the adsorbent surface. This is due to the fact that hydrogen ions themselves are a strong competing sorbate in one hand and the contaminant decreases the negative charge of the same surface in another hand. **Fig.3** show that the percentage removal of Cd(II) was increased as the pH of the solution increased.

Although a maximum uptake was noted at a pH of 8.As the pH of the solution increased to more than 7, Cd(II) started to precipitate out from the solution (Hengpeng*et al*., 2010). Therefore, the increased capacity of biosorption at pH more than 7 may be a combination of both biosorption and precipitation on the surface of the adsorbents. This condition is often not desirable, as the metal precipitation could lead to incorrect values of the adsorption capacity. In practice, metal precipitation generally does not produce a stabilized form of heavy metal. The precipitation can sometimes be very small in size and, upon the neutralization of the effluent from the wastewater treatment plant, the solubility of the metals increases, resulting in a re-contamination of the waste outlet stream. It is considered that adsorbents had a maximum biosorption capacity at a pH 6, if the precipitated amount is not considered in the calculation. Therefore, it will take 6 as the optimum pH for the biosorption of Cd(II) onto rice husk for the later experiment.

Tangjuank*et al*. (2009) found that the optimum pH was 6 when using cashew nut shells to removal Cd(II) from water

The effect of shaking time on biosorption of Cd(II) is illustrated in **Fig. 4**. This figure

indicates that the metal concentration in aqueous solution decreases rapidly at the beginning and remains nearly constant after 90 min; this is probably due to a larger surface area of the rice husk being available at the beginning.

As the surface biosorption sites become exhausted, the uptake rate is controlled by the rate at which the adsorbate is transported from the exterior to the interior sites of the adsorbent particles. The increasing contact time increased the Cd(II) adsorption and it remained constant after reach equilibrium. The maximum percentage of Cd(II) removal was attained after about 100 min of shaking time. Therefore, 100 min is selected as optimum shaking times.

El-sayed, *et al*. (2010) find that at 90 min the biosorption of Cd(II) by rice straw reach equilibrium.

3.2 FT-IR Analysis of Adsorbents

The FT-IR spectra of rice husk before and after biosorption of Cd(II) was plotted to determine the vibration frequency changes in the functional groups of the adsorbent as in **Fig. 5**and**6.**

These figures show the results obtained in this study. The spectra was measured within the range of 400–4000cm^{-1}. As shown in the Figures, the spectra display a number of adsorption peaks, indicating the complex nature of the material examined. The broad, intense absorption peaks around 3760-3340 cm^{-1} are indicative of the existence of bounded hydroxyl groups (-OH). The peaks observed at 2924 cm^{-1} can be assigned to the C–H group. The peaks around 1650 cm^{-1} are due to the carbonyl C=O stretching vibration of the carboxyl groups, while the intense band at 1380 cm^{-1} are initiated by carboxylate group (-COO) stretching. The peaks ranging from 1300-1000 cm-1 are described generally to the C–O stretching vibration in carboxylic acids and alcohols. The additional peaks at 609.8–832.6 cm^{-1} can be assigned to bending modes of aromatic compounds. All these peaks in the sample after adsorption show an absorbance substantially lower than those in the raw sample and small differences in the frequency bands

The results show that Cd(II) may be adsorbed or complexed by hydroxyl, carboxylic acids and alcohol, carboxylate and carbonyl.Results show that the bands of hydroxyl groups shifted to lower frequency. The total displacements of these functional groups were, 81 for hydroxyl group, 3.85 for carbonyl group, 3.86 for carboxylate group, 11.57 for carboxylic acids and alcohols groups, and 23.14 for aromatic compound due to the biosorption of Cd(II) onto surface of biomass. The bands of functional groups shifted to lower frequency with total amount of 123.42.

Table 2 shows the main function groups before and after biomass loaded with Cd(II) ions.

These results are similar to that obtained in previous studies by Hengpeng (2010), Srivastava*et al*. (2009) and Garg*et al*. (2008).

Fig. 7 shows that the equilibrium isotherm is of a favorable type and by apply the fourth isotherm model its fined in **Fig. 8** that Freundlich model is the best fit model to describe the biosorption of Cd(II) by rice husk and the parameters and correlation coefficient of these models are show in **Table 3.**

These results were analogues to that found from Kumar *et al*., (2010) and El-sayed*et al.* (2010) when used rice husk ash and rice straw respectively as adsorbent and Cd(II) as adsorbat.

4. Conclusion

- Biosorption of Cd(II) increases rapidly with increasing mass of adsorbent from 0.1 to 2.5 g with removal efficiency from 20 to 97 %, while maximum uptake 9mg/g was achieved at lower mass of adsorbent.
- The percentage removal of metal ion decreased with the decrease in pH .The optimum pH value is 6 to remove cadmium by biosorption process from polluted solution
- The metal concentration in aqueous solution decreases rapidly at the beginning of the experiment and remains nearly constant after 90 min. The increasing contact time increased the Cd(II) biosorption and it remained constant after reach equilibrium. The maximum percentage of Cd(II) removal was attained after about 100 min of shaking time.

- Hydroxyl (-OH), Carboxylic (C-O),aromatic compound and carboxylate (-COO-), carbonyl (-C=O) functional groups on the surface of rice husk play the major role in biosorption of Cd(II) ions by complex mechanism.
- Freundlich isotherm is the best fit model to describe the biosorption of Cd(II) onto rice husk with high correlation coefficient 0.983 and 1/n less than 1 .

Nomenclature

b	Langmuir constant , l/mg
B	constant to describe the energy of Interaction between the solute and the adsorbent surface.
C	Concentration in fluid, mg/l
C_o	Initial concentration, mg/l
C_t	Concentration at given time.mg/l
Cs	is the saturation concentration of solute (mg/l)
d_p	Particle diameter (m).
g	Gravitational force (= 9.81 m/s^2)
K_f	Liquid film mass transfer coefficient (m/s).
M	Mass of adsorbent (g).
n	Freundlich constant
q_e	Amount of adsorbate adsorbed per unit mass of adsorbent (mg/g).
q_{max}	Adsorption equilibrium constant defined byLangumer equation (mg/g)
q_t	Amount of pollutant adsorbed at time t (mg/g)
Q	amount of solute adsorbed in forming acomplete mono- layer (mg/g).
R	Universal gas constant(=0.8314) (kJ/mol.K)
R_p	Radius particle, m
t	Time (s).
V	volume of solution (L).
w_o	Mass of adsorbent (kg).

Greek Symbol

μ_l	liquid viscosity (water $=1\times10^{-3}$Pa.s)
ρ_l	Density of liquid (kg/m^3)
ρ_p	Density of solid (kg/m^3)

List of Abbreviations

BET	BrunauerEmmetTeller method
FT-IR	Fourier Transform-Infrared Radiation
rpm	Revolution per minutes
WHO	World Health Organization

Acknowledgment

We would like to express our sincere thanks and deep gratitude to the Ministry of Water Resources, National Center for Water Management, Baghdad, Iraq for supporting this work financially.

Reference

Ajmal, M., Rao, R. A., Anwar, S., Ahmad, J. and Alunad, R., 2003. Adsorption studies on rice husk: Removal and recovery of Cd (II) from wastewater. Bioresource Technology, 86, p147-149.

Bailey, S. E., Olin, T. J., Bricka R. M. and Adrian, D. D., 1999.A review of potentially low-cost sorbents for heavy metals. Water Research, 33, p2469-2479

Brunauer, S., Emet, P.H. And Teller, E., 1938. Adsorption of Gases InMultimoleculer Layers. J. Am. Chem. Soc. 60, 309.

Cheung, C. W., Porter J. F. and McKay, G., 2001. Sorption kinetic analysis for the removal of cadmium ions from effluents using bone char".Water Research, 35, p605-621.

Drush, G. A., 1993, Increase of Cadmium body burden for this century. Science of the Total Environment, 67, p75-89.

El-Sayed, G.O., Dessouki, H.A. and Ibrahim, S.S., 2010.Biosorption Of Ni(II) And Cd(II) Ions From Aqueous Solutions Onto Rice Husk Straw. Chemical Sciences Journal.

Freundlich, H., 1907. Ueber die Adsorption in Loesungen. Z.; Phisik.Chem. v. 57, p385-470.

Hengpeng Ye, Qing Zhu and Dongyun Du, 2010. Adsorptive removal of Cd(II) from aqueous solution using natural and modified rice husk. Bioresource Technology, vol. 101, p5175–5179

Kumar, S.P., Ramakishnan, K., Kirupha, D.S. and Sivanesan, S., 2010. Thermodynamic and kinetic studies of cadmium adsorption from aqueous solution onto rice husk. Brazilian Journal of Chemical Engineering, vol.27 no.2 São Paulo, version issn 0104-6632

Langmuir, I., 1918. The adsorption of gases on plane surfaces of glass, mica and platinum.J. Am. Chem. Soc.; v. 40, p1361-1403.

Mashitah, M.D., YusAzila, Y., Bhatia, S., 2008.Biosorption of cadmium (II) ions by immobilized cells of Pycnoporussanguineus from aqueous solution. Bioresour.Technol, 99, p4742–4748.

Sulaymon, A.H., Ebrahim, S.E., Abdullah, S.M. and Al-Musawi, T.J., 2010.Removal of lead, cadmium, and mercury ions using biosorption. Desalination and Water Treatment, vol.24 , p 344–352

Sun, G. and Shi, W., 1998. Sun flowers stalk as adsorbents for the removal of metal ions from wastewater. Industrial and Engineering Chemistry Research, 37, p1324-1328.

Temkin, M., 1934. Die gas adsorption under nernstschewärmesatz. Acta.Physicochem. URSS, Vol. 1, p. 36–52.

WHO, 2004.Guidelines for drinking-water quality. 3rd Edition, Volume1, Recommendations, World Health Organization, Geneva

Table 1 show the characteristic of rice husk

physical property	**%**
Particle size range (mm)	0.6 - 1
Equivalent diameter (mm)	0.775
Bulk density (g/ml)	0.2197
Solid density (g/ml)base dry	1.48
Surface area (m^2/g)	0.3018
Bed Porosity	0.911
Husk porosity	0.5
chemical composition	**%**
Volatile matter	64.7
Fixed carbon	15.7
Ash	19.6

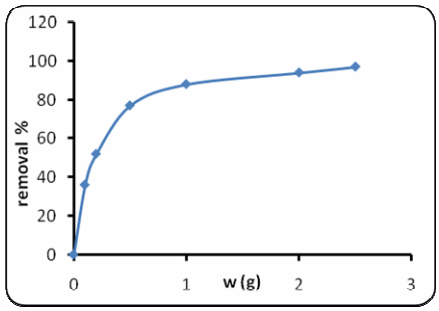

Fig. 1 Effect of different mass of adsorbent on Cd(II) removal efficiency, C_O=25mg/l, pH=6 , 150 rpm and t=3hr

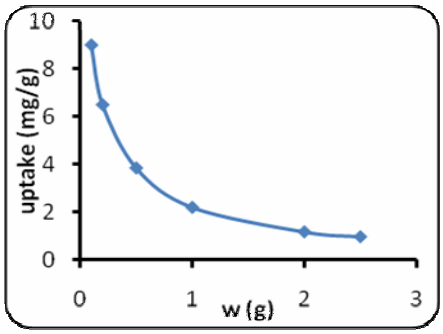

Fig. 2 Effect of different mass of adsorbent on Cd(II) up take, C_O=25mg/l, pH=6 150 rpm and t=3hr

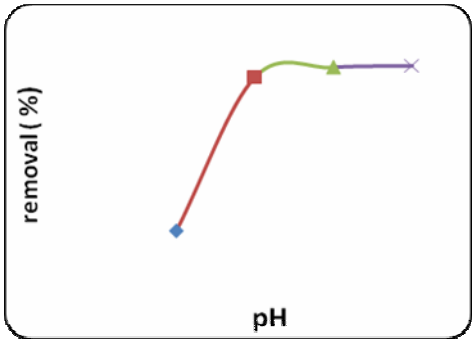

Fig. 3 Effect of different pH values on Cd(II) removal efficiency C_O=25mg/l , 2.5g of adsorbent, t=3hr and 150 rpm

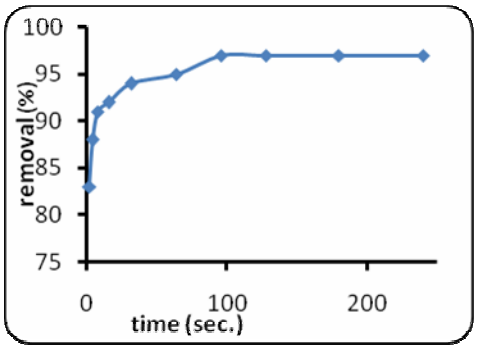

Fig. 4 Effect of different contact time on Cd(II) removal efficiency C_O=25mg/l, 2.5g of adsorbent, pH=6 and 150 rpm

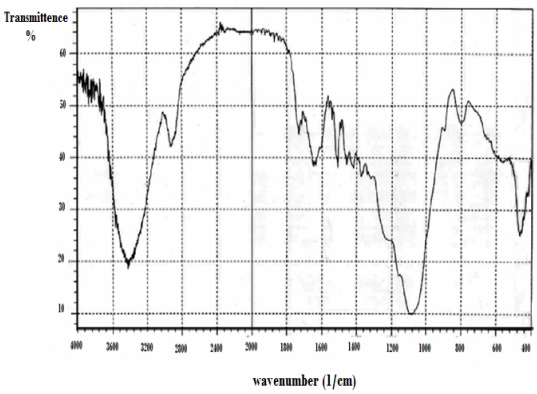

Fig. 5 FTIR spectra for rice husk biomass before loaded with 25 mg/l of Cd(II)

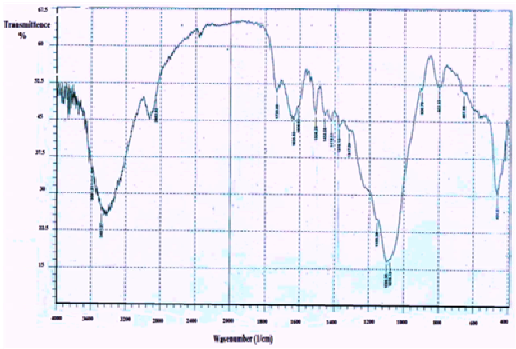

Fig. 6 FTIR spectra for rice husk biomass after loaded with 25 mg/l of Cd(II)

Table 2 Function groups before and after rice husk loaded with Cd(II)

FT-IR peak	Assignment groups	unloaded (cm^{-1})	loaded (cm^{-1})	Difference (cm^{-1})
1	Hydroxyl (OH)	3566.14	3591.21	25.07
2	Hydroxyl (OH)	3425.34	3481.27	55.93
3	Carbonyl (C=O)	1637.45	1635.52	1.93
4	Carbonyl (C=O)	1456.16	1458.08	1.92
5	Carboxylate (COO^-)	1373.22	1375.15	1.93
6	Carboxylate (COO^-)	1319.22	1317.29	1.93
7	Carboxylic acids and alcohols (C-O)	1157.21	1155.28	1.93
8	Carboxylic acids and alcohols (C-O)	1093.56	1099.35	5.79
9	Carboxylic acids and alcohols(C-O)	1074.28	1078.13	3.85
10	Aromatic compound	898.77	900.7	1.93
11	Aromatic compound	794.62	802.33	7.71
12	Aromatic compound	667.32	657.68	9.64
13	Aromatic compound	468.67	464.81	3.86
Total sum.		123.42		

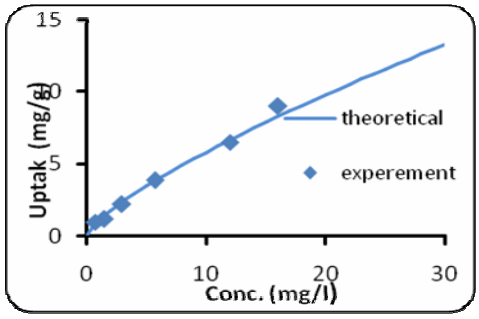

Fig. 7 The adsorption isotherm of Cd(II) onto rice husk biomas

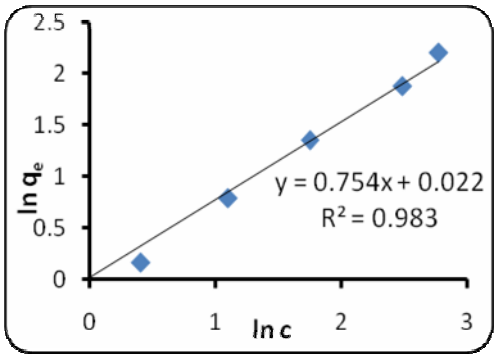

Fig. 8 Freundlich model (C=Conc. in mg/l and q_e= uptake in mg/g)

Table 3 Parameters isotherm for adsorption of Cd(II) ions onto rice husk

Model	Parameters	value	Refrence
Langmuir $q_e = \frac{q_{max} \times b \times C}{1 + b \times C}$	q_{max}(mg/l)	7.692	Langmuir (1918)
	b(l/mg)	0.1836	
	R^2	0.904	
Freundlich $q_e = K_f C^{1/n}$	K_f (l/g)	1.022	Freundlich (1907)
	n	1.326	
	R^2	0.983	
Temkin $q_e = \frac{RT}{b} \ln(K_T C)$	K_T(mg/g)	1.209	Temkin (1934)
	B=RT/b (l/mg)	2.53	
	R^2	0.880	
BET $q_e = \frac{BQC}{(C_s - C)[1 + (B-1)(C/C_s)]}$	B	9.9643	BET (1938)
	Q(mg/g)	3.5842	
	R^2	0.982	

Modeling of Corrosion Rate Under Two Phase Flow in Horizontal Pipe Using Neural Network

Fadhil Sarhan Kadhim

University of Technology
Petroleum Technology Department

Yousif Khalaf Yousif

Ministry of Higher Education and Scientific Research
Research and Development Department

Abstract

The present study develops an artificial neural network (ANN) to model an analysis and a simulation of the correlation between the average corrosion rate carbon steel and the effective parameter Reynolds number (Re), water concentration (Wc) % temperature (T ^{o}) with constant of PH 7 . The water, produced fom oil in Kirkuk oil field in Iraq from well no. k184-Depth2200ft., has been used as a corrosive media and specimen area (400 mm^2) for the materials that were used as low carbon steel pipe. The pipes are supplied by Doura Refinery . The used flow system is all made of Q.V.F glass, and the circulation of the two –phase (liquid – liquid) is affected using a Q.V.F pump .The input parameters of the model consists of Reynolds number , water concentration and temperature. The output is average corrosion rate .The performance of the two training algorithms, gradient descent with momentum and Levenberg-Marquardt, are compared to select the most suitable training algorithm for corrosion rate model. The model can be used to calculate the average corrosion rate properties of carbon steel alloy as functions of Reynolds number, water concentration and temperature. Accordingly, the combined influence of these effective parameters and the average corrosion rate is simulated. The results show that the corrosion rate increases with the increase of temperature, Reynolds number and the increase of water concentration.

Keywords: Corrosion rate, Two phase flow, ANN, Modeling

الخلاصة

في الدراسة المقدمة، قد تم تطوير نموذج شبكة عصبية اصطناعية(ANN) لتحليل ومحاكاة للعلاقة ما بين متوسط معدل تآكل الكربون الصلب والعوامل المؤثرة وهي (عدد رينولد وتركيز المياه ودرجة الحرارة) بثبات PH . الماء المستخدم بالدراسة هو الماء المنتج مع النفط في حقل النفط في كركوك في العراق برقم .k184-Depth2200ft و قد تم استخدام وسط للتآكل ومنطقة العينة (400 mm^2) على المواد التي تستخدم الانابيب الفولاذية ذات الواطئ والتي توفرها مصفاة الدورة وقد تم استخدام نظام التدفق بواسطة Q.V.F الزجاجي وتدوير ثنائي الطور (سائل – سائل) باستخدام مضخة Q.V.F ، عوامل الادخال للنموذج المقترح كانت رقم رينولدز و تركيز الماء ودرجة الحرارة والناتج الخارج من النموذج هو معدل التأكل . الاداء لطريقتي تدريب الشبكة الاصطناعية وهما (هبوط الانحدار مع الزخم و ليفن بيرك ماركورت) قورن لاختيار طريقة التدريب الاكثر ملائمة للنموذج معدل التأكل ويمكن استخدام هذا النموذج لحساب خواص معدل التأكل لسبيكة الفولاذ كاربون كمعادلة مع معامل رينولد وتركيز المياه ودرجة الحرارة . التأثير المتراكب لهذه العوامل المؤثرة مع معدل التأكل تم تمثيله حيث بينت النتائج ان معدل التأكل يزيد بزيادة هذه العوامل المذكورة انفا .

Introduction

The applications of two phase flow are found in petroleum exploration ,transport chemical engineering, nuclear reactors and thermal systems [Wenyin Zhang 2010]. In oil field water is often produced in large quantities with crude and the characteristics of two phase flow are of interest both in well itself where the flow is vertical in the production tubing and in horizontal pipe lines transporting crude oil to filed treating facilities [F. Sarhan 1996]. Many studies have investigated two-phase capillary flow in the last 50 years. Some of them have used mathematical approaches based on numerical simulations to generate a theoretical model of capillary flow. Most of these models have considered two thermodynamic equilibrium regions of sub-cooled liquid and a two-phase vapor–liquid mixture [P.K. Bansal 1998 - S.M. Sami1998 - P. Kritsadathikarn 2002 - M. Fatouh 2007]

The corrosion can be defined as the distractive attach of metal by a chemical or electrochemical reaction with its environment [Uhlig H.H 1977]. Generally the produced water with crude oil leads to corrosion problem because these contents are impurities or dissolved substances such as salt, acid, hydrogen sulfide, carbon dioxide and oxygen which increase the corrosivity of the produced water.

The experimental work

The present study uses low carbon steel pipe which is supplied by Daura Refinery. The pipe is about 2m in length , and 2.54 cm in diameter. It consists of the following chemical composition :

C=0.084% ,Si= 0.225% , Mn=0.787% , P=0.022%,S=0.015% , Cr=0.163%, Mo=0.043% ,Ni=0.13% , Cu=0.232%, V=0.004% , Fe= remains.

The cylindrical specimens, which have a length of 0.5 cm and diameter of 2.54cm and are cut from a carbon steel pipe, are annealed in vacuum at 600C° for an hour (to remove the effect of cold working). Then the furnace is cooled under vacuum to room temperature. Specimens are abraded in sequence under running tap water by using 240,320,420 and 600 emery paper grades. After that, the specimens are washed with running tap water and instantly followed by distilled water. Then they are dried with clean tissue paper ,immersed in ethanol ,dried with clean tissue paper ,immersed in acetone and dried with clean tissue paper respectively. Finally, they are left to dry for an hour over silica gel before use. The water ,which is produced along with oil in Kirkuk oil field from well No. K184, depth of 2200ft , has the following composition:

$CaHCO_3$ =5670ppm, $CaSO_4$ =3451ppm,$CaCl_2$ = 513ppm , $MgCl_2$ =3789ppm,NaCl=13538ppm.

It is worth mentioning that this water was used as corrosive media.

The flow system that has been used, as shown in (figure 1), is made of Q.V.F glass . The circulation of the two-phase liquid (Gas oil-water) was affected using Q.V.F pump and the total flow rate is measured by two calibrated rotary meter with range (0-1400L/hr.).

Different total flow rates, different Reynolds number; (5000, 75000 ,10000, 125000),different phase concentrations (15%, 25%, 35% and 45%) and different temperatures (30 C° and 50 C°) have been tested to calculate the corrosion rate by using weight loss method . Three specimens have been used in each run . The average corrosion rate (A.C.R) was equal to the arithmetical average of three specimens ,The equation of calculation of corrosion rate is as follows:

$$C.R = \frac{\Delta W}{A*T} \quad (1)$$

where :

A=area of specimens exposed to the environment A=πdl

d=inside diameter of specimen , l=length of specimen .

Δw=weight loss .

The experimental data set were calculated as shown in table(1) and plotted in figure (2). They refer to inputs parameter (Reynolds number, temperature and water concentration) to propose a model and an output (corrosion rate). As shown in table (1), the

highest corrosion rate was found at the temperature (50 o) ,Reynolds number (12500) and a (45%) water concentration, because the increase of temperature leads to the increase of the reaction rate between corrosive media and metal surface. Accordingly, the increase of the flow rate leads to the removal of oxidation results at metal surface . Hence, the corrosive media becomes closely related to metal surface. Finally, it is believed that the increase of water concentration increases the corrosion rate, because the corrosive media covers a large area of metal surface.

Proposed Model and Artificial Neural Network (ANN)

Artificial intelligence (AI) predictions have been widely used in the domain of model systems which are rarely modeled by the use of traditional methods. They have been referred to as having the ability to be trained like humans, by accumulating knowledge throw recurring learning activities[8].

A feed-forward neural network with nine inputs neuron, one with a hidden layer and one with an output neuron, were used. The architecture of the model is depicted in fig (3). The activation function in the hidden layer is Log-Sigmoid transfer function which normalizes the data and, hence, the transformed data which lie between -1 and 1 . In the output layer the linear transfer function is used.

Training a network involves presenting it with examples, and representing the relationship between inputs of process (Reynolds number, temperature and water concentration) and output (average corrosion rate) as well. These examples are called "training data set patterns". Table (1) shows the training data set. There is a large number of training algorithms for feed forward neural network, as discussed in a previous section.

It is very hard to decide which Algorithm performs better for a specific application. Thus the neural network model has been trained using two different training algorithms:

1- Gradient Descent with Momentum Algorithm.

2- Levenberg - Marquardt Algorithm.

The performances of these two training algorithms are compared to decide which algorithm performs better than the other. The neural network may converge to a local minimum rather than a global one. Therefore, some sort of simulated annealing technique is used to find the best solution among many local minima [9]. The annealing technique is clarified as follows: once the network converges to a local minimum, the network state is perturbed in a random direction and by a random magnitude. Then the network dynamics are reactivated. Herby, another local minimum is found. During this process, the algorithm keeps track of the best solution. After finding a predetermined number of local minima, the algorithm terminates and the solution with the lowest error is accepted as the best solution.

After examining the performance of different architectures, a network with one hidden layer (include 9 neurons) trained by Levenberg-Marquardt algorithm has showed good performance indication. Figure (5) shows the training session as the training error decrease versus number of iterations (epochs) until goal error meeting

Where:

W1: weights among Ren and hidden layer.

W2: weights among Temp. and hidden layer.

W3: weights among WC % and hidden layer.

W3: weights among hidden layer and Output layer (corrosion rate).

b1: bias to hidden layer b2:bias to output layer.

Post Training Analysis

The data set obtained from experiments are divided randomly into three subsets, namely training and testing sets in 50% to 10% of the total data, respectively. The training set is used to calculate the gradient and to form the weight factors and bias. The remaining 10% testing data set is used to calculate the prediction error to estimate the accuracy of the models on the unseen data set, but it is often useful to investigate the network response in more details. One option is to perform a regression analysis between the network response (predicted outputs) and the corresponding targets. Figure(6) illustrate a straight line representing the

best linear regression relating targets (actual of average corrosion rate) to network response.
When perfect fit had been found (predicted outputs exactly the same the actual values), the slope of this straight R line would be one .From figure (7) and figure (8) it can be shown that these values are very close, which indicate a good response to training sets.

Neural Network Simulation

Testing of neural network model requirs new independent (test sets) to validate the generalization capability of network. Table (4.8) shows testing data sets for the network and the response of the network to these data sets.
The prediction accuracy for the testing patterns based on mean absolute percent error (APE) criteria in eq. (2) :

$$APE = \{ |\text{Predicted} - \text{Actual}| / \text{Actual} \} * 100\% \quad (2)$$

Conclusions

The main conclusions obtained from the present research are :

1. Corrosion rate increases with increasing Reynolds number, water concentration and temperature.
2. The multilayer feed-forward neural network is successfully mapping the relationship among inputs parameters corrosion rate under two phase flow in horizontal pipe.
3. For the proposed NN model the Levenberg – Marquardt algorithm shows better performance than gradient descent with momentum because it uses 2nd order Taylor series approximation of performance index rather than 1St order approximation as with gradient descent algorithm.

References

F. Sarhan, “investigation of carbon steel corrosion under two-phase (Kerosene-Brine) and multi-phase flow (Kerosene-Brine-CO2) in horizontal pipe”, Baghdad University,1996

M. Fatouh, Theoretical investigation of adiabatic capillary tubes working with propane/n butane/iso-butane blends, Energy Conversion and Management 48 (2007) 1338–1348.

Mohan Kumar et al ,” Neuro-fuzzy and neural network-based prediction of various responses in electrical discharge machining of AISI D2 steel”, Springer Int J Adv Manuf Technol (2010)

P. Kritsadathikarn, T. Songnetichaovalit, N. Lokathada, Pressure distribution of refrigerant flow in an adiabatic capillary tube, Research Article, Science Asia 28 (2002) 71–76.

P.K. Bansal, A.S. Rupasinghe, An homogeneous model for adiabatic capillary tubes, Applied Thermal Engineering 18 (1998) 207–219.

S.M. Sami, C. Tribes, Numerical prediction of capillary tube behaviour with pure and binary alternative refrigerants, Applied Thermal Engineering 18 (1998) 491–502.

Tania Binos "Evolving Neural Network Architecture and Weights Using An Evolutionary Algorithm" Msc Thesis, Department Of Computer Science RMIT, April 10, 2003.

Uhlig H.H., “Corrosion and corrosion control”, John Wiley and sons Inc., 2nd Edition 1977.
Wenyin Zhang et al, “Recognition of gas-liquid two-phase flow patterns based on improved local binary pattern operator”, international Journal of Multiphase Flow, 36 ,2010.

Table (1) Experimental Data Sets

Set No	water concentration %	Temp C	Re	ACR mmd	Set No	water concentration %	Temp C	Re	ACR mmd
1	15	30	5000	200.7	17	35	30	5000	279.4
2	15	30	7500	250.68	18	35	30	7500	385.2
3	15	30	10000	400.37	19	35	30	10000	540.7
4	15	30	12500	449.22	20	35	30	12500	630.2
5	15	50	5000	260.17	21	35	50	5000	330.15
6	15	50	7500	279.64	22	35	50	7500	416.51
7	15	50	10000	47206	23	35	50	10000	630.85
8	15	50	12500	485.5	24	35	50	12500	649.71
9	25	30	5000	270.53	25	45	30	5000	309.27
10	25	30	7500	306.8	26	45	30	7500	416.79
11	25	30	10000	504.3	27	45	30	10000	618.68
12	25	30	12500	512.6	28	45	30	12500	628.26
13	25	50	5000	301.19	29	45	50	5000	339.16
14	25	50	7500	340.9	30	45	50	7500	360.7
15	25	50	10000	539.1	31	45	50	10000	674.7
16	25	50	12500	619.43	32	45	50	12500	696.8

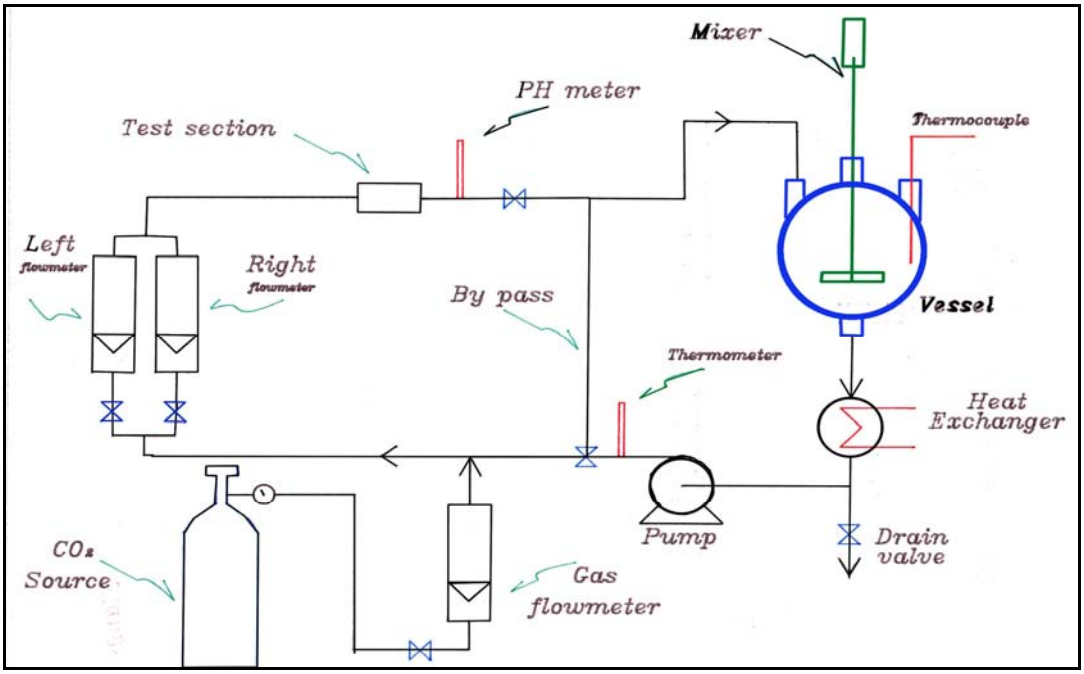

Fig. (1) Schematic flow diagram of experimental apparatus

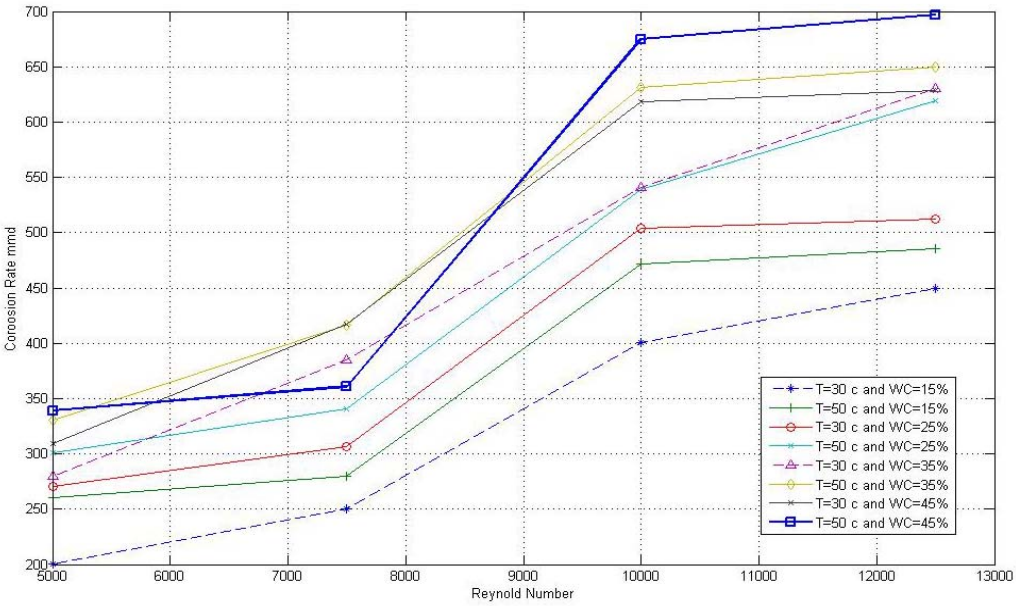

Fig.(2) Corrosion rate Vs Reynolds number

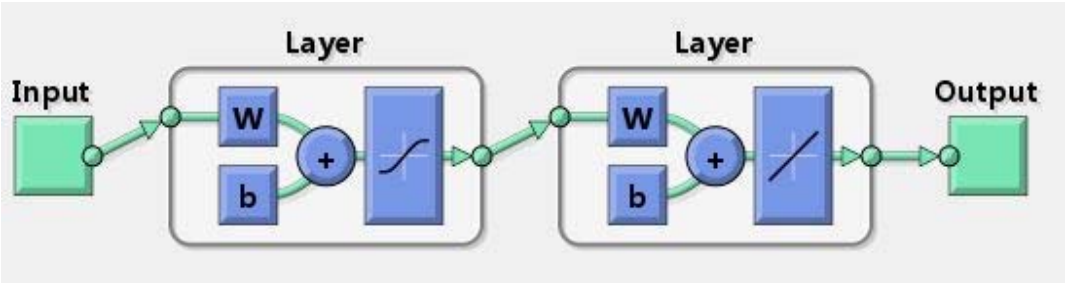

Fig. (3) Artificial Neural Network

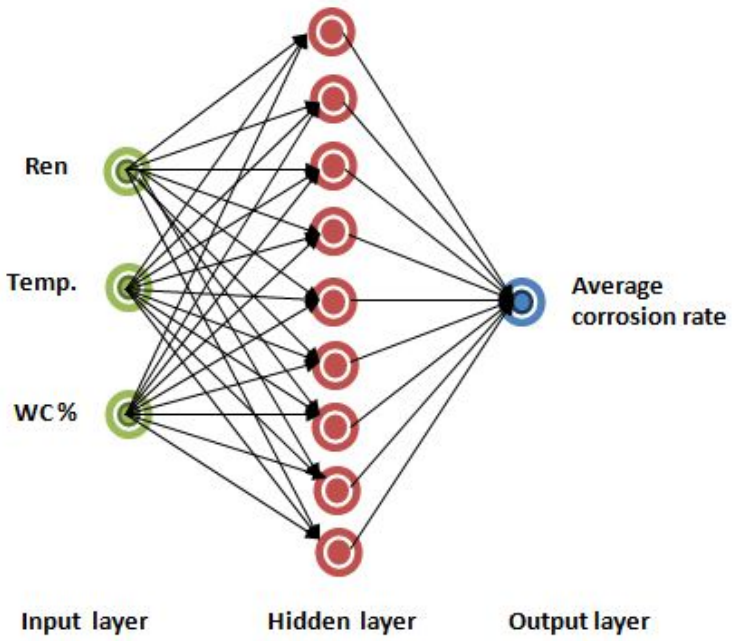

Fig. (4) Neural network architecture

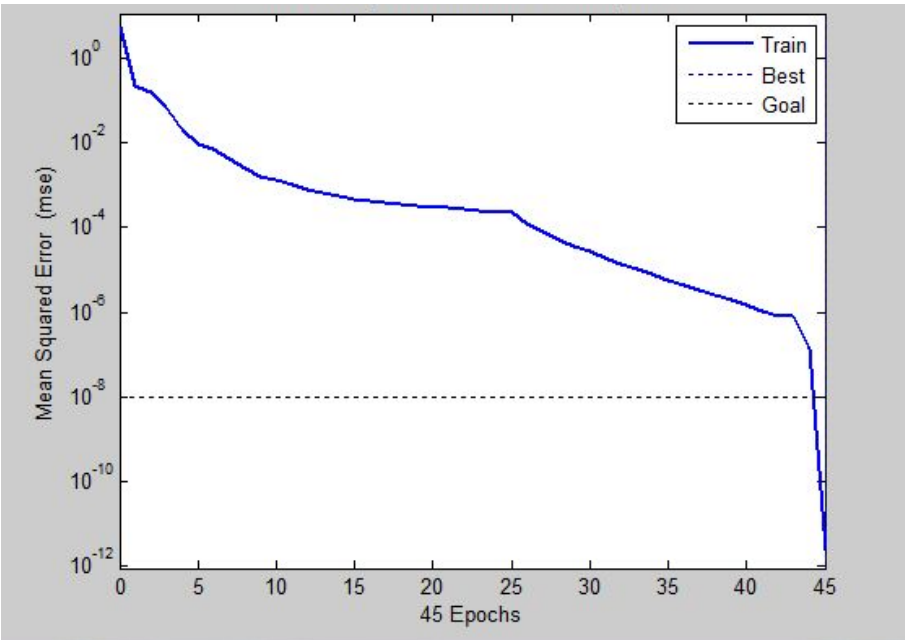

Fig. (5) Training Session

Table (2) The weights and bias between inputs and hidden layer

W1	W2	W3	W4	b1	b2
0.718647	-5.85696	-8.88151	-0.61732	-7.47805	0.049794566
-3.44112	4.323622	2.556928	-1.12072	5.986354	
9.025448	2.243282	1.143872	-0.40574	-2.92597	
11.76387	2.028157	2.87373	2.027852	2.785801	
2.645666	-1.11169	-8.79878	-0.68903	-0.71903	
1.830581	6.81657	-1.17294	-0.69285	-0.14563	
-8.0053	4.26784	3.474221	-1.54134	-3.74571	
-4.17033	8.68734	-3.04253	1.296458	-1.39753	
-11.7345	-0.28785	-1.477	1.566467	-3.95063	

Where:
W1: weights among Ren and hidden layer.
W2: weights among Temp. and hidden layer.
W3: weights among WC % and hidden layer.
W3: weights among hidden layer and Output layer (corrosion rate).
b1: bias to hidden layer b2:bias to output layer.

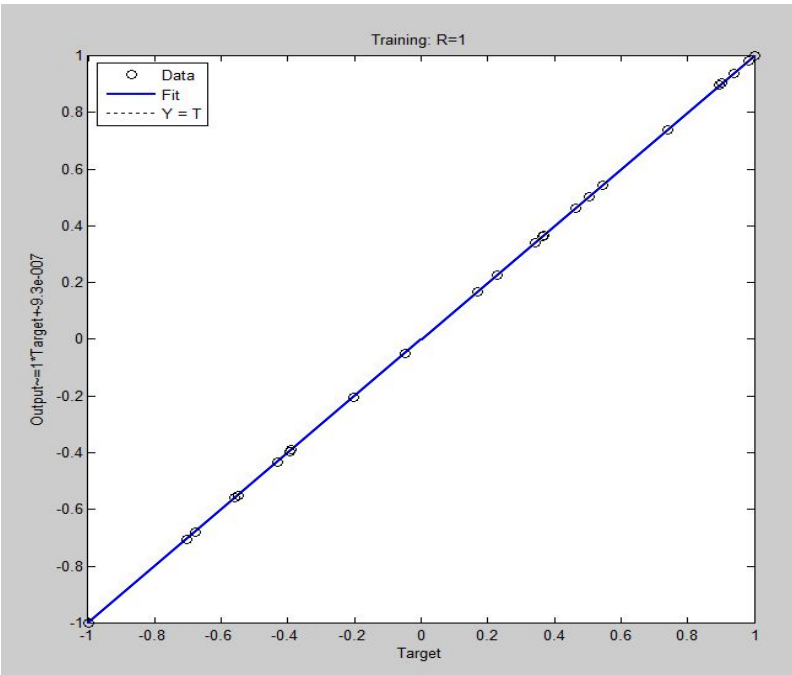

Fig. (6) Best linear fit of average corrosion rate in training set

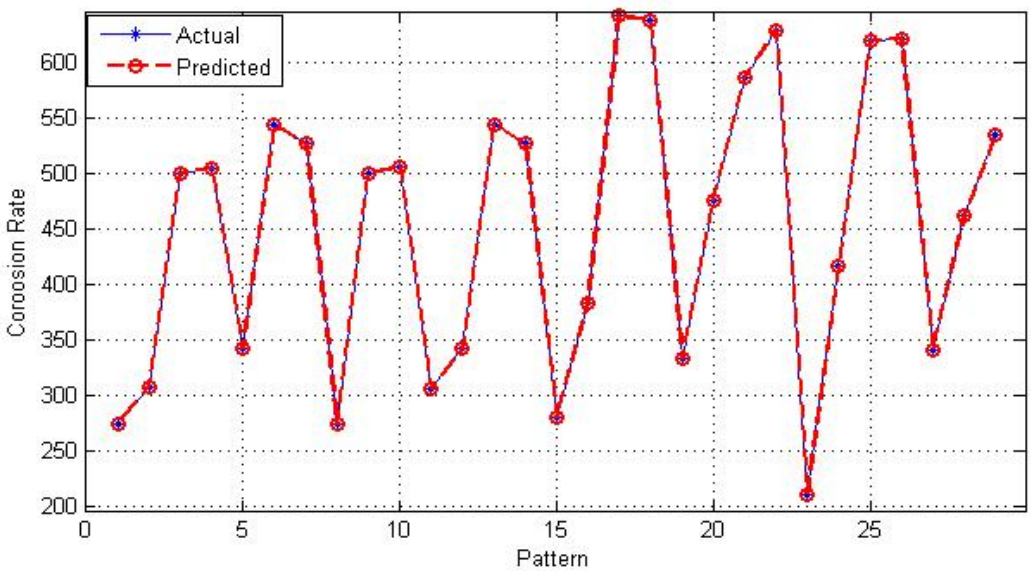

Fig.(7)Predicted and actual corrosion rate for training

Table (3) Test data sets and network response

Set No	ACR mmd	NN Response	APE %
5	306.91	287.9431	6.1799
10	303.99	320.7760	5.5219
31	584.8	578.7600	1.0328

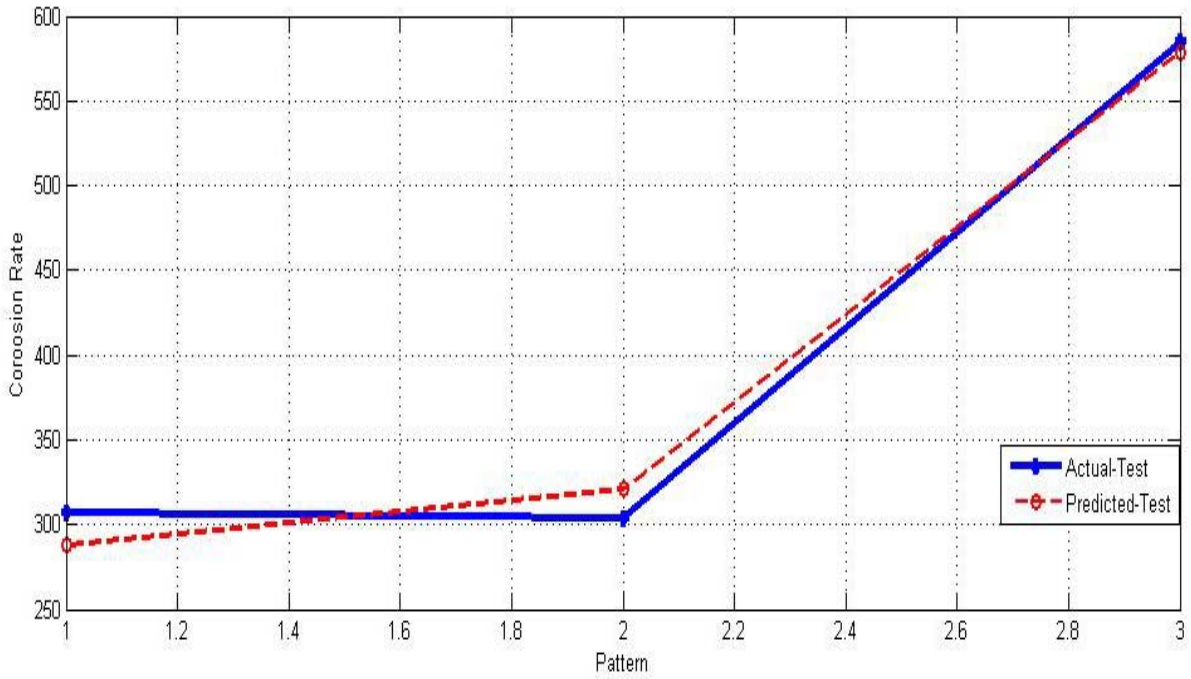

Fig. (8) predicted and actual corrosion rate for testing data sets (unseen in the training)

ENGINEERING

College of Engineering Baghdad University Baghdad

List of Contents

English Section: Page

Modeling of Corrosion Rate Under Two Phase Flow in horizontal Pipe Using Neural Network **876 - 885**

Fadhil Sarhan Kadhim
Yousif Khalaf Yousif